Crustal seismic imaging across the San Andreas fault system using narrow-angle reflection industry data

---

Seismische Abbildung der Krustenstruktur des San Andreas Störungssystems unter Verwendung von industriell erhobenen reflexionsseismischen Steilwinkeldaten

DISSERTATION

zu Erlangung des Doktorgrades
am Fachbereich Geowissenschaften
der Freien Universität Berlin
Fachrichtung Geophysik

von
Stine Gutjahr

Berlin, 2015

Tag der mündlichen Prüfung: 29. Mai 2015

1. Gutachter: Prof. Dr. Serge Shapiro
2. Gutachter: Prof. Dr. Stefan Buske

"Ich versichere, dass ich die Dissertation selbstständig verfasst habe. Andere als die angegebenen Hilfsmittel und Quellen wurden nicht benutzt. Die Arbeit hat keiner anderen Prüfungsbehörde vorgelegen. "

„How do you find America?“
„Turn left at Greenland.“
— Ringo Starr
(Media question to the Beatles during first U.S. tour 1964)

Meinem Vater in treuem Gedenken!
Horst Gutjahr (* 8. Juli 1951, † 25. Dezember 2010)

Summary

The San Andreas transform fault system is one of the most extensively studied plate boundaries in the world. Since the great 1906 San Francisco earthquake at the latest, geoscientists investigate the huge transform plate boundary in order to derive detailed models of the complex fault system. The aim is to understand the processes that control the transform motion of the adjacent lithospheric plates and to estimate its future potential to trigger large and destructive earthquakes.

Seismic migration methods provide valuable information on the subsurface structure by investigating the ability of the subsurface materials to reflect seismic signals that have been generated by controlled seismic sources. The resulting depth images can then further be interpreted in terms of the subsurface geological structures.

The present thesis uses advanced imaging techniques to determine new structural seismic depth images from the old industry reflection seismic data set SJ-6 across the San Andreas fault system in south central California.

The complete data set from 1981 was purchased from the United States Geological Survey (USGS). The profile line crosses the California Coast Ranges nearly perpendicular to the prominent San Andreas fault zone and the Great Valley from west to east.

Three different migration techniques, Kirchhoff Prestack Depth migration, Fresnel Volume migration and Reflection Image Spectroscopy, respectively, are used to determine the reflectivity structure of the whole crust beneath the SJ-6 profile line. The imaging results are compared and evaluated with respect to the image quality and the observable subsurface structures. Kirchhoff Prestack Depth migration is a standard imaging technique that is suitable to image complex geological structures. Compared to the other applied methods it is less time consuming but produces considerable migration artefacts especially in cases of low data coverage. The advanced Fresnel Volume migration uses the principle of Fresnel Volumes to restrict the migration operator to the region around the actual reflection point. In this way, migration artefacts are significantly reduced and far more distinct structures can be observed in the seismic images. Reflection Image Spectroscopy is used to consider the relation between the signals wavelength and the size of

the heterogeneities in the subsurface by individually migrating discrete frequency bands. Additional small- as well as large-scale subsurface structures are imaged.

The applied migration techniques are implemented in 3D in order to account for the irregular course of line SJ-6 and its significant kink that results in a change of direction from predominantly northeast to east. For that reason, the processing steps are adjusted in order to obtain seismic depth images of the whole crust from directly beneath the SJ-6 receiver line. The most significant structures that can be identified in each of the seismic depth images are summarized by creating respective reflector maps of the subsurface. Each of the three migration techniques is performed by using the same local 3D background velocity model derived from earthquake tomography.

The imaged structures are finally interpreted by comparing the imaging results with other recent geophysical studies. It is shown that the individual terranes across the San Andreas fault system significantly differ in their reflectivity structure. Sequentially layered strong reflectors are identified in the lower crust of the Salinian Block southwest towards the San Andreas fault. They are approximately 5 km in width and terminate abruptly adjacent to the San Andreas fault zone. The San Andreas fault zone itself appears as a near vertical zone that is 4 km in width and lacks of distinct reflectors. The imaged fault zone is further characterized by low seismic velocities and a narrow subvertical band of high seismic activity in the upper and middle crust. It successively broadens with increasing depth below the brittle-ductile transition zone. Non-volcanic tremor locations are mainly located in the lower crust southwest to the San Andreas fault surface trace but inside the non-reflective zone. For that reason, these specific seismic signals are attributed to the deep extensions of the San Andreas fault zone that can be traced through the entire crust according to its distinctive reflectivity structure.

The San Joaquin Valley east to the San Andreas fault zone is characterized by westward dipping sedimentary layer sequences in the shallow crust. They overlay a body of steeper west dipping structures that are attributed to Great Valley ophiolites according to its correlation with unusual high velocities. These particular structures have so far been imaged for the first time in this particular region. The depth of the crust-mantle boundary gradually increases towards east with increasing distance to the San Andreas fault zone.

This work demonstrates that old seismic data sets contain a multitude of subsurface information that traditional processing techniques are not able to extract. Additional subsurface information also on new target depths can be obtained by reprocessing old data sets using advanced processing techniques. Previous interpretations can be complemented and reevaluated in consideration of recent investigation results.

Zusammenfassung

Das San Andreas Störungssystem ist seit vielen Jahrzehnten Objekt umfangreicher geowissenschaftlicher Studien. Spätestens seit dem verheerenden Erdbeben von San Francisco im Jahr 1906 wird das komplexe Störungssystem genau untersucht, um detaillierte Modelle abzuleiten, mit deren Hilfe das Erdbebenrisiko entlang der Verwerfungszonen abgeschätzt und die Prozesse der Plattenverschiebung beschrieben werden können.
Seismische Migrationsmethoden bieten dazu die Möglichkeit mittels aktiver seismischer Experimente das Reflexionsvermögen des Untergrundes als seismisches Abbild darzustellen. Dieses kann anschließend hinsichtlich der geologischen Strukturen interpretiert werden.
In der vorliegenden Arbeit wird der 1981 industriell erhobene reflexionsseismische Datensatz SJ-6 erneut bearbeitet, um mittels moderner Migrationsmethoden neuartige seismische Abbilder entlang des San Andreas Störungssystems im südlichen Zentralkalifornien zu erzeugen.
Dazu wurde der komplette Datensatz vom Geologischen Dienst der Vereinigten Staaten (USGS) erworben, dessen Profillinie das kalifornische Küstengebirge nahezu senkrecht zur San Andreas Verwerfung und das kalifornische Längstal (San Joaquin Valley) in Richtung von West nach Ost überquert.
Das Reflexionsvermögen der gesamten Kruste unterhalb der Profilline wird durch drei verschiedene Migrationsmethoden bestimmt, um die Ergebnisse zu vergleichen und die Methoden hinsichtlich der Qualität der Abbilder beurteilen zu können. Angewendet werden die Kirchhoff Prestack Tiefenmigration, die Fresnel Volumen Migration und die Reflection Image Spectroscopy Methode. Die Kirchhoff Prestack Tiefenmigration wird heutzutage standardmäßig eingesetzt und eignet sich sehr gut zur Abbildung komplexer Untergrundstrukturen. Obwohl sie schnell in der Durchführung ist, verursacht sie erhebliche Migrationsartefakte, die durch eine geringe Datenabdeckung, besonders am Rand der seismischen Sektionen, aber auch verursacht durch die geringen Quell-Empfängerabstände, entstehen. Die neuartige Fresnel Volumen Migration greift das aus der Optik und Funkübertragung bekannte Prinzip der Fresnel Zonen auf, um den Migrationsoperator im Untergrund auf die Region nahe des eigentlichen Reflexionspunktes zu beschränken und dadurch

die Bildung von Migrationartefakten zu vermindern. Die daraus resultierenden Abbilder enthalten zusätzliche Untergrundstrukturen, die sich deutlicher vom Hintergrundrauschen abgrenzen. Da das Reflexionsvermögen im Untergrund auch von der Größe der Untergrundstrukturen und den Wellenlängen der verwendeten seismischen Signale abhängt, wird zusätzlich die Reflection Image Spectroscopy Methode auf die Daten angewendet. Auf diese Weise können zusätzliche Strukturen sowohl im groß- als auch im kleinskaligen Bereich unter Berücksichtigung diskreter Frequenzbereiche abgebildet werden.
Die verwendeten Migrationsmethoden werden aufgrund des unregelmäßigen Verlaufs und des markanten Richtungswechsels der SJ-6 Profillinie in 3D implementiert. Die Bearbeitungsschritte werden entsprechend angepasst, um jeweils ein verlässliches seismisches Abbild der kompletten Erdkruste unterhalb der Profillinie zu erzeugen. Anschließend werden die Abbildungsergebnisse miteinander verglichen und eine Karte der abgebildeten Strukturen erstellt.
Jede der drei Migrationsmethoden wird unter Verwendung des gleichen 3D Geschwindigkeitsmodells durchgeführt, das durch Erdbebentomographie erzeugt und für diese Arbeit zur Verfügung gestellt wurde.
Die in dieser Arbeit abgebildeten Strukturen werden mit den jüngsten Ergebnissen anderer geophysikalischer Studien verglichen und interpretiert. Die abgebildeten Strukturen zeigen, dass sich die einzelnen Gesteinskomplexe des San Andreas Störungssystems deutlich in ihrer Struktur unterscheiden. Südwestlich der San Andreas Verwerfung im Salinischen Gesteinskomplex wird in der unteren Erdkruste eine ungefähr 5 km dicke Sequenz subparalleler starker Reflektoren abgebildet, die südwestlich der San Andreas Verwerfung abrupt enden. Die San Andreas Verwerfung wird als 4 km breite reflexionsarme subvertikale Zone abgebildet, die durch hohe Seismizität und niedrige seismische Geschwindigkeiten im oberen und mittleren Teil der Erdkruste gekennzeichnet ist. Unterhalb des spröd-duktil Übergangs verbreitert sich die reflexionsarme Zone mit zunehmender Tiefe. Im südwestlichen Teil dieser Zone wurden nicht-vulkanische Tremore in der unteren Kruste lokalisiert, die somit der tiefen San Andreas Verwerfung zugeordnet werden können, die durch ihr charakteristisches Reflexionsvermögen in der gesamten Erdkruste identifizierbar ist.
Mit zunehmender Entfernung von der San Andreas Verwerfung in östlicher Richtung nimmt die Tiefe der Erdkruste sukzessive und damit auch die Tiefe des spröd-duktil-Überganges zu. Das San Joaquin Valley ist durch westwärts einfallende subparallele Sedimentschichten in der oberen Kruste charakterisiert, die unterhalb der östlichen Grenze des Küstengebirges gefaltet sind. Die Sedimentschichten des San Joaquin Valleys überlagern einen Block mit starken steil nach Westen geneigten Reflektoren. Diese Strukturen wer-

den aufgrund ihrer Geschwindigkeitsstruktur den sogenannten Great Valley Ophioliten zugeordnet, die in dieser Region erstmals strukturell abgebildet werden konnten.
Es wird gezeigt, dass alte seismische Datensätze meist eine Vielzahl von Informationen enthalten, die mit den üblichen Prozessierungsmethoden nicht erfasst werden können. Die erneute Bearbeitung dieser Datensätze mit modernen Prozessierung- und Abbildungsmethoden bietet die Möglichkeit zusätzliche strukturelle Informationen zu erhalten und vorhandene Interpretationen, wenn nötig, zu aktualisieren und vor dem Hintergrund aktueller Forschungsergebnisse neu zu bewerten.

Contents

List of Figures

1 Introduction and Motivation

Controlled-source seismic experiments have been executed world wide since more than 60 years. They provide substantial information on subsurface structures and the tectonics of the earth's crust by resolving the shape and location of large- as well as small-scale crustal structures. The quality of the resulting seismic depth images thereby depend on the quality of the recorded data but also on the available computing facilities and processing procedures. With the time, the acquisition layouts, recording instruments and the data processing routines have been further developed in order to enhance the earth's seismic response signals and to suppress noise at the same time aiming to achieve seismic depth images of enhanced quality and high resolution.

The essential processing step that places recorded seismic signals to their subsurface origins is called *Seismic Migration* or *Seismic Imaging*.

Due to limited computing facilities in the past, post-stack migration of common-midpoint (CMP) processed data have been the conventional method to generate seismic depth images. This method was used especially by the exploration industry as oil and gas accumulations can usually be found in sedimentary layer sequences that often show simple geology. CMP post-stack migration works fine for plane and gently dipping reflectors but fails in regions with complex geology. For that reason and for the fact that computing facilities developed rapidly during the last three decades, other migration techniques replaced the standard CMP processing routines.

Today, *Kirchhoff Prestack Depth migration* is one of the widely used imaging methods. It works in complex geologic settings and can successfully be used in cases of irregular survey layouts. During Kirchhoff Prestack Depth migration the recorded wavefield is attributed to each potential reflection point in the subsurface according to its two-way traveltime. It can be said, that the wavefield is "smeared" along the corresponding two-way travel time isochrones. The true reflector is imaged where the two-way travel time isochrones interfere constructively. However, in cases of sparse sampling and limited aperture Kirchhoff Prestack Depth migration produces significant migration artefacts. In this case, the two-way travel time isochrones do not sufficiently interfere to produce a clear

seismic image of the reflector. For that reason, Görtz et al. (2003), Lüth et al. (2005) and Buske et al. (2009) propose to use the concept of *Fresnel Volumes* in order to restrict the migration operator (i.e. the two-way traveltime isochrones) to that particular subsurface region that physically contributes to the recorded reflection event. For this purpose, rays are traced into the subsurface according to the emergence angle of the recorded events. Then, the Fresnel Volume is calculated for each ray and the wavefield values are attributed to those particular subsurface points that are located within the first Fresnel Volume. This advanced imaging approach is called *Fresnel Volume migration*. The studies of Görtz et al. (2003), Lüth et al. (2005) and Buske et al. (2009) clearly show the advantages of Fresnel Volume migration compared to standard Kirchhoff Prestack Depth migration. Migration artefacts are significantly reduced and consequently reflectors appear more distinctive. Sick (2006) and Chalbaud (2010) applied both methods, Kirchhoff Prestack Depth migration and Fresnel Volume migration, respectively, to active seismic data sets from different sites along the Chilenean subduction margin. Both authors obtained precise depth images of the subduction environment that are more suitable for interpretation than the corresponding depth images produced by Kirchhoff Prestack Depth migration. Furthermore, Fresnel Volume migration succeeds in imaging steeply dipping reflectors where standard Kirchhoff Prestack Depth migration fails. This was shown by Gutjahr (2009) who used synthetic seismic data from a vertical reflector model and managed to successfully image the vertical reflector with Fresnel Volume migration.

Yoon (2005) showed that the quality of seismic depth images depends strongly on the considered wavelengths of the recorded seismic signals because heterogeneous zones in the subsurface cause scattering. The range of particular wavelengths thereby depend on the size of the heterogeneities. For this reason, the scattering characteristics of the subsurface can be characterized by performing the migration algorithm within discrete frequency bands. This approach is called *Reflection Image Spectroscopy*. Certain small-scale as well as large-scale structures can additionally be resolved that are usually superimposed by signals from different frequency ranges.

The present thesis aims to reprocess an old industry reflection data set using standard Kirchhoff Prestack Depth migration, Fresnel Volume migration and Reflection Image Spectroscopy. It shall be shown that the application of advanced imaging techniques on an old reflection data set is able to complement previous studies with new structural details from beneath the investigation area.

The data set used in the frame of this thesis is the industry reflection data set SJ-6 that has been acquired in 1981 in order to explore oil accumulations in the shallow crust of south central California, USA. Line SJ-6 is of valuable interest to the scientific community

because it crosses major parts of the prominent San Andreas transform fault system which is a major transform plate boundary separating the North American plate and the Pacific plate, respectively.

The San Andreas transform fault system is one of the most intensely studied plate boundaries in the world because it can be observed on land and is therefore more easily to access. Furthermore, the San Andreas fault system consists of many fault strands that are capable of producing large earthquakes that pose danger for citizens living near the fault zones especially those in large cities, for example San Francisco and Los Angeles, respectively. Various studies on the San Andreas fault aim to understand the mechanisms and processes that control the displacement of crustal blocks which is so far not yet completely understood, nor is its complex tectonic evolution. Additionally, the San Andreas fault system can be separated into many segments that all have different characteristics, for example with respect to adjacent geology, seismicity or fault dip.

Profile SJ-6 crosses the San Andreas fault near the small town Cholame where the seismic behaviour of two different segments changes from seismically locked (i.e. few large earthquakes) to transitional (i.e. aseismic creep, microearthquakes and intermediate recurring earthquakes). Along the transitional segment approximately 50 km north of Cholame the famous San Andreas Fault Observatory At Depth (SAFOD) is located which contains a borehole that was drilled directly through the San Andreas fault zone at approx. 3 km depth in order to examine the fault zone directly at the locations of earthquake hypocenters. The preliminary survey at SAFOD contained a 2D active seismic reflection/refraction data set (SAFOD2003) across the drilling site and the San Andreas fault zone. Buske et al. (2007) processed a limited portion of the full data set using Fresnel Volume migration. The resulting depth images show two distinct almost subvertical structures down to depth of approximately 4 km that are related to the San Andreas fault and the adjacent Buzzard Canyon fault.

The present work is strongly motivated by the studies of Buske et al. (2007) and Buske et al. (2009). The question came up how the San Andreas and other related faults appear in the seismic depth image at other locations of the fault system and how potential differences might be correlated to other geological or geophysical observations.

With a total extend of 180 km line SJ-6 is an exceptionally long profile line that crosses the major geomorphological units and fault zones in south central California, e.g. the Coast Ranges and the Great Valley as well as the Nacimiento-Rinconada fault zone, the San Andreas fault zone and the San Juan fault, respectively. Another interesting aspect about the SJ-6 data set is its location directly above a zone of high non-volcanic tremor activity. These seismic signals have firstly been described along the San Andreas fault

by Nadeau and Dolenc (2005). It is expected that non-volcanic tremor are related to processes in the deep San Andreas fault zone. Determined non-volcanic tremor locations (e.g. Shelly et al., 2009, Nadeau et al., 2009 and Ryberg et al., 2010) are so far uncertain and the processes that generate non-volcanic tremor signals are not yet understood. For that reason, many studies deal with these extraordinary seismic signals in order to gain an insight into the deep San Andreas fault zone.

The United States Geological Survey (USGS) fortunately made the full industry SJ-6 reflection data set available to the scientific community. It was shown in 1985 by several working groups (Walter et al., 1987) that the data set contains striking information not only on the shallow crust but also on the lower crust. However, only particular parts of the data set were available to the scientists and CMP post-stack processing was the standard imaging technique used in those days. Bloch et al. (1993) reprocessed a part of the SJ-6 data east towards the San Andreas fault using Prestack Migration techniques in order to investigate the tectonic evolution of the eastern Coast Ranges and the Great Valley but their seismic depth images only contain structural information on the shallow crust.

In the scope of this thesis, the full SJ-6 data set is reprocessed with the aim to image the whole crust with particular focus on the deep crustal structures of the San Andreas fault system. The major questions according to the San Andreas fault zone are: Does the fault can again be imaged as distinct subvertical feature in the shallow crust? What is the appearence of the fault in the lower crust and does it reach the Moho? Does the depth images show any indicators that correlate with non-volcanic tremor locations?

The depth images that are obatined by each of the three imaging techniques are compared to magnetotelluric investigation results that have been obtained across nearly the same profile line (Becken et al., 2011 and Tietze et al., 2013), to the seismic velocity structure (Thurber at al., 2006 and Lin et al., 2010) and to the local seismicity (Waldhauser and Schaff, 2008) as well as non-volcanic tremor locations (Nadeau et al., 2009).

The structure of the present thesis is as follows: Chapter 2 introduces the investigation area focusing on the main characteristics of the San Andreas fault zone according to its evolution and its seismic attributes. Furthermore, the most important geomorphological units along line SJ-6 are presented. Chapter 3 explains the theory behind the three applied imaging methods used in this thesis. It starts with the principle of Kirchhoff Prestack Depth migration followed by a discription of Fresnel Volumes and Fresnel Volume migration. Finally, the basic idea behind Reflection Image Spectroscopy is explained. Chapter 4 gives an overview on the data set. The exact location of line SJ-6 as well as the acquisition geometry and the recording parameter are introduced in section 4.1. Section

4.2 shows major results from selected previous studies that used parts of the same data set.

Line SJ-6 is partly crooked in some regions and shows a significant kink where it crosses the San Andreas fault. The imaging techniques are for that reason implemented in 3D and line SJ-6 is separated into two distinct segments according to the significant kink. The dimensions of the predefined subsurface models and the two segments are presented in section 4.3.1 followed by a characterization of the additionally required velocity model in section 4.3.2. The migration operator, namely the two-way travel time isochrones are then determined according to the brief description in section 4.3.3. Section 4.3.4 demonstrates the preprocessing steps that are applied to prepare the data for migration. Finally, it is explained how each single imaging approach is implemented on the data set and how reliable 2D depth images are produced from 3D migrated volumes under consideration of a crooked receiver line. Chapter 5 presents and compares the migration results of each migration approach for the two separate line segments according to the predominating geomorphological units along line SJ-6. A final reflector map is presented at the end of the chapter.

Finally, in chapter 6, the resulting depth images are discussed and partly interpreted by comparing it with other geophysical investigation results. The major aspects of this thesis are summarized und concluded in chapter 7.

2 Tectonic and Geological Setting

The western North American margin experienced several different tectonic plate interactions through historical time, each of them triggering geologic events that together formed a highly complex geology. The present-day tectonic setting along the western North American margin consists of a convergent plate boundary along the coast of Oregon, Washington and Canada as well as a transform plate boundary parallel to the Pacific coast of California, USA. There, the Pacific and the North American plates move past each other and form the prominent San Andreas transform fault system. The present chapter aims to give a brief and rather simple overview on the main characteristics of the San Andreas fault system and the geology of the investigation area in particular. The present-day geology is directly related to the tectonic processes that occurred prior to the initiation of the transform motion that later reshaped the geologic setting. Section 2.1.1 briefly illustrates the tectonic evolution of the western North Amercian margin and the San Andreas fault in particular. Section 2.1.2 summarizes the seismic character of the San Andreas fault system that is a direct consequence of active plate tectonics and bears a risk for residents along particular parts of the fault system. Recently, seismic signals called non-volcanic tremor have been observed along certain sections of the San Andreas fault system that are introduced shortly in section 2.1.3. The final section of this chapter deals with the most significant geomorphological units across the San Andreas fault system focusing on the area of investigation in south central California.

2.1 The San Andreas Fault System

The San Andreas transform plate boundary is located at the western margin of the North American continent and defines a large region that is affected by the transform motion of the oceanic Pacific plate against the continental North American plate. Thereby, the Pacific plate moves relatively northwestward past the North American plate with a rate of approximately 49 mm/yr (Thatcher, 1990).
The largest portion of this transform motion (approx. 75 %) is accomodated by the San

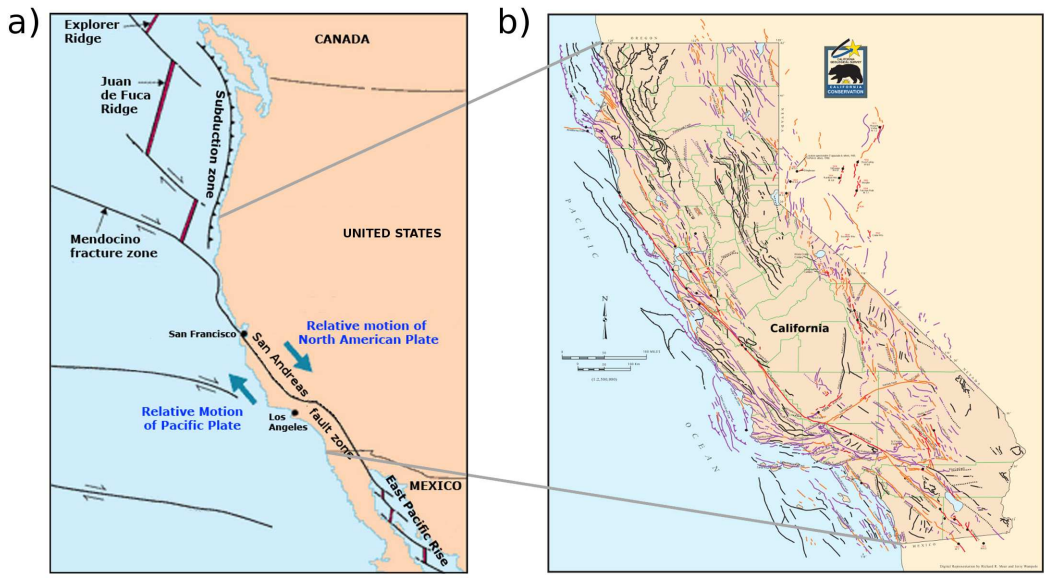

Figure 2.1: *a) The San Andreas fault system represents the transform plate boundary between the Pacific plate and the North American plate along the west coast of California, USA (Kious et al., 1996). b) A complex network of faults crosses California from northwest towards southeast defining the San Andreas fault system (modified after Jennings et al., 2002).*

Andreas fault system that is located nearly parallel to the Pacific Coast of California, USA. The rate of dextral strike-slip along the San Andreas fault system amounts to 33-37 mm/yr (Thatcher, 1990) resulting in an estimated total offset of 560 km (Irwin, 1987) since the transform plate boundary started to develope approximately 30 Ma ago. The extensive deformation as a result of transform plate motion can be observed across the San Andreas fault system along a region of 50 km to 100 km in width and more than 1000 km in length from Cape Mendocino north of San Francisco southeast towards the Gulf of California. A complex network composed of many faults developed within this region subparallel to the plate boundary where the San Andreas fault is designated as the main fault and therefore lends its name to that large transform plate boundary. Figure 2.1 a) illustrates the main trace of the San Andreas fault zone through California and Figure 2.1 b) gives an impression of the complex fault network that defines the San Andreas fault system.

The prominent San Andreas fault is a right-lateral strike-slip fault that can be traced from Cape Mendocino southeast towards the Gulf of California over a distance of 1.200 km. Near Cape Mendocino the San Andreas fault forms a triple junction with the Mendocino transform fault and the Cascadia subduction zone. Three lithosperic plates interact in this region and the transform system changes to subduction towards north.

On its way southeast from the Mendocino triple junction to the Gulf of California the San

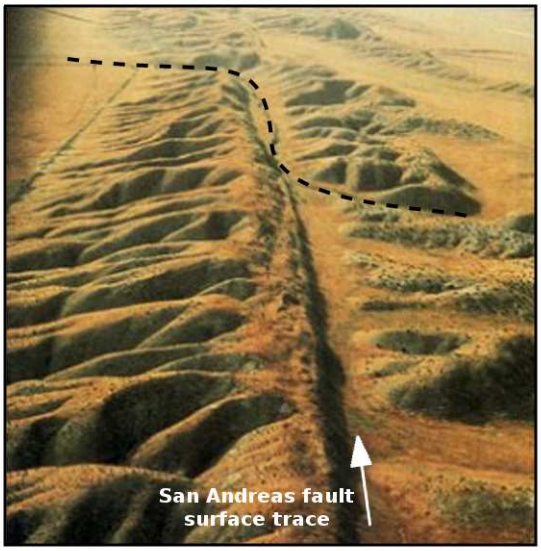

Figure 2.2: *The San Andreas fault is characterized by a significant scar that can be observed at the surface through almost the length of California. The dashed black line demonstrates the offset of a drainage pattern due to strike slip movement along the fault (Kious et al., 1996).*

Andreas fault cuts through diverse rock types and regional structures. In its central part the San Andreas fault is relatively straight and separates contrasting crustal elements that differ significantly in age and lithology. The southern section of the San Andreas fault contains a bend towards east near Los Angeles.

The overall strike-slip movement along the San Andreas fault is locally accompanied by a relevant component of compression perpendicular to the strike of the fault. The direction of strike slip movement along the fault differs by approximately 6 ° from the direction of relative plate movement of the transform system (Eaton and Rymer, 1990).

Along the surface the San Andreas fault zone can be observed by linear landforms and a great scar that is existent through most of California. Linear rigdes and valleys are oriented subparallel to the plate boundary. Different lithologies on either side of the fault indicate the past displacement of crustal blocks against each other. Respective surface expressions resulting from the displacement are offset streams as illustrated in Figure 2.2. It is possible that the offset shown in Figure 2.2 may have been forced by one large earthquake or propably by multiple earthquakes over the past million years. Other surface indicators of the fracture zone can directly be observed by en echelon or linear cracks in some regions as well as offsets in formerly straight fences and damaged buildings that have been built directly upon the fault. And of course, the present plate movement can directly be experienced by moderate to large earthquakes.

2.1.1 Evolution

The evolution of the San Andreas transform system was initiated approximately 30 Ma ago. By then the ancient oceanic Farallon plate was subducted eastward beneath the North American continent since Pangaea broke apart approximately 200 Ma ago. Where the Farallon plate adjoined the Pacific plate, new oceanic crust was produced along the East Pacific rise, an oceanic ridge system. Figure 2.3 a) schematically illustrates this situation. The spreading center of the East Pacific rise is marked by the thick red line. With the time, the rate of subduction between the North American plate and the Farallon plate exceeded the spreading rate at the ridge system farther west. Consequently, the North American plate started to override the spreading center causing the Farallon plate to progressively destruct as can it be seen in Figure 2.3 b). Two triple junctions developed at the edges of the contact zone between the Pacific and the North American plates, the Mendocino triple junction (M in Figure 2.3) and the Rivera triple junction (R in Figure 2.3), respectively. While subduction of the Farallon plate continued northwestward and southeastward to the triple junctions, the latter started to migrate towards northwest and southeast, respectively, approximately 20 Ma ago. Since then, the right lateral San Andreas transform fault formed in between the migrating triple junctions (see Figures 2.3 c)-e)). The above given description of the San Andreas fault evolution only highlights the main aspects of a very complex and long process. Even today, this process is not yet fully understood and continues to be a subject of intense research. The reader is referred

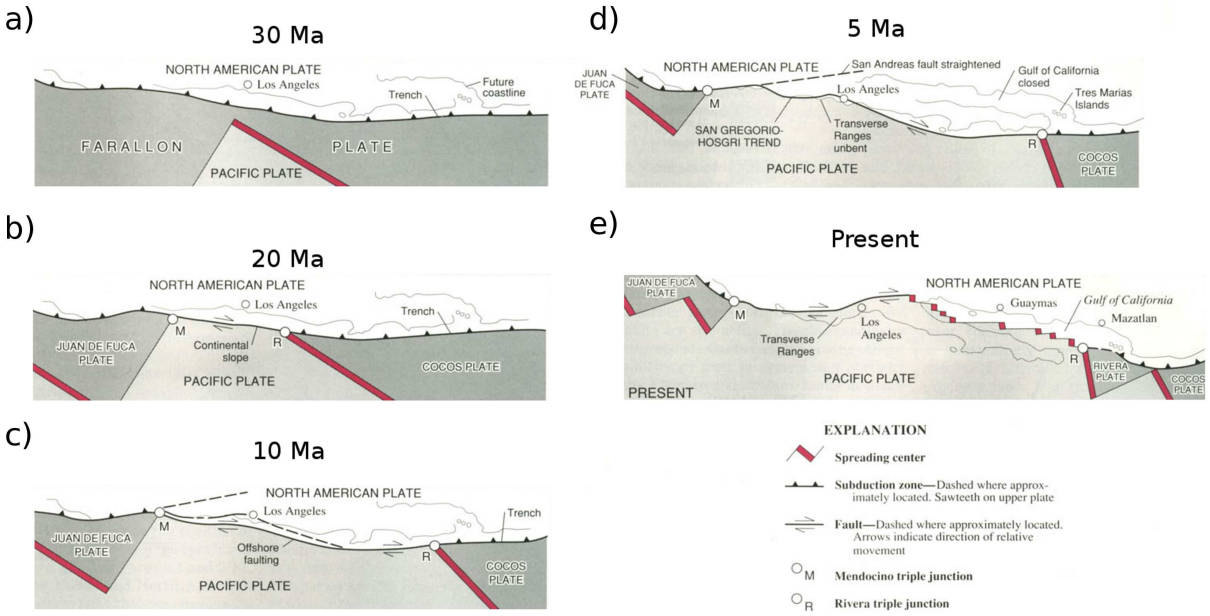

Figure 2.3: *Cenozoic plate tectonic evolution of the San Andreas transform fault system (Irwin, 1990).*

to Irwin (1990), Brown (1990) or Atwater (1970) who studied and summarized the main aspects of the San Andreas fault Cenozoic tectonic evolution in detail. Popov et al. (2012) simulated 20 Ma of San Andreas fault evolution in order to find possible mechanisms that explain an observed migration of the active San Andreas fault zone towards east during this period.

2.1.2 Seismicity

The motion of the lithospheric North American and Pacific plates against each other generates stresses and accompanying strain within the adjacent crustal blocks along the plate boundary. The global tectonic stress forces the plates to move against each other but friction between the adjacent crustal blocks causes these to stick together. When friction exceeds, the crustal blocks slip against each other and stress is locally released by earthquakes of different magnitudes. Figure 2.4 shows the San Andreas fault main trace and seismic events (blue points) recorded in the years between 1984 and 2011 that have been relocated by Waldhauser and Schaff (2008). The San Andreas fault zone itself can be subdivided into segments that significantly differ in its seismic behaviour. The red segments in Figure 2.4 have ruptured in historical times and generated large earthquakes, like the 1906 San Francisco earthquake and the 1857 Fort Tejon earthquake, both with a magnitude of approximately 7.9. The San Francisco 1906 and the Fort Tejon 1857 earthquakes are marked by white stars in Figure 2.4. Both segments are supposed to be locked until the accommodated strain exceeds the frictional strength of the crustal blocks and sudden slip causes the next large earthquake. Tectonic activity in Central California is characterised by aseismic creep, shallow microseismic events and few recurring M6 events located between the two locked segments. The so-called creeping segment is illustrated by a green fault line in Figure 2.4. Historical creep rates are 32 mm/yr along this 132 km long section (Bryant et al., 2002). The adjacent crustal blocks slip constantly or periodically against each other. Large earthquakes have not been reported from this fault segment and it is unlikely that they will occur in the future as local plate motion is almost completely accomodated by the long-term slip (Hill et al., 1987). Microseismic activity is rather high along the creeping section of the fault compared to the locked fault segments. Maximum depths of microseismic events have been located not deeper than 13 km along the creeping segment and 15 km along the creeping to locked transition zones (Waldhauser and Schaff, 2008). For this reason and because of the narrow distribution of microseismic events beneath and around the faults surface trace, the San Andreas fault can seismically be defined as a near vertical structure down to depth of 15 km. The shallow seismicity is associated with the brittle upper crust that is characterized by

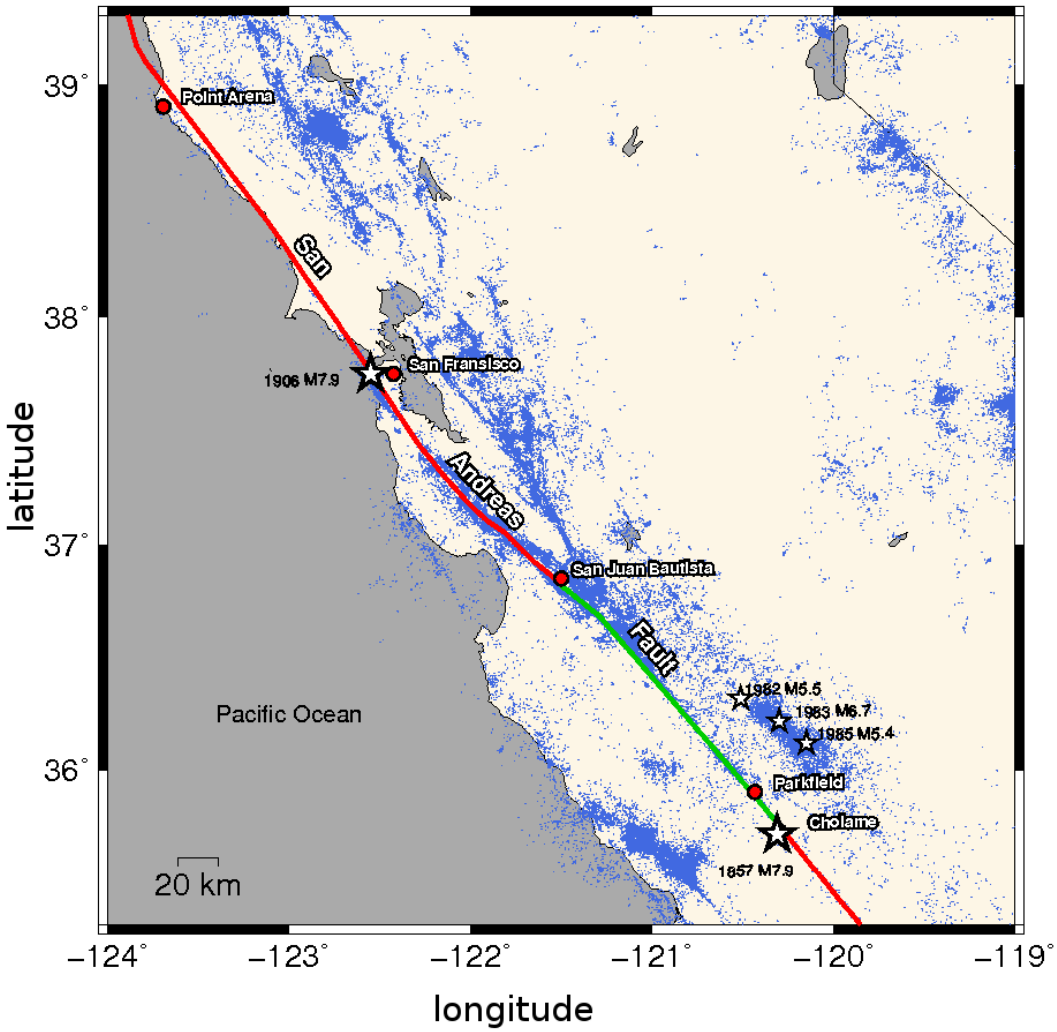

Figure 2.4: *Seismic activity map showing seismic events (blue dots) recorded in the years between 1984 and 2011 relocated by Waldhauser and Schaff (2008). The San Andreas fault locked segments are indicated by red lines and the creeping segment by the green line, respectively. White stars mark the epicentres of the M7.9 1906 San Francisco, the 1857 Fort Tejon, the 1982 M5.5 New Indria, the 1983 M6.7 Coalinga and the 1985 M5.4 Kettleman Hills earthquakes, respectively.*

prevalent elastic deformation. From the so far aseismic lower crust it is inferred that plastic deformation predominates in the ductile part of the crust.

The seismic activity map shows several bands of seismicity that strike subparallel northeast and southwest to the San Andreas fault. The structures there are capable of producing relatively large earthquakes such as the M6.7 Coalinga and the M5.4 Kettleman Hills earthquakes. These seismic events are associated with reverse and thrust fault earthquakes that occur at the western and eastern flanks of the California Coast Ranges. Eaton and

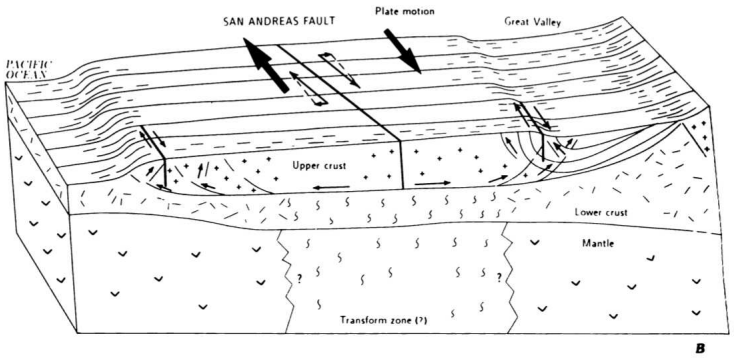

Figure 2.5: *Seismotectonic model from Eaton and Rymer, 1990.*

Rymer (1990) proposed a seismotectonic model that is illustrated in Figure 2.5. They presume the Coast Ranges to be underlain by a transform zone in the mantle and a ductile lower crust that borders a mechanically stronger lower crust at the edges of the Coast Ranges. The brittle upper crust above is supposed to be decoupled from the lower crust and mantle along subhorizontal detachements that generate thrust and reverse fault earthquakes when reaching the brittle upper crust at the flanks of the Coast Ranges.

2.1.3 Non-volcanic tremor

The San Andreas fault zone is one of the most intensely studied faults in the world. Seismic receiver density along the fault is therefore high, especially along the creeping segment. Along particular segments of the fault low amplitude, high frequency seismic signals have been detected amongst the seismic recordings. The same kind of signals have previously been detected along subduction zones in southern Japan and Cascadia (Obara, 2002) and are called non-volcanic tremor. Figure 2.6 illustrates the non-volcanic tremor activity since 2005 (Nadeau and Dolenc, 2005 and Nadeau et al., 2009). Non-volcanic tremor locations are marked as blue dots. The non-volcanic tremor activity is increased along the creeping segment of the San Andreas fault and highest at the southeastern transition from the creeping into the locked segment. Identification and location determinations of non-volcanic tremor is a challenging task because these signals lack clear P- and S-phase arrivals. They occur spontanously or can be triggered by local earthquakes and by teleseismic earthquakes. The duration of non-volcanic tremor is variable and can last from several minutes up to days. At subduction zones non-volcanic tremor are supposed to be related to slow-slip events in the subducted crust that are induced by dehydration processes. The processes that are related to non-volcanic tremor generation along the San Andreas fault remain unknown. It is speculated that these processes might be fluid

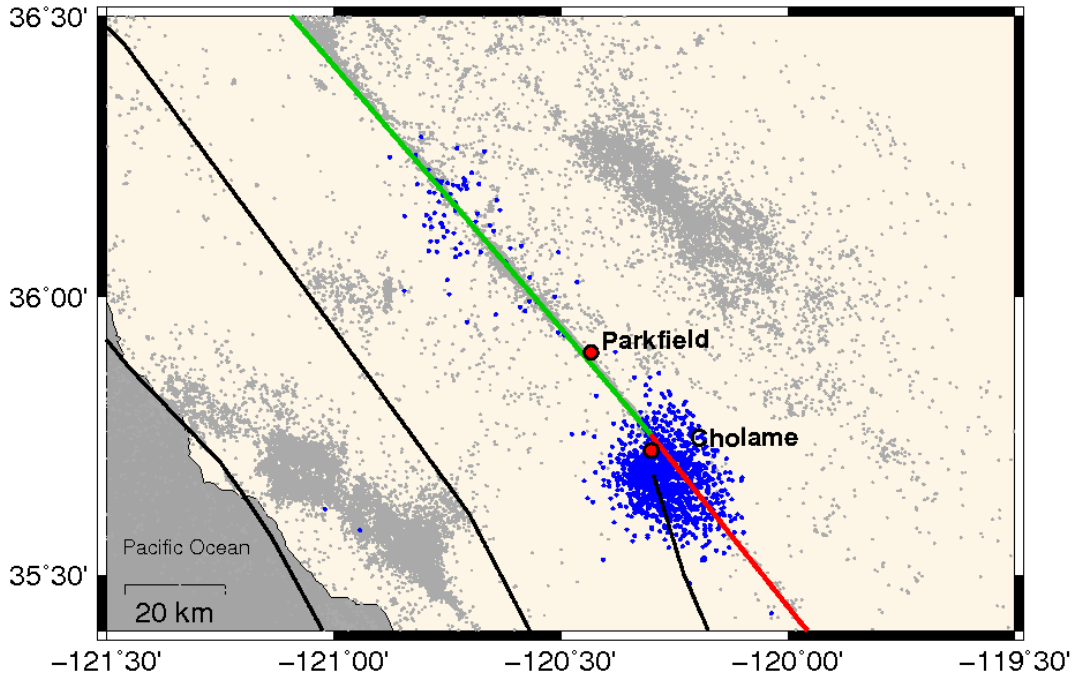

Figure 2.6: *Non-volcanic tremor locations in South Central California (Nadeau et al. ,2009). Blue dots are non-volcanic tremor locations, gray dots are seismic events (Waldhauser and Schaff, 2008).*

driven. As clear body wave phase arrivals can not be detected diverse location approaches have been developed by different working groups. The results are not consistent and yield in diverse interpretations. According to Nadeau et al. (2009) non-volcanic tremor are widely distributed within and adjacent to the San Andreas fault zone. Thereby higher non-volcanic tremor activities are concentrated slightly west of the fault. The location results from Shelly et al. (2009) show non-volcanic tremor events that are mostly aligned within the deep fault zone. Both groups located the non volcanic tremor events in the lower crust beneath the seismogenic zone and presume a direct relationship to the deep San Andreas fault concluding that the fault zone is a distinct feature that intersects the entire crust. Locations by Ryberg et al. (2010) are parallel to, but offset towards southwest from the San Andreas fault. Rubinstein et al. (2010) presents two physical models that aim to explain the generation of non-volcanic tremor, a fluid-flow model and a frictional model, respectively. The frictional model explains non-volcanic tremor as a result of slow-slip events whereas the fluid-flow model attributes fluid processes to non-volcanic tremor generation. Nevertheless, further studies of non-volcanic tremor events might reveal important information on the processes that are related to the deep crust which are so far poorly understood.

2.2 Geomorphic Provinces of South Central California

California is subdivided into eleven geomorphic provinces as illustrated in Figure 2.7. Each province is characterized by distinct features such as landforms, climate, geology or topography. The following section focuses on the geology of three particular provinces and its specific subregions that are located across the area of interest in south central California that is indicated by the black rectangle in Figure 2.7. This particular region contains the California Coast Ranges, the Great Valley and the foothills of the Sierra Nevada.

Much of the present day rock units in California developed as a result of Mesozoic subduction processes. Cenozoic strike-slip movement deformed these rocks and displaced most of the rock units out of its original locations. Many faults have been involved over specific periods of time resulting in a complex pattern of neighbouring geologic units of different origin and age. Therefore, reconstruction of Californias geological history is a challenging work to do.

For more information on the evolution and the geological structure of the San Andreas fault system and western North America the reader is referred to Irwin (1987) as well as Page et al. (1998) to name but a few. As mentioned before, a wide variety of interesting literature can be found on various topics relating to the San Andreas fault system.

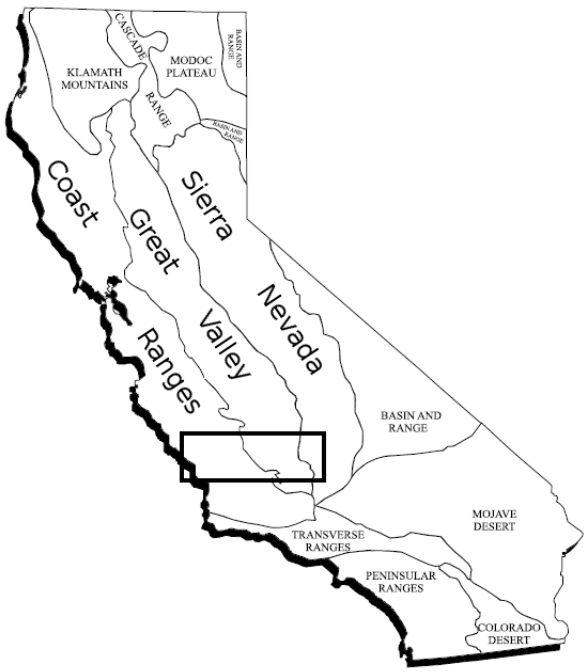

Figure 2.7: *California geomorphic provinces (California Geological Survey, 2002). The black rectangle marks the area of interest.*

2.2.1 The California Coast Ranges

The California Coast Ranges are characterized by mountain ranges and valleys that are located between the Pacific coast and the Great Valley. Tending nearly subparallel to the San Andreas fault zone the Coast Ranges extend over a distance of approximately 300 km in northwest-southeast direction and up to 50 km perpendicular to this. The mountain ranges can achieve elevations of 1200 m in some regions. Due to the compressional deformation across the plate boundary the Coast Ranges are still undergoing folding and thrusting (Page et al., 1998). It is suggested that uplift of the Coast Ranges was initiated after the passage of the Mendocino triple junction towards northwest. While the northern Coast Ranges are mainly composed of rocks from the so-called Franciscan Block, the southern Coast Ranges additionally include a large block of mainly granitic composition, the Salinian Block.
Beside the famous San Andreas fault the California Coast Ranges contain series of almost parallel faults that belong to the San Andreas fault system, for example the Nacimiento fault, the Rinconada fault and the San Juan fault in South Central California.

Franciscan Block

The Franciscan Block is a heterogeneous assemblage of various rock types including graywacke, sandstone, limestone, chert as well as volcanic rocks and metabasalts. The Franciscan rocks represent an accretionary assemblage that formed during the Mesozoic subduction process at the front side of the overriding lithospheric plate. Deep sea sediments and parts of oceanic crust were accreted to the continent and formed an accretionary wedge that underwent large deformation. The basement rocks of the Franciscan Block are overlain by Cretageous, marine Tertiary and continental Quaternary sedimentary sequences. Locally Franciscan rocks are overlain by Great Valley Sequence rocks that are similiar in age but differ in lithology compared to the Franciscan rocks. In south Central California Franciscan rocks are located west to the Nacimiento fault and east to the San Andreas fault. In between, rocks of the Salinian Block have been brought into contact to the Franciscan Blocks by transform motion along the San Andreas and Nacimiento fault, respectively. The western and the eastern Franciscan Block differ significantly in age and metamorphic grade. According to Godfrey et al. (2000) the western block is younger (Late Cretaceous to Miocene) and exhibits lower metamorphic grade than the eastern block (Late Jurassic to middle Cretaceous).

Salinian Block

The Salinian Block is an allochthonous block composited of plutonic and metamorphic

rocks (Page et al., 1998). It is located between the Nacimiento fault and the San Andreas fault where it is in fault contact with Franciscan rocks on its western and eastern margin, respectively. The composition of the rocks of the Salinian Batholith is similiar to the plutonic rocks of the Sierra Nevada. It is assumed that Salinian rocks and Sierran rocks have the same origin farther south of the present position of the Salinian Block. The Franciscan rocks clearly differ in composition and evolution from the Salinian rocks. As the Franciscan rocks are unaffected by late Cretageous plutonism within the Salinian Block it is assumed that large fault displacements have taken place, resulting in the movement of the Salinian Block against Franciscan rocks. The igneous basement rocks of the Salinian Block are covered by Cretageous to Tertiary marine sedimentary rocks and by non-marine Quaternary rocks (McBride and Brown, 1986).

Coast Range Ophiolite

Coast Range ophiolite outcrops have been found along the entire length of the California Coast Ranges. Ophiolites are remnant parts of oceanic crust or possibly upper mantle that have partially been accreted onto the continental crust. During the uplift of the Coast Ranges they were elevated to the surface. Ophiolites are mainly composed of ultramafic, mafic and minor felsic igneous rocks of Jurassic age. Sequences of Coast Range ophiolites lie between Franciscan rocks and sedimentary rocks of the Great Valley Sequence. The contact between Franciscan rocks and the Coast Range ophiolites (or where missing rocks of the Great Valley Sequence) is marked by a mostly east dipping fault, namely the Coast Range fault. Today, discussions about the origin and evolution of Coast Range ophiolites continue and are subject to a number of investigations. The reader is referred to Bailey (1970) and Shervais (1985) or Choi et al. (2008) for further readings on ophiolites.

2.2.2 The Great Valley

The Great Valley is a large basin that is aligned in north-south direction parallel to the California Coast Ranges. The eastern margin of the Great Valley abuts to the Sierra Nevada mountain range and the western margin to the Coast Ranges, respectively. The Great Valley is separated into the northern Sacramento Valley and the southern San Joaquin Valley. During the Mesozoic subduction processes the Valley originated below sea level along the Farallon-North American plate boundary. These processes caused depression and sedimentation of marine deposits. Though, the Great Valley included a fore-arc setting in Mesozoic time until subduction ceased. The western San Joaquin Valley is assumed to be underlain by a wedge of Franciscan rocks that proceeds eastward

due to compressive components of deformation (Walter et al., 1987 and Wentworth et al., 1984). The basement of the eastern San Joaquin Valley is presumably composed of mafic rocks of the so-called Great Valley ophiolite as proposed by Godfrey et al. (1998) and Fliedner et al. (2000). The geologic composition and the pre-Cenozoic tectonic history of the Great Valley basement are not yet completely understood.

Great Valley Sequence

The Great Valley Sequence sediments have been deposited in the fore-arc basin environment during Mesozoic subduction processes. Most of the deposits have been transported from the Sierra Nevada mountain site. Great Valley Sequence rocks lay upon Franciscan rocks in the eastern Coast Ranges and partially in the western Coast Ranges. The age and lithology is similiar to sediments of the Franciscan, but unlike the Franciscan rocks the Great Valley Sequence rocks are intact and less deformed. Their age is dated from Late Jurassic to Cretageous. Most of the Great Valley Sequence consist of mudstone, sandstone and conglomerate. Sandstones are suggested to be deposited from turbidity currents. The sediments have been deposited into shallow seawater environment and are likely to contain abundance of oil and gas.

Great Valley Ophiolite

Ophiolites as previously described above are suggested to form the basement of the Great Valley. Godfrey et al. (1998) analyzed various of geophysical data sets and concluded that the sedimentary strata of the Great Valley lie upon mafic and ultramafic material that he referred to as Great Valley ophiolite that may be related to the Coast Range ophiolite. Beneath the San Joaquin Valley the ophiolitic section is presumably 10-12 km thick. It is not yet clear whether the Great Valley ophiolite originated from an intraoceanic island arc crust or from oceanic crust. Furthermore, it could not be distinguished if the ophiolitic section consists purely of crust or if there are components of oceanic mantle material. According to his investigations Godfrey et al. (1998) derived possible scenarios for the pre-Cenozoic evolution of the western North American plate boundary.

2.2.3 The Sierra Nevada

The Sierra Nevada is a large mountain system that trends northwest through California over a distance of 700 km. The orientation of the Sierra Nevada is the result of Mesozoic subduction processes. Magma intruded into the upper North American plate during subduction of the Farallon plate and built up a magmatic arc. The magma was emplaced

into older rocks that have been deformed and metamorphosed. Large bodies of plutons formed the Sierra Nevada Batholith that is in many places exposed today as uplift resulted in erosion of sedimentary and volcanic rocks.

The area of interest of this work includes only the western foothills of the Sierra Nevada in south central California. The Sierra Nevada foothills are located towards east adjacent to the Great Valley. In south central California the foothills comprise in principal granitic and metamorphosed rocks.The geology of the Sierra Nevada and the Sierra Nevada foothills is very complex as diverse geologic events formed the present rock units and moved it to its present day locations.

3 Applied Methods of Seismic Imaging

Seismic migration is the process that places recorded seismic signals to their subsurface origins in order to create an image of the subsurface structures. These structural images are further used to interpret the imaged structures for the shape, size and distribution of geologic structures and to identify the location and orientation of characteristic subsurface features such as faults and major lithological boundaries. While migration provides information on the spatial orientation an distribution of subsurface structures, additional processing techniques such as Amplitude versus Offset (AVO) yield supplementary information on characteristic parameters of the geological units.

Active seismic experiments use controlled seismic sources to generate elastic waves that propagate downward through the subsurface (see Figure 3.1). The propagation velocities of the waves depent on the elastic properties of the subsurface rocks. The downward travelling waves are partly reflected and refracted at suburface heterogeneities where the contrast of the acoustic impedance is high enough. The acoustic impedance is defined as the product of the materials specific parameters seismic velocity and density. The upward travelling reflected portion of the wavefield is recorded at the surface as a function of

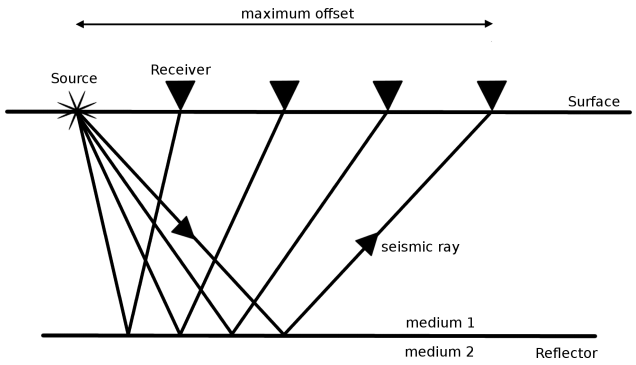

Figure 3.1: *Simple survey line layout of an active seismic experiment. The wavefield is reflected when the contrast of acoustic impedance between medium 1 and medium 2 is high enough.*

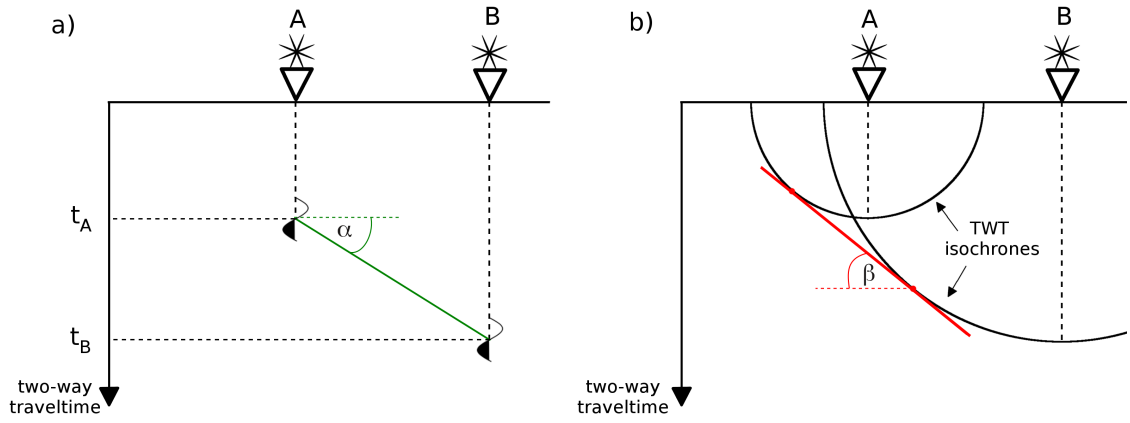

Figure 3.2: *Principle of Seismic Migration (after Yilmaz, 1987). a) Reflection events recorded at receiver A and B at different two-way travel times (TWT) t_A and t_B indicate a dipping reflector, b) migration yields the true spatial position and dip β of the corresponding reflector (red line).*

travel time along predefined receiver lines or arrays. In the following, the term *reflection* will be used in order to describe coherent seismic reflection signals that are recorded and displayed in the time section whereas the term *reflector* is used for the interface or subsurface structure that accounts for the recorded reflections at certain depths. The shape of the reflections is given by the intervals in which the signals are recorded at different stations. The term *offset* defines the distance between the source point position and the receiver location.

In a *zero-offset* experiment, that means that the source and the receiver are placed at the same location, a horizontal reflector can be identified by horizontal coherent reflection signals in the time section if the wavefield generation is repeated at different surface positions. A *finite-offset* time section displayes a reflection hyperbola, when the source point is fixed in one location. The larger the offset, the longer becomes the travel path of the waves and hence the travel time. In the case of dipping reflection events or more complex reflection structures in the time section, the shape of the related subsurface reflector is so far unknown. Seismic migration therefore aims to solve this problem by determining the true subsurface positions of recorded reflection signals.

The basic principle of migration is rather simple. Figure 3.2 a) illustrates two stations A and B in a zero-offset set-up. The difference of the arrival times (t_A and t_B) of the reflection response at the stations A and B is obviously generated at a dipping subsurface reflector. The connection of both recorded events in the time section gives a straight travel time curve with the dipping angle α.

The true dip β of the corresponding reflector is so far unknown but can be reconstructed by drawing the *two-way travel time* isochrones (i.e. the time the wavefield needs to propagate from the source to the reflection point and back to the receiver) around each station. Each point located on the two-way travel time isochrone is a potential reflection point in the subsurface that might be the origin of the recorded reflection response. The location of the true reflector is obtained by constructing a straight line that tangentially strikes both isochrones (red line in Figure 3.2 b). The relation between α and β is formulated by the so-called migrators equation: $\tan\alpha = \sin\beta$ (Sheriff, 1991). This procedure is simple in the case of small data volumes and simple reflector shapes but becomes very complicated when realistic situations are considered.

Today, seismic surveys are very complex and provide large data volumes. Moreover, complex velocity models have to be taken into account that represent the true velocity structures as precisely as possible. All in all, seismic migration is a far more complex process as illustrated above because it actually means to solve an inverse problem for the location and the orientation of subsurface reflectors .

A variety of approaches have been developed in order to obtain detailed images of the geological and tectonic structures, whereas the suppression of artefacts and the enhancement of resolution are still subject to various studies. Throughout this thesis a dynamic migration approach is used to obtain structural subsurface information from seismic reflection data. Dynamic migration approaches are based on wave theory and contain in principle two steps. First, the recorded wavefield is backpropagated into the subsurface. The second step places the recorded energy to the corresponding subsurface points depending on the particular travel times of the waves between the source and each subsurface point.

Three main techniques are commonly used for wavefield backpropagation: Kirchhoff methods (Schneider, 1978), Fourier methods (Gazdag, 1978) and Finite Difference methods (Claerbout, 1976). In the scope of this thesis, Kirchhoff Prestack Depth migration and the so-called Fresnel Volume migration approach are performed in order to obtain structural subsurface information. The Fresnel Volume migration approach was developed in order to improve the image quality compared to standard Kirchhoff Prestack Depth migration by significantly reducing migration artefacts. Kirchhoff Prestack Depth migration as well as the advanced Fresnel Volume migration approach are introduced in sections 3.1 and 3.2, respectively.

Additional structural details can be obtained by migrating discrete narrow-frequency bands that are previously extracted from the data which has been shown by Yoon (2005). This approach is called Reflection Image Spectroscopy and will be introduced in section 3.3.

3.1 Kirchhoff Prestack Depth Migration

Kirchhoff migration techniques are based on the solution of the high-frequency approximation of the wave equation which is the Kirchhoff integral.
In 1954, Hagedoorn showed that reflections can be migrated graphically by creating the envelope of equal travel time curves as has been shown in the previous section. The equal travel time curve depicts all points that represent a possible reflection source for a given source-receiver pair. The curves are constructed by drawing circles that pass through the arrivals on the seismic traces and are centered at $t = 0$.
The envelope of all equal travel time curves forms the image of the corresponding reflector. The process is illustrated in Figure 3.3. Hagedoorn's concept is the basis for diffraction stack migration and therefore Kirchhoff Prestack Depth migration. The relation of Haagedorn's graphical migration approach and modern Kirchhoff migration is presented in the publications of Bleistein (1999) and Bleistein and Gray (2001).
The following section shortly summarizes the major aspects of diffraction stack migration as the basis of modern Kirchhoff migration techniques.

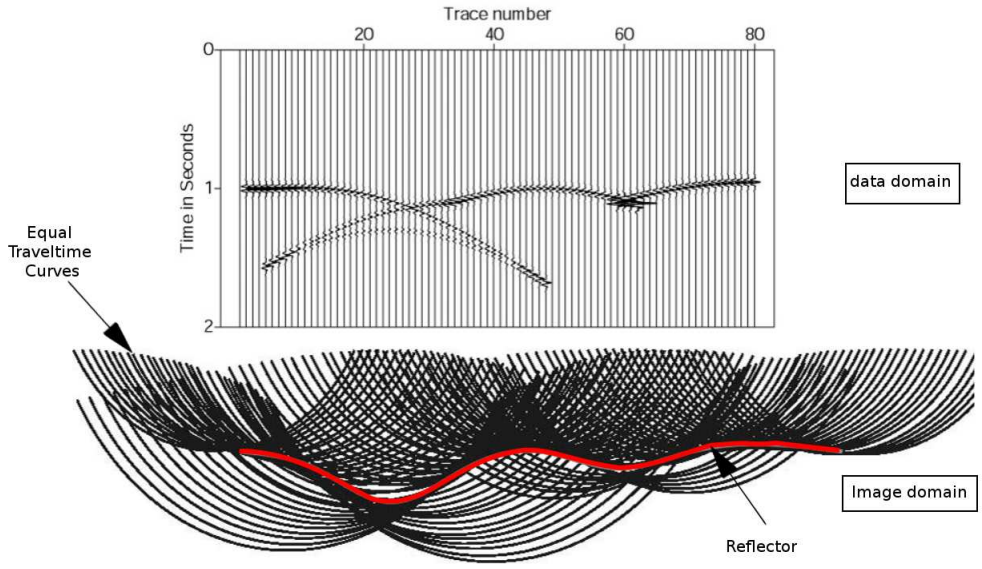

Figure 3.3: *Schematic representation of Hagedoorn's method to synthetic data of a syncline model (Bednar, 2005). Top: Synthetic time section; Bottom: Superposition of equal travel time curves (black circles) forms the image of the reflector (red curve).*

Diffraction Stack Migration

The diffraction stack method, as based on Hagedoorns migration approach, follows Huygens' principle, stating that every single reflection point that is hit by a wave becomes the source of a secondary wavefield (diffracted wavefield). Figure 3.4 represents the case of a single diffraction point $P(x, z)$ in the subsurface, in the following called the *image domain*. A seismic signal propagating from a single source S at the surface into the subsurface is diffracted at $P(x, z)$ and produces a secondary wavefield according to Huygens' principle. The secondary wavefield propagates back from $P(x, z)$ to the surface where it is recorded at certain receivers (r_1 to r_6). In the time section, called *data domain*, the recorded events define a diffraction hyperbola (red line) providing the respective two-way travel times of the arriving wave. The two-way travel time in the data domain contains the important information on how long the wave travelled from the source to each resepective receiver ($t = t_s + t_{r_i}$, $i = 1, .., 6$). The shape of the diffraction curve depends on the subsurface velocity, on the position of the diffraction point and the source-receiver configuration at the surface. Provided that subsurface velocities are known or pre-estimated, diffraction curves for any particular subsurface point can be calculated for a given survey geometry.

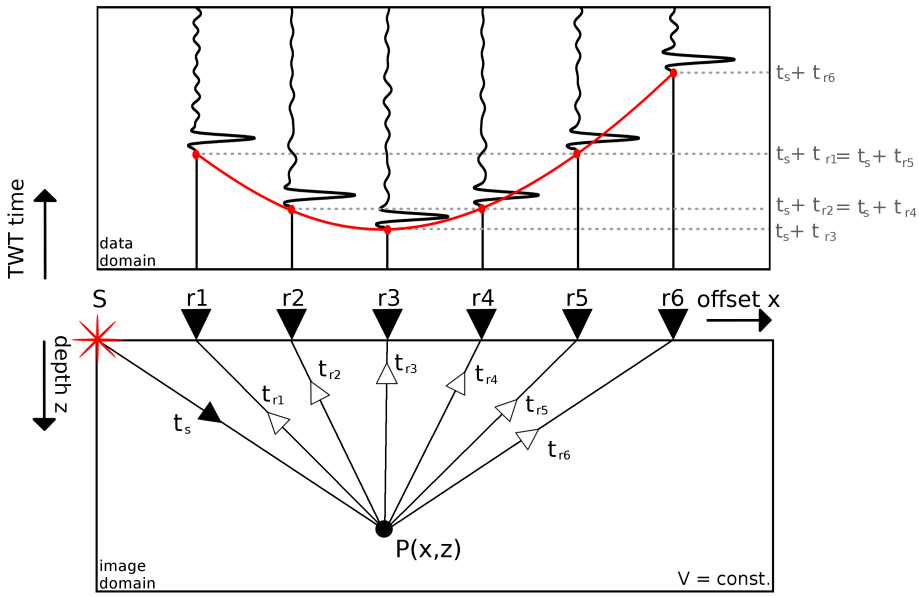

Figure 3.4: *Diffraction stack migration sums the amplitudes along the diffraction hyperbola in the finite-offset time section and attributes the sum to the considered subsurface point $P(x, z)$.*

Diffraction stack migration then sums the amplitudes along all diffraction curves and assigns the sums to the corresponding subsurface points in the image domain. Considering all source receiver configurations, the results will then interfere constructively along the true recorded diffraction curves and destructively elsewhere. In the example of Figure 3.4 the sum of amplitudes will be maximal for diffraction point $P(x, z)$ and minimal for all other points as they do not contribute as secondary sources. This procedure can similarly be applied to reflection events. Reflection events can be assumed as a superposition of diffraction curves in the data domain and as closely spaced diffraction points in the image domain.

Kirchhoff Migration

Kirchhoff migration is a weighted diffraction stack where the amplitudes are corrected for geometrical spreading and obliquity in advance.

The backpropagation of the recorded wavefield into the subsurface is realized by an approximation of the 2D Kirchhoff equation which is an integral form of the 2D wave equation. The 2D Kirchhoff equation mathematically describes the wavefield at any particular subsurface point as the superposition of wavefield contributions from surrounding points and earlier times (Sheriff, 1991). The aim of migration is to determine the subsurface position of the wavefield at the time when the reflection occurred. As the wavefield is recorded at the surface the Kirchhoff equation can be reduced to the Kirchhoff migration integral that provides the wavefield $U(\vec{x}, t(\vec{x}))$ at any point $P(\vec{x})$ in the subsurface at the time of reflection $t_S = t - t_R$ beneath the acquisition surface A:

$$M(\vec{x}) = U(\vec{x}, t_S(\vec{x})) = \int\int_A W(\vec{x}, \vec{x}')\ \dot{U}(\vec{x}', t_S + t_R)\ \ d\vec{x}' \tag{3.1}$$

$t = t_S + t_R$ is the two-way travel time that the wavefield needs to propagate from the source to the reflection point (t_S) and from the reflection point to the receiver (t_R). The wavefield $M(\vec{x})$ at image point $P(\vec{x})$ is determined by stacking the time derivatives of the recorded wavefield $\dot{U}(\vec{x}', t_S + t_R)$ at the surface $\vec{x}' = (x, z = 0)$. The weight function $W(\vec{x}, \vec{x}')$ accounts for the correct treatment of the amplitudes during the backpropagation of the wavefield. In this thesis the approximated Kirchhoff migration represented by equation 3.2 is used and corresponds to the weighted diffraction stack migration.

$$M(\vec{x}) = U(\vec{x}, t(\vec{x})) = \int_{-\infty}^{\infty} U(\vec{x'}, t_S + t_R) \cdot W(\vec{x}')dx' \tag{3.2}$$

In practice, an a priori velocity model is used to determine the two-way travel times for each image point $P(x, z)$ and each particular source-receiver pair configuration. In

the majority of cases the recorded amplitudes are corrected for geometrical spreading in the preprocessing process prior to migration. During migration, the amplitudes are then attributed to each point $P(x, z)$ that is a possible diffractor of reflection energy, that means amplitudes are smeared along the corresponding two-way travel time isochrones. In the actual imaging step, amplitudes associated with the same subsurface point $P(x, z)$ are summed so that they interfere constructively at actual diffraction points and destructively elsewhere. This approach is referred to as Kirchhoff Prestack Depth migration since the migration is applied in the prestack domain because migration is performed on each single shot gather separately. Afterwards the single migration results are stacked to obtain one final migrated depth section in order to improve the signal-to-noise ratio.

The above described imaging technique has proven effective especially in complex geologic settings and for surveys with varying acquisition parameters. High quality images can only be obtained if the interference of isochrones is sufficiently good. Most likely this is not the case for low coverage or limited aperture. The image result can then sigificantly be affected by migration noise and artefacts. Furthermore, this imaging technique is not suitable for imaging steeply dipping reflectors.

3.2 Fresnel Volume Migration

In the following, an advanced migration approach will be introduced that is able to enhance the image quality significantly compared to standard Kirchhoff Prestack Depth migration. The so-called Fresnel Volume migration approach was proposed by Görtz et al. (2003) and Lüth et al. (2005) as an extension to standard Kirchhoff Prestack Depth migration. The basic concept of this approach is to estimate the travel path of recorded energy and to locally restrict the migration operator (two-way travel time isochrone) around to the vicinity of the travel path. Thus, the standard Kirchhoff Prestack Depth migration scheme is extended by a ray tracing procedure that subsequently determines Fresnel Volumes in order to provide the criterion for the restriction of the migration operator. In the following, the concept of Fresnel Volumes and the method of Fresnel Volume migration will be introduced.

The concept of Fresnel Volumes

In ray theory, rays are approximated as infinitely narrow lines as long as frequencies are assumed to be infinitely high. In reality, recorded data contain finite frequency ranges. According to each frequency the recorded wavefield propagates inside a finite region around the graphical ray of the high frequency approximation (Spetzler and Snieder, 2004). This extended region is the so-called Fresnel Volume (Figure 3.5). The concept of Fresnel Volumes originates from physical optics and radio communication. However, the concept is also valid for seismology and seismics as for all problems concerning the radiation of waves. The area that intersects the Fresnel Volume perpendicular to the propagation

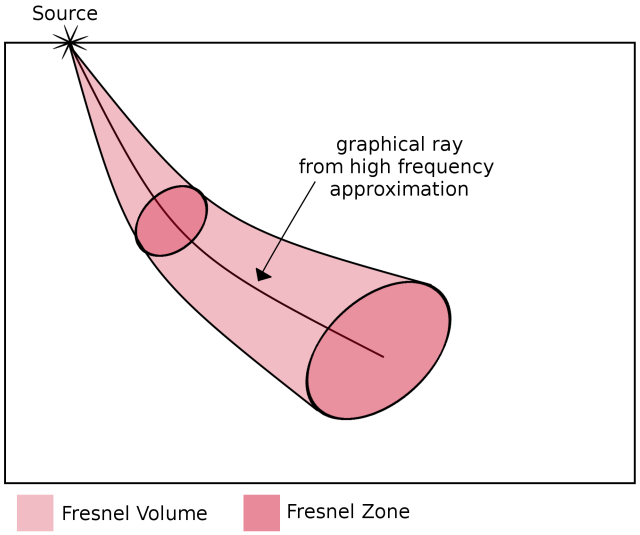

Figure 3.5: *Fresnel Volume and Fresnel Zone.*

direction of the corresponding ray is called Fresnel Zone. Sheriff (1991) defines the first Fresnel Zone as that portion of the reflector from which the reflected energy arrives at the detector within one-half wavelength of the first reflected energy. That portions of the wavefield that are reflected within the first Fresnel Zone interfere constructively and produce the reflection seismic signal in the seismogram. The wavefield located outside the first Fresnel zone is progressively attenuated with inceasing distance to the ray. In the following, the term Fresnel Zone refers to the first Fresnel Zone. For a zero-offset configuration the Fresnel Zones form annular rings around the reflection point. In the case of finite-offset configurations the Fresnel Zones form ellipses.
The size of the Fresnel Zone depends on the reflection signals dominant wavelength λ, the source-receiver-pair distance x and the reflectors depth z, respectively. In a 2D finite-offset example as illustrated in Figure 3.6 that includes a horizontal reflector in a homogenous medium, the size of the linear Fresnel Zone D is given by the following expression:

$$D = \frac{\sqrt{\lambda \cdot 2l}}{cos\varphi} \tag{3.3}$$

Here, φ is the emergence angle of the center ray given by the high frequency approximation and $2l$ is the distance between the source S, the reflection point M and the receiver R.
Sheriffs (1991) definition can be used to formulate a criterion that specifies whether an arbitrary subsurface point P in the vicinity of a ray contributes to the recorded signal and therefore lies within the Fresnel Zone, or not.
This criterion can be formulated according to simple geometric relations for travel paths by the following expression:

$$|s + r - x| \leq \frac{\lambda}{2} \tag{3.4}$$

The same criterion related to travel times and the dominant period T reads:

$$|t(S,P) + t(P,R) - t(S,R)| \leq \frac{T}{2} \tag{3.5}$$

The travel paths for rays at the edge of the Fresnel Zone are given by the rays in Figure 3.6 labeled s and r. The source-receiver offset is x. $t(S,P)$, $t(P,R)$ and $t(S,R)$ are the travel times between the source S and the subsurface point P, the subsurface point P and the receiver R and the source S and the receiver R, respectively.

Fresnel Volume Migration

Fresnel Volume migration includes the concept of Fresnel Volumes into the standard Kirchhoff Prestack Depth migration scheme in order to restrict the migration operator

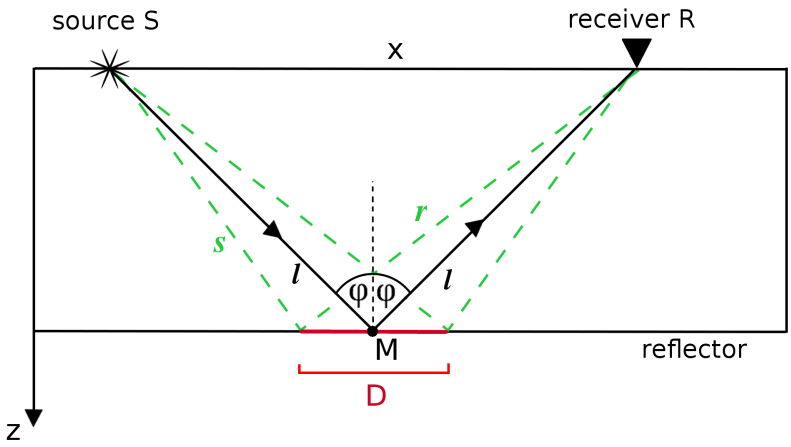

Figure 3.6: *Fresnel Zone D of a reflection event at M for a finite-offset configuration.*

to the relevant subsurface regions that effectively contribute to the reflection event. This restriction is included to the diffraction stack integral in form of an additional weight factor $w_F(\vec{x}, \vec{x'})$, the so-called Fresnel Weight. The extended diffraction stack integral reads:

$$M(\vec{x}) = U(\vec{x}, t(\vec{x})) = \int_{-\infty}^{\infty} U(\vec{x'}, t_S + t_R) \cdot W(\vec{x'}) \cdot w_F(\vec{x}, \vec{x'}) \; d\vec{x'} \tag{3.6}$$

The Fresnel Weight accounts for the Fresnel Volume that is calculated according to the travel paths through the subsurface velocity field for each recorded event. The particular travel paths are determined using a ray tracing procedure.

Ray Tracing Procedure

Based on equation 3.5 Ceverny & Soares (1992) proposed a ray tracing algorithm that subsequently determines paraxial Fresnel Volumes for all points on a particular ray. Emergence angles are directly computed from the time sections and provide the starting directions for the ray tracing procedure. The starting position is given by the receiver locations along the surface.

As the actual reflection point is a priori unknown the rays are traced into the subsurface until they reach a point called the virtual source S' (see Figure 3.7). All points located on the rays are given by the locations $\vec{x} = (x, y, z)$. The differential equation for the locations reads:

$$\frac{d\vec{x}}{dt} = v^2 \cdot \vec{p}, \tag{3.7}$$

where $\vec{p}$ is the local slowness vector that indicates the direction of the ray at each point

$\vec{x}$. The corresponding differential equation for the slowness vector reads:

$$\frac{d\vec{p}}{dt} = \frac{1}{v} \cdot \nabla v. \tag{3.8}$$

The seismic velocity $v(x, y, z)$ is given by an a priory velocity model. The initial conditions for this problem are given by the slowness at the surface $\vec{p}_0$ and the receiver positions $\vec{x}_0$. The differential equations above are solved by using the Runge-Kutta method that solves this intitial value problem for each time step in four stages:

$$\begin{aligned} k_1 &= hf(x_n, y_n) \\ k_2 &= hf\left(x_n + \frac{1}{2}h, y_n + \frac{1}{2}k_1\right) \\ k_3 &= hf\left(x_n + \frac{1}{2}h, y_n + \frac{1}{2}k_2\right) \\ k_4 &= hf\left(x_n + h, y_n + k_3\right) \\ y_{n+1} &= y_n + \frac{1}{6}k_1 + \frac{1}{3}k_2 + \frac{1}{3}k_3 + \frac{1}{6}k_4 \end{aligned} \tag{3.9}$$

n is the total number of time steps on the ray and h is the time interval. Ray tracing provides the locations of the points on the corresponding rays $\vec{x}$ and the orientation of the ray at each point given by the local slowness $\vec{p}$. Furthermore, the algorithm gives the so-called ray propagator element Π_{13} that will later contribute to calculate the Fresnel Zone for each point on the ray. The ray propagator matrix is a 4x4 matrix that contains the second spatial derivatives of the velocity field. A detailed description of the ray propagator element can be found in Cerveny (2001).

Fresnel Weight

Lüth et al. (2005) simplified the formulation of Cerveny & Soares (1992) for paraxial Fresnel Volumes by assuming smooth velocity models. In this case, the ray propagator element Π_{13} becomes the first spatial derivative of the velocity field at each grid node. They derived a formulation for an approximated Fresnel Volume that gives the Fresnel Radius r_P of the corresponding Fresnel Zone for each particular point $P(\vec{x})$ on the ray.

$$r_P = \sqrt{\frac{T_{dom}}{\frac{1}{\Pi_{13}(P)} - \frac{1}{\Pi_{13}(P) - \Pi_{13}(S')}}} \tag{3.10}$$

T_{dom} is the dominant period of the recorded seismic signals and Π_{13} are the respective ray

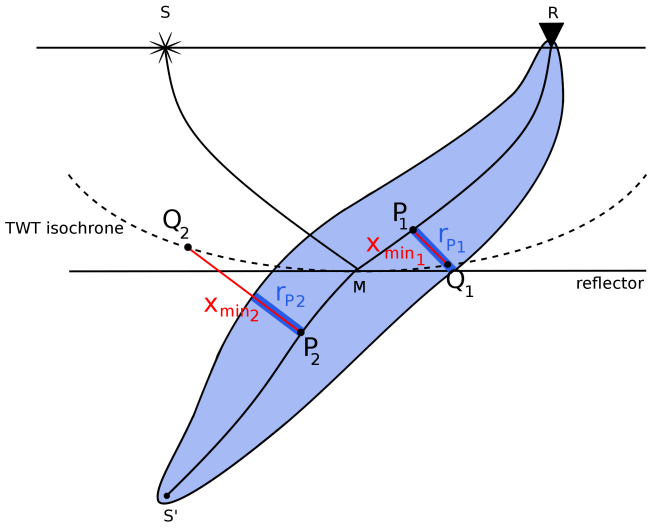

Figure 3.7: *Schematic illustration of ray tracing and Fresnel weight during Fresnel Volume migration for one recorded event. The first Fresnel Volume is represented by the blue filled area around the ray that is traced from the receiver R to the virtual source point S'. The recorded energy is assigned to the points Q along the corresponding TWT isochrone as long as the minimum distance x_{min} is smaller or equal the first Fresnel Radius r_P around point P on the ray. For Q_1 the weighting factor is 1 because $x_{min_1} < r_{P_1}$, for Q_2 the weighting factor is 0 because $x_{min_2} > r_{P_2}$.*

propagator elements. Within the next step the minimum distance x_{min} of every single image point Q in the subsurface model to the respective points P on the ray is determined. If the minimum distance x_{min} is larger than the second Fresnel Radius (here approximated by $2r_P$) around P the weighting factor is set to zero. If otherwise, the minimum distance is less the first Fresnel Radius r_P the weighting factor is set to one (see Figure 3.7). For minimum distances less the second Fresnel Radius and larger the first Fresnel Radius the weighting factor is tapered between 0 and 1 in respect of the distance to the first Fresnel Zone. The weight condition thus reads:

$$w_F(x_{min}, r_P) = \begin{cases} 1 & : \quad x_{min} \leq r_P \\ 1 - \frac{x_{min} - r_P}{r_P} & : \quad r_P < x_{min} \geq 2r_P \\ 0 & : \quad x_{min} \geq 2r_P \end{cases} \tag{3.11}$$

The Fresnel Weight $w_F(x_{min}, r_P)$ specifies if amplitudes or zeros are summed at each grid node in the subsurface volume. Consequently, amplitudes are only stacked at points located inside the Fresnel Volume of each recorded event. Applying Fresnel Volume migration significantly reduces migration noise as well as migration artefacts. Furthermore, this method is suitable for imaging steep dipping events as is shown by Gutjahr (2009).

Emergence Angle Estimation

As described above, emergence angle estimations for all recorded signals are required as starting directions for the ray tracing procedure. Nevertheless, the algorithm accounts for the slowness vector $\vec{p} = (p_x, p_z)$ whose components are directly linked to the emergence angles by Snells law:

$$sin(\varphi(x,t)) = p_x(x,t) \cdot v(x, z=0). \tag{3.12}$$

Here x denotes the receiver position at the surface, t is the two-way travel time, $\varphi(x,t)$ represents the emergence angle of each recorded event and $p_x(x,t)$ is the horizontal slowness that is also referred to as *ray parameter*. The apparent velocity $v(x, z=0)$ at the receiver stations is provided by an a priory velocity model.

Geometrical relations as presented in Figure 3.8 show that the horizontal slowness p_x represents the slope of the travel time curve $\frac{dt}{dx}$ of a recorded reflection event.

$$sin(\varphi(x,t)) = p_x(x,t) \cdot v(x, z=0) = \frac{ds}{dx} = v(x, z=0) \cdot \frac{dt}{dx} \tag{3.13}$$

The vertical slowness is defined by the following relation:

$$cos(\varphi(x,t)) = p_z(x,t) \cdot v(x, z=0) = \frac{ds}{dz} = v(x, z=0) \cdot \frac{dt}{dz} \tag{3.14}$$

After all, the horizontal slowness can be estimated directly from the common shot gathers by estimating the slope of the travel time curves $\frac{dt}{dx}$. This is done by performing a slowness analysis of neighbouring traces in the seismograms.

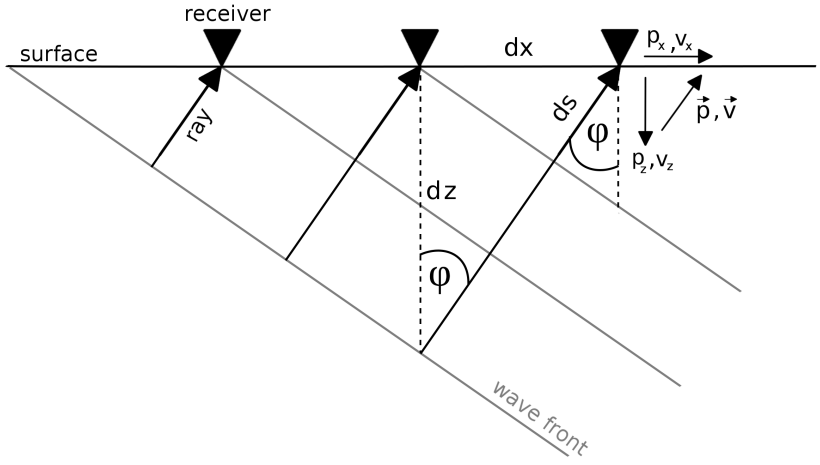

Figure 3.8: *Geometrical relations of horizontal slowness p_x and vertical slowness p_z.*

For a given range of slopes the trace to trace coherence is calculated by stacking the amplitude values over a certain amount of comparison traces within a predefined time window around the corresponding sample. The slope with the maximum coherence corresponds to the horizontal slowness. The vertical slowness $p_z(x,t)$ is computed according to the following relation using the velocity at the receiver $v(x, z = 0)$ and the horizontal slowness $p_x(x,t)$:

$$\mid \vec{p}(x,t) \mid = \sqrt{p_x(x,t)^2 + p_z(x,t)^2} = \frac{1}{v(x, z = 0)} \tag{3.15}$$

$$p_z(x,t) = \sqrt{\frac{1}{v(x, z = 0)^2} - p_x(x,t)^2} \tag{3.16}$$

3.3 Reflection Image Spectroscopy

In general, seismic reflection data analyses aim to expose geological heterogeneities in the subsurface. Heterogeneities involve changes of the materials composition or elastic properties as well as temperature and stress distribution, respectively. The ability to image those features depends on the scale of the heterogeneities in relation to the wavelengths of the emitted wavefield. Thereby, the wavelength must be in the order of the heterogeneities size to obtain a suitable image. Usually seismic reflection data are acquired in a more or less wide frequency range of 1 to 100 Hz depending on the source types used. Vibroseis sweeps progressively produce frequencies between 10 and 80 Hz. For crustal velocities of approximately 5 km/s respective wavelenghts range between 60 m and 500 m.
Seismic images of data that contain the full or at least a broad frequency range will effect the loss of information on small-scale structures that are mostly superimposed by large-scale structures imaged by the lower frequency wavefield components. Furthermore, the image of a reflector is strongly affected by the amount of frequency dependent scattering from above the reflector (Yoon, 2005). These scattering effects cause amplitude loss and phase fluctuations of certain frequency components according to the scatterers size. On that account Yoon (2005) applied several bandpass filter to the full-frequency range data in order to extract data sets of discrete narrow-frequency bands. Migration of the separate data sets yield seismic images of large-scale structures from the low-frequency range and

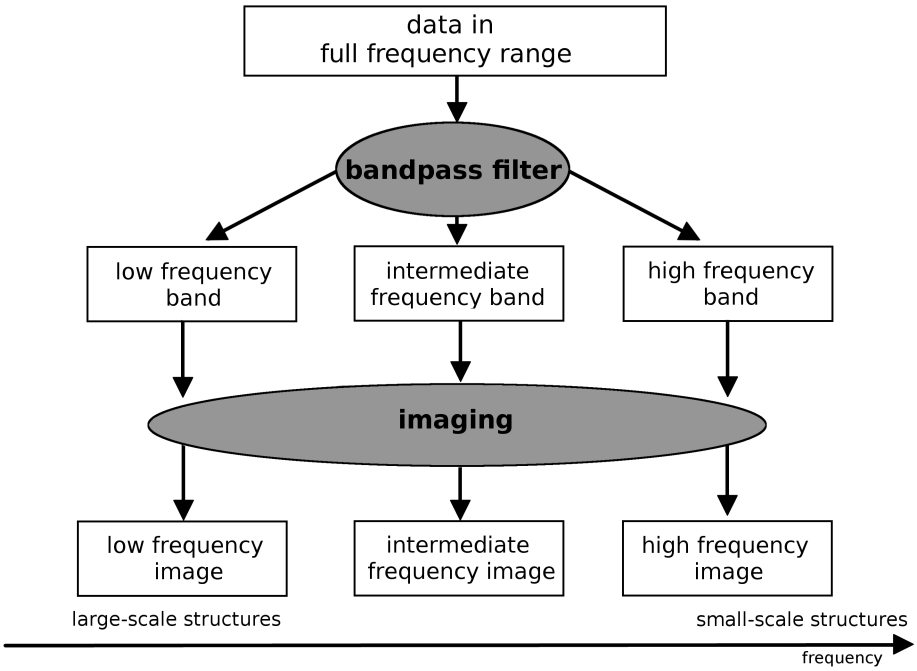

Figure 3.9: *Reflection image spectroscopy processing scheme.*

small-scale structures from the high-frequency range data. Additionally deep reflector images are enhanced in those frequency ranges that are not effected by scattering.
Yoon (2005) called this approach Reflection Image Spectroscopy. The processing sequence of Reflection Image Spectroscopy is schematically shown in Figure 3.9. Yoon et al. (2009) sucessfully applied this method to seismic reflection data sets from across the Central Andes and Southern Andes in South America and imaged additional structural details of the Andean subduction zone.
In the frame of this work Reflection Image Spectroscopy will be applied to the SJ-6 data set in order to obtain additional information on large as well as the small scale crustal features across the San Andreas fault system in Central California. An overview on the implementation of Reflection Image Spectroscopy is given in section 4.4.3 of chapter 4. The results are presented in chapter 5.

4 The SJ-6 Industry Seismic Reflection Profile

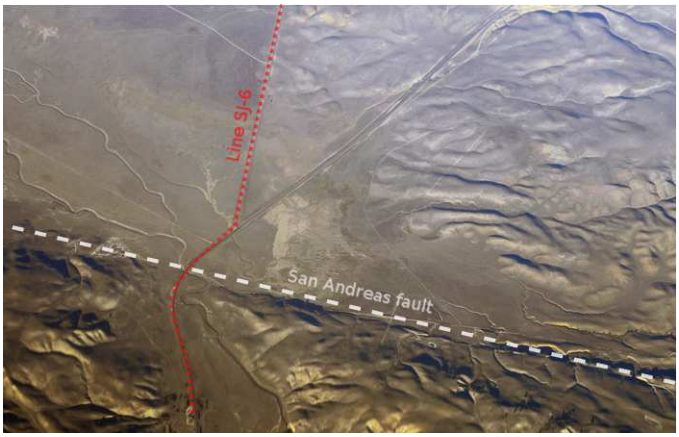

Figure 4.1: *Air photograph of the San Andreas fault (dashed white line) near Cholame crossing the location of the SJ-6 acquisition line (red line) (with kind permission of Michael J. Rymer).*

The industry seismic reflection data set SJ-6 (San Joaquin Valley - line 6) was acquired in 1981 by Western Geophysical. The survey was designed for economical purposes in order to explore oil reservoirs especially in the anticline belt east to the San Andreas fault that houses major oil fields, e.g. the Coalinga, Kettleman Hills North Dome and the Lost Hills oil fields, respectively. In 1982 the USGS (United States Geological Survey) performed a seismic refraction survey along approximately the same profile line for deep crustal studies of the California Coast Ranges and the adjacent Great Valley. In order to complement the refraction data the USGS purchased the SJ-6 industry reflection data in 1983. Numerous scientific groups analysed parts of both data sets in order to obtain velocity and structural information on the subsurface along line SJ-6. Most of the results were published in the Open-File report 87-73 in 1987 (Mooney and Walter, 1987). The coincident reflection and refraction data from line SJ-6 have been included into several studies that investigate the crustal structure of Central California, e.g. Bloch et al. (1993), Fuis et al. (1990) and Wentworth et al. (1987), to name but a few. In the scope of this work the complete

reflection data set is reprocessed using advanced imaging techniques in order to produce depth images of improved quality compared to existing results. This chapter aims to give an overview on the seismic reflection data set SJ-6. The location of the profile line as well as the experimental setup is presented in the following section 4.1. Section 4.2 gives an overview on selected investigation results of previous studies on the reflection and refraction data sets along line SJ-6.

In the current study, the data set will be separated into two segments according to the predominating orientation of the survey line. Both data sets will be processed separately. But prior to the actual imaging process several preprocessing steps have to be performed to first prepare the original field data for imaging and second to obtain a suitable velocity model. Section 4.3 firstly introduces the local coordinate system, the individual line segments and the model set up followed by a description of the velocity model and the actual data preprocessing.

Finally, section 4.4 shows how the three migration approaches are implemented and explains the stacking and visualization procedure.

4.1 Location and Experimental Setup

The complete SJ-6 receiver line extends over a distance of 180 km from the Pacific Coast east towards the foothills of the Sierra Nevada. It crosses the major geologic formations of Central California that have previously been introduced in chapter 2.

Figure 4.2 illustrates the course of line SJ-6 across the California Coast Ranges and

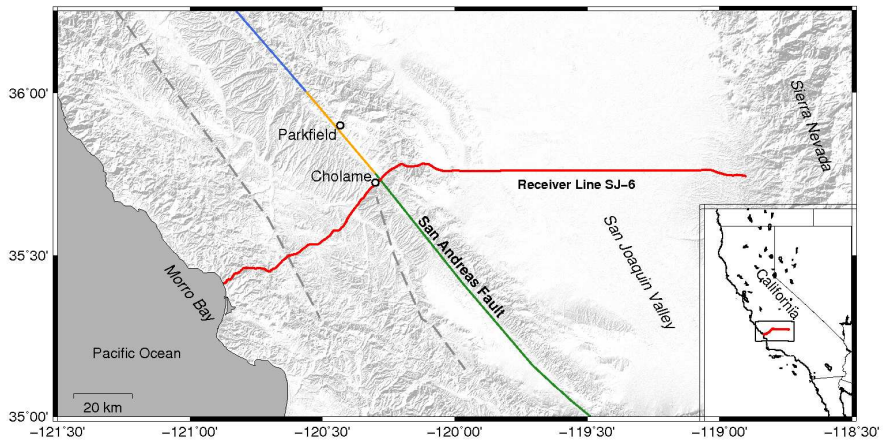

Figure 4.2: *Location of line SJ-6 (red line) in South Central California. Colors along the San Andreas fault represent the creeping segement (blue), the transitional segment (orange) and the currently locked segment (green), respectively.*

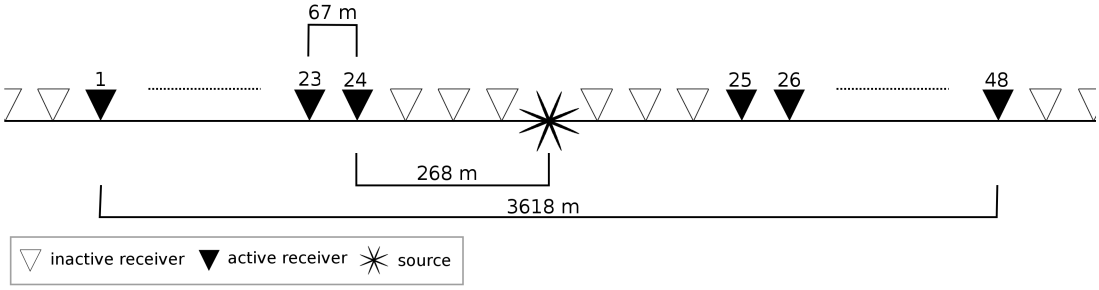

Figure 4.3: *Split-spread acquisition geometry along the SJ-6 receiver line; Maximum offset is 1809 m.*

the San Joaquin Valley in South Central California. Measurements started at the Pacific Coast near Morro Bay and proceeded northeast towards Cholame following Highway 41. On its way the acquisition line crosses prominent fault systems of the California Coast Ranges such as the Nacimiento fault zone, the Rinconada fault zone, the San Juan fault zone and the San Andreas fault zone, respectively. Unfortunately the receiver line is highly crooked along the southwestern part of the profile as the acquisition has been partly performed along winding roads. Several shot points have been skipped due to houses, rivers, drilling wells and other obstacles.

The acquisition line intersects the San Andreas fault surface trace near Cholame. The line then turns east and transverses the Kettleman Hills and the San Joaquin Valley until it was completed at the foothills of the Sierra Nevada. The easternmost part of the profile across the San Joaquin Valley follows a more or less straight line.

The acquisition was performed using the classical roll-along technique with equidistant source spacing and receiver spacing. A 48 channel split-spread geometry with a maximum offset of 1.8 km and a receiver spacing of 67 m was used (see Figure 4.3). The initial source receiver offset amounted to 268 m. The recording spread changes to an end-on spread geometry across the San Joaquin Valley for a length of 45 km.

The wavefield was generated by Vibroseis sources (Trademark, Conoco Inc.) using a 20 second upsweep in a frequency range between 10 and 52 Hz. The shot point intervall is identical to the receiver spacing intervall of 67 m. Receiver and shot point locations along the line are identical. Thus, only one set of coordinates have to be considered during the processing. The recording length of the original single shot sections is 26 seconds. Single component sensors recorded the vertical component of the incident wavefield.

4.2 Previous studies along line SJ-6

Since 1983 when the USGS purchased the SJ-6 reflection data set it was partly analysed by several scientific groups in the frame of a workshop of the *Commission on Controlled Source Seismology* held in 1985. The results have been published in the Open-File Report 87-73 in 1987. Due to the large data volume most groups regarded only particular parts of the profile line. The results fairly differ as the groups used different methods and assumptions, especially on the velocity field. Mooney and Walter (1987) gave an overview on the most important results of the above mentioned report. The following section shortly resumes the descriptions of Mooney and Walter (1987) and thereby concentrates on the results of Trehu and Wheeler (1987) for the western portion of profile SJ-6 and Walter et al. (1987) for the eastern portion, respectively. Both groups analysed the combined reflection and refraction data sets.
The studies in the Open-File Report are all restricted to certain portions of the refraction data set. Only few studies are completed by the reflection data. The resulting velocity models that have been derived from the refraction data are in closer agreement east to the San Andreas fault than west to the fault.

Line SJ-6 southwest to the San Andreas fault
All determined velocity models include abrupt changes in the shallow velocity structure at the San Andreas fault and the Rinconada fault. Between the faults, the sedimentary layer sequences in the shallow crust thicken towards east. Beneath the sedimentary cover the velocities in the Salinian Block are significantly higher compared to the adjacent blocks west of the Rinconada fault and east to the San Andreas fault, respectively.
Trehu and Wheeler (1987) modeled three low-velocity zones within the lower crust. Figure 4.4 a) illustrates velocity isolines of their final velocity model in combination with a ray diagram for a shot from the southwestern end of line SJ-6. The first low-velocity zone (LVZ1) is located at depth between 12 km and 22 km in the westernmost part of the Salinian Block. It shows a prominent wedge shaped structure that plunges towards east. The top of this low velocity zone coincides with a bunch of northeast dipping reflections (see figure 4.4 b)) from the SJ-6 reflection data. Trehu and Wheeler (1987) interpret these coinciding structures as subducted and unmetamorphed sediments from a today inactive trench approx. 150 km offshore. The second low velocity zone (LVZ2 in Figure 4.4 a)) is localized beneath the San Andreas fault surface trace down to midcrustal depths. To the east of the Salinian Block the reflection data quality is poor and no major reflections could be observed from within the San Andreas fault zone. Combining their results from

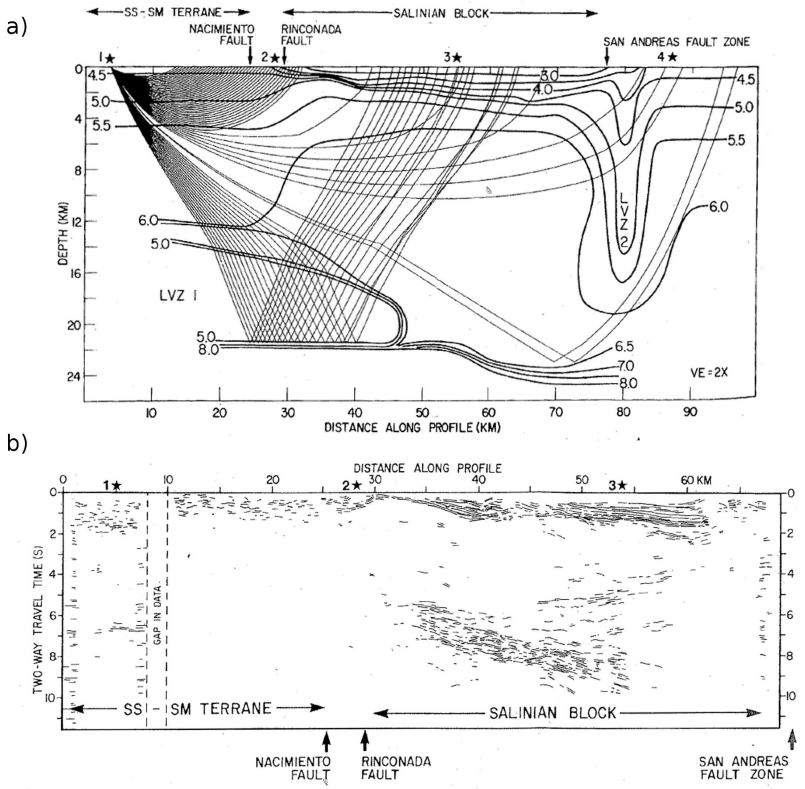

Figure 4.4: *a) Velocity isolines from Trehu and Wheeler (1987) for the western SJ-6 line segment together with a ray diagram for the westernmost shot point SP1 of the refraction survey. b) Line drawing of the unmigrated reflection data along the same line segment.*

both, the reflection and the refraction data sets, Trehu and Wheeler (1987) suggest the existence of fault gouge material within the fault zone. Furthermore, they present a third low velocity zone (not shown in Figure 4.4 a)) within the Salinian Block west of the San Andreas fault zone that coincides with west dipping reflections which are interpreted as the base of the Salinian Batholith that is suggested to be thrusted over lower velocity Franciscan assemblage rocks.

Line SJ-6 east to the San Andreas fault

The velocity models show westward thickening sedimentary layer sequences across the San Joaquin Valley. Beneath the Kettleman Hills higher velocity sedimentary strata are elevated by an eastward thinning wedge of intermediate velocity. Nearly each group derived a continuous basement but the top boundary of the basement is located at different depths. The results do not provide velocity information on the basement itself. Figure 4.5 shows the results of Walter et al. (1987) and Bloch et al. (1993) where a) illustrates the unmigrated reflection section and b) the interpreted depth section including the velocity information from the refraction data ananlyses. Figure 4.5 c) shows the migration result

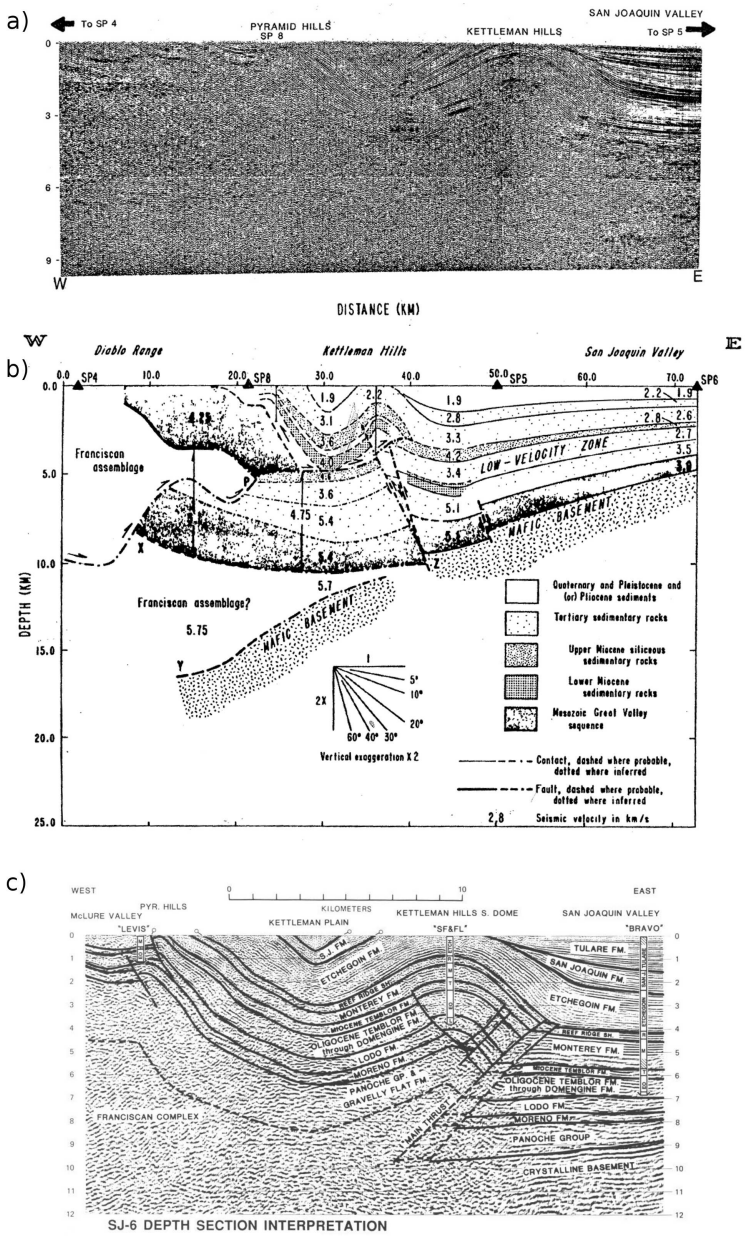

Figure 4.5: *a) Portion of the SJ-6 reflection data along the eastern SJ-6 line segment. b) Interpretation of combined refraction/reflection data from Walter et al. (1987). c) Interpretation of prestack migrated SJ-6 reflection data from Bloch et al. (1993)*

of Bloch et al. (1993) who analysed the eastern portion the SJ-6 reflection data set. The reflection data show a prominent fold in the centre of Figure 4.5 a). Structures at the anticlinal arch are interpreted as northeast-dipping reverse faults and southwest-dipping thrust faults. Beneath the San Joaquin Valley west dipping horizons define the sedimentary basin west of the prominent fold. The base of these horizons steepens its dip beneath the Kettlaman Hills and reaches depths of about 15 km farther to the west. This interpretation is supported by the refraction data that reveal a deeper mafic basement

west to the Kettleman Hills compared to the east according to a velocity rise greater to 6 km/s. Furthermore, the final velocity model implicates a low velocity zone east of the Kettleman Hills at depths of approx. 5 km. Wentworth et al. (1984) interpret this feature as a repetition of Great Valley sequence material that originated west to the Kettleman Hills. It was thrusted towards east due to compression during the Pliocene and formed the above mentioned fold. It is furthermore suggested that rocks similar to Franciscan rocks form a wedge that underthrusts Great Valley sequence formations beneath the Kettleman Hills as illustrated in Figure 4.5 b). Bloch et al. (1993) reprocessed the fraction of the eastern SJ-6 data using Prestack Migration techniques in order to image the upper crust beneath the Kettleman Hills. Several sedimentary layer sequences as well as thrust faults have been identified (Figure 4.5 c)). Using this data, Bloch et al. (1993) derived a three-stage growth history for the Kettleman Hills. The results provides no information on the lower crustal structures.

4.3 Preprocessing

4.3.1 Coordinate system and subsurface volume set up

Line SJ-6 is an extremely long profile that crosses several faults and geomorphic units and comprises a large amount of seismic data. The profile line is not a straight line. Instead, it is crooked along several parts of the profile, especially in the western Coast Ranges where the data have partly been acquired along windy roads. After crossing the San Andreas fault towards northeast the profile line changes its orientation from southwest-northeast to west-east, respectively. The receiver line coordinates are available in SEG-P1 format (see Geophysics, vol48/no4,1983) in plane coordinates of the California Coordinate system (CCS83) Zone 5. The coordinates are firstly converted into SI units (from feet in m) and secondly transformed into a predefined local coordinate system that is oriented perpendicular to the strike of the San Andreas fault surface trace. The origin of the coordinate system is at 120.9° longitude and 35.5° latitude which is marked by the red point in Figure 4.6.

In order to account for the prominent kink of the receiver line and the partly crooked line geometry the migration approaches are implemented in 3D and the SJ-6 receiver line is divided into two segments. For that, two subsurface volumes are predefined, each in line with the respective receiver line segment. Defining two subvolumes instead of one large

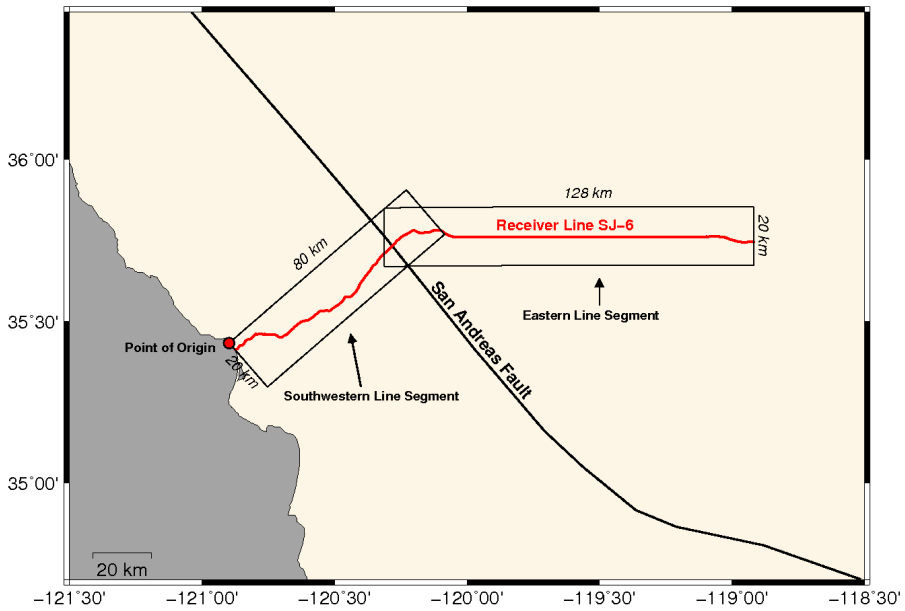

Figure 4.6: *Subdivision into two line segments and the dimensions of the corresponding two subsurface models.*

volume reduces the computation time and the amount of occupied disk space significantly. Figure 4.6 illustrates the two individual receiver line segments and the correspnding subvolumes that are individually processed in the following. The first receiver line segment includes the southwestern section of the acquisition line that crosses the western Coast Ranges and the San Andreas fault. The second receiver line segment includes the eastern section of line SJ-6 that crosses the eastern Coast Ranges and the San Joaquin Valley, respectively. The horizontal dimensions of the subsurface volume beneath the southwestern segment are 80 km in southwest-northeast direction and 20 km in northwest-southeast direction. Those of the second segment are 128 km in east-west direction and 20 km in north-south direction. The vertical extent is 45 km for both subvolumes in order to image the lower crust and if possible parts of the upper mantle.
Migration is performed separately in both subsurface volumes under consideration of the associated shot point locations. The following section introduces the velocity model that provides the a priori velocity information which are the basis for travel time calculation and the ray tracing procedure that is required for Fresnel Volume migration.

4.3.2 Velocity model compilation

In previous studies seismic velocities have been analysed and published in the Open-File Report 87-73 in 1987 on the basis of the SJ-6 refraction data. However, the resulting models are to some degree inconsistent as the acquisition conditions have not been ideal due to large shot point spacings and, compared to these days, limited computing facilities. Additionally, velocity information on the lower crust are not well resolved by these data. In the scope of this study, two present-day three-dimensional tomographic compressional velocity models are used to provide velocity information for the entire crust beneath the SJ-6 investigation site. Zhang and Thurber (2003) developed a double-difference tomography method (tomoDD) in order to obtain improved velocity models by using absolute and relative arrival times of earthquake data and active source experiments.
Thurber et al. (2006) used this method to derive a regional velocity model for the Parkfield region using local earthquake data from densely spaced receiver stations as well as active seismic data sets. They improved the velocity models resolution by including data recorded from the prominent 2003 San Simeon and the 2004 Parkfield earthquakes, respectively. The local Parkfield velocity model covers a region 130 km in northeast-southwest direction and 120 km northwest-southeast direction aligned with the strike of San Andreas surface trace. It comprises the southwestern SJ-6 line segment and parts of the eastern line segment. The locations of the respective grid nodes of the local Parkfield velocity model are shown in Figure 4.7 by black diamants. Gridspacing varies between 25 km and

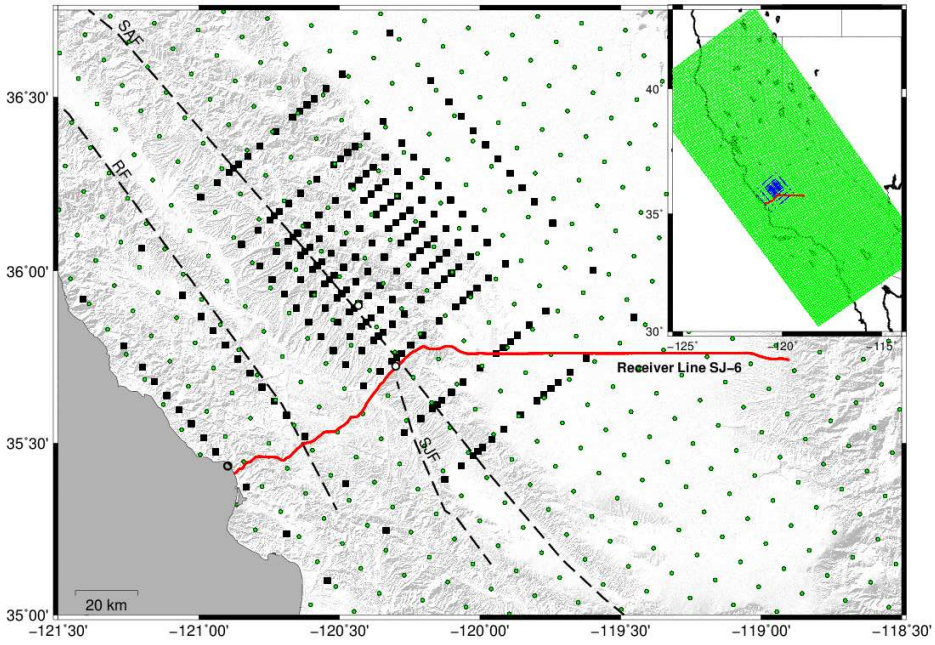

Figure 4.7: *Velocity model grid point locations. Black diamants are grid point locations of the local Parkfield velocity model from Thurber et al. (2006); Green dots represent grid point locations of the statewide California model from Lin et al. (2010) (total extent of the model is presented in the small box in the right top corner); red line is the SJ-6 receiver line.*

2 km in perpendicular to the strike of the San Andreas fault, 20 km and 6 km in along strike direction and 8 km to 2 km in depth, respectively, reaching a maximum depth of 26 km.

Unfortunately, the Parkfield velocity model of Thurber provides no velocity information on the subsurface beneath the eastern segment of line SJ-6 and for depths greater than 26 km. To provide the rest of the subvolumes with 3D velocity information the statewide California velocity model from Lin et al. (2010) is used. They calculated velocity models across California using the tomoDD algorithm from Zhang and Thurber (2003). Horizontal gridspacing amount to 10 km. The respective grid nodes are illustrated in Figure 4.7 by green dots. The vertical extend of the California statewide velocity model is 45 km.

Both compressional wavespeed models are interpolated to a regular gridspacing of 1600 m in each direction. Afterwards the models are combined by adding the statewide model to the edges of the Parkfield model. Both models are weighted at the edges along a certain amount of grid points. Finally, the combined model is interpolated to a regular grid spacing of 200 m in each direction. Slices through the final velocity model are shown in Figure 4.8 for the southwestern SJ-6 line segment and the eastern segment, respectively.

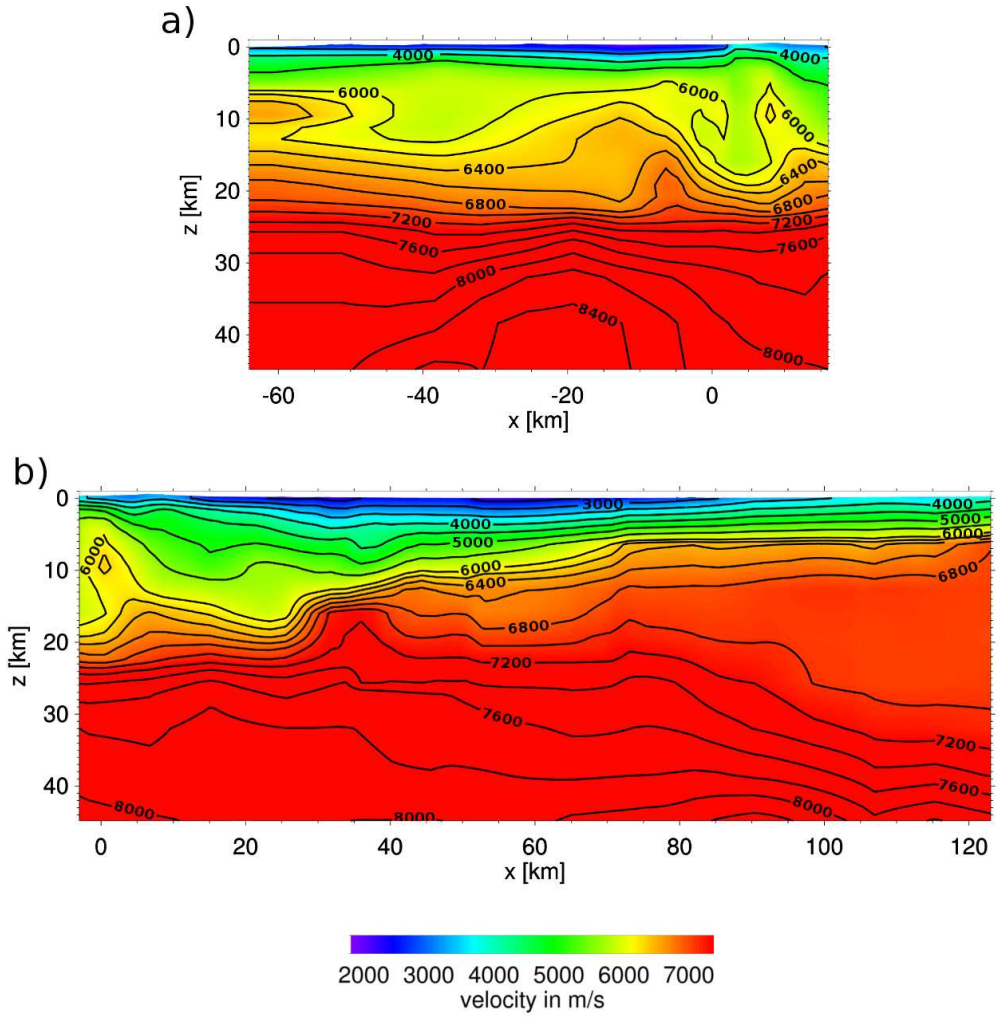

Figure 4.8: *Cross-sections at $y = 10$ km from the separate subsurface velocity models along a) the southwestern and b) the eastern SJ-6 line segments, respectively.*

It shows a significant low-velocity zone across the San Andreas fault zone ($x = 0$ km) down to approximately 20 km depth.

Velocities are higher west of the San Andreas fault zone compared to those east of the fault zone above depths of 17 km. A second low velocity zone appears approximately 40 km west to the San Andreas fault at depths between 8 km and 13 km. The velocity structure west of the San Andreas fault and within the San Andreas fault zone derived by Thurber et al. (2006) is similar to that modelled by Trehu and Wheeler (1987) (see section 4.2). Moreover, the velocity structure east to the San Andreas fault shows the same large scale features as have been observed from the SJ-6 refraction data analyses (Mooney and Walter, 1987). Seismic velocities are low east to the San Andreas fault and rise towards east with decreasing depths.

4.3.3 Diffraction curve estimation

The diffraction curves are estimated by calculating the two-way travel times for all source-receiver location pairs using the a priori velocity model presented in the previous section. As the velocity structure is rather complex travel time calculation is performed numerically using the finite difference algorithm proposed by Podvin & Lecomte (1991). This algorithm calculates first arrival travel times by numerically solving the eikonal equation. Thereby Huygens' principle is successively applied to compute local travel times at every grid node in the subsurface model according to each receiver and source location that act as starting points. First arrival travel times at the grid nodes are then obtained by picking the first arrival from all set of Huygens' secondary sources sourrounding the correspondig grid point. The algorithm allows for different propagation modes, i.e. transmitted and diffracted body waves as well as head waves. The algorithm is robust and fast and it can easily be implemented on parallel computer systems. In order to obtain the diffraction curve for a source-receiver pair location and therefor the two-way travel time for a particular subsurface point, the calculated travel time sections of corresponding source and receiver locations are summed. Figure 4.9 shows the travel time isolines (in seconds) calculated for one source-receiver pair infront of a cross-section of the P-wave velocity

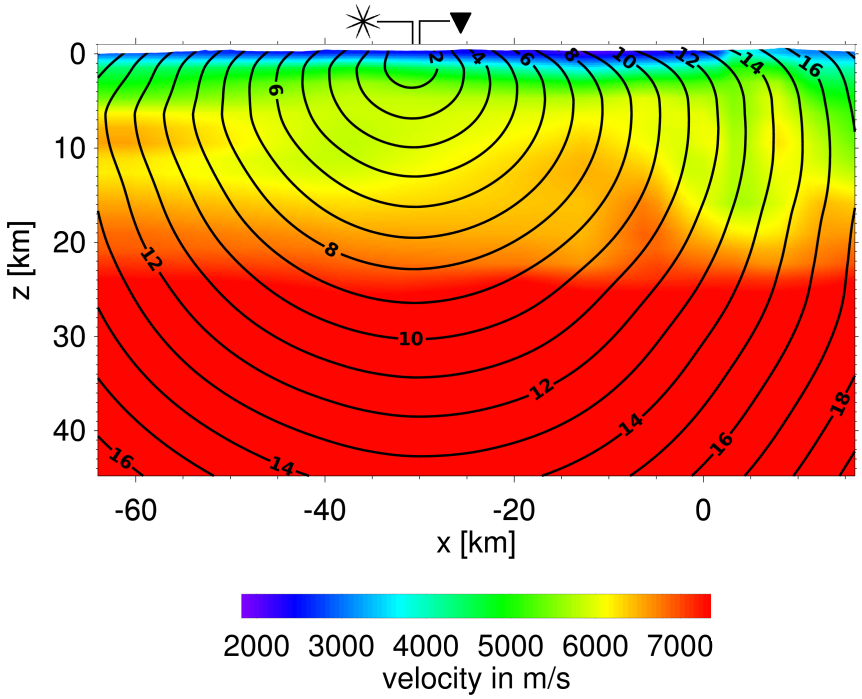

Figure 4.9: *Two-way travel time isochrones for a source-receiver pair located at $x_{src} = -31.5$ km and $x_{rcv} = -30$ km infront of the $x - z$-cross section of the corresponding P-wave velocity model along the southwestern SJ-6 line segment.*

model along the southwestern SJ-6 line segment.
In total 3388 travel time tables are calculated for all receiver positions and stored. The source coordinates are identical to the receiver coordinates, thus only one set of travel time tables need to be calculated. In order to reduce the amount of occupied disc space, grid spacing is enlarged from 200 m to 2000 m in the direction perpendicular to the SJ-6 receiver line.

4.3.4 Data Preprocessing

The original field data have been obtained from the USGS (Gary Fuis). These data are so far not suitable for the imaging process as the single shot files are poorly sorted and the data itself are unbalanced and noisy. The data preprocessing contains three main steps:

1. Data inspection and sorting
2. Crosscorrelation
3. Frequency filtering and amplitude balancing

The original field data need to be inspected for their data content and quality and sorted for their receiver and shot locations along the receiver line. Crosscorrelation is required to eliminate the source signal from the data as will be discussed in the following. In general, the aim of data preprocessing is to enhance reflection signals all over the seismic section and simultaneously suppress other recorded coherent signals like ground roll, direct and refracted waves and incoherent noise. Precise preprocessing prior to migration enhances seismic reflectors in the final depth images and reduces migration noise significantly.

Data inspection and sorting

The original field data are stored in SEGY-format. At first the data are examined and converted to Seismic Unix compatible SU-format. The given files are separated into single common shot records. Afterwards the data are sorted, checked for bad shots and renamed taking into account the SJ-6 field observer notes and oberserver notes made by Mark R. Goldman from the USGS, respectively. Available receiver coordinates are stored in SEG-P1 format (see Geophysics, vol48/no4,1983) in plane coordinates of the California Coordinate System (CCS83) Zone 5. The receiver coordinates are rotated to the predefined local coordinate system that is oriented perpendicular to the predominating strike of the San Andreas fault surface trace. Subsequently the receiver and shot-point coordinates are assigned to the corresponding trace headers. Afterwards empty and noisy traces are identified and killed.

The remaining traces provide the *fold* for all receiver locations. Here the fold is defined by the number of traces having identical receiver coordinates. The respective folds along the southwestern and the eastern SJ-6 line segments are shown in Figure 4.10. It can be expected that the quality of the migration results will correlate with the respective fold numbers that deviate extremely along several parts of the profile line. The inconsistency of fold numbers results from skipped shot points along the line due to inaccessible regions.

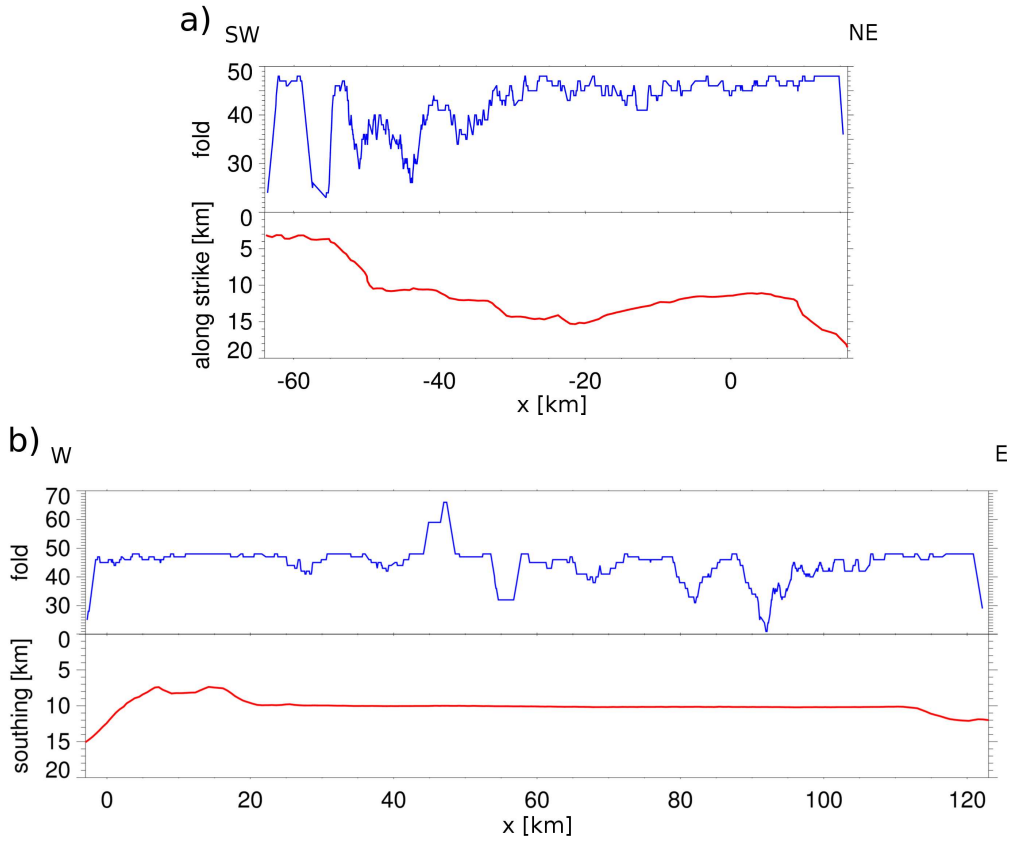

Figure 4.10: *Fold (blue curves on top) along a) the southwestern SJ-6 line segment and b) the eastern line segment. Red curves are receiver line positions along the individual line segments.*

High folds better account for changing recording conditions and different noise levels during acquisition and thus result in better signal-to-noise ratios.

Crosscorrelation

The active seismic energy along line SJ-6 was generated by non-explosive Vibroseis sources that produced a 20 second long upsweep containing frequencies ranging from 10 Hz to 52 Hz. The sweep signal superimposes the earths reflection response by streching the wave train by 20 seconds. The single reflection events are obtained by removing the sweep signal and therefore compressing the data. This is done by crosscorrelating the original field data with the corresponding sweep signal. The following explanation of the correlation process is taken from Yilmaz (1987). In the following paragraph the original field data are referred to as *vibrograms*. The vibrograms $v(t)$ have been recorded over a period of 26 seconds. They contain superpositions of the reflection response and the sweep signal which is nothing else but a convolution of the sweep $sw(t)$ with the earth response $e(t)$ and the response of the recording system $w(t)$.

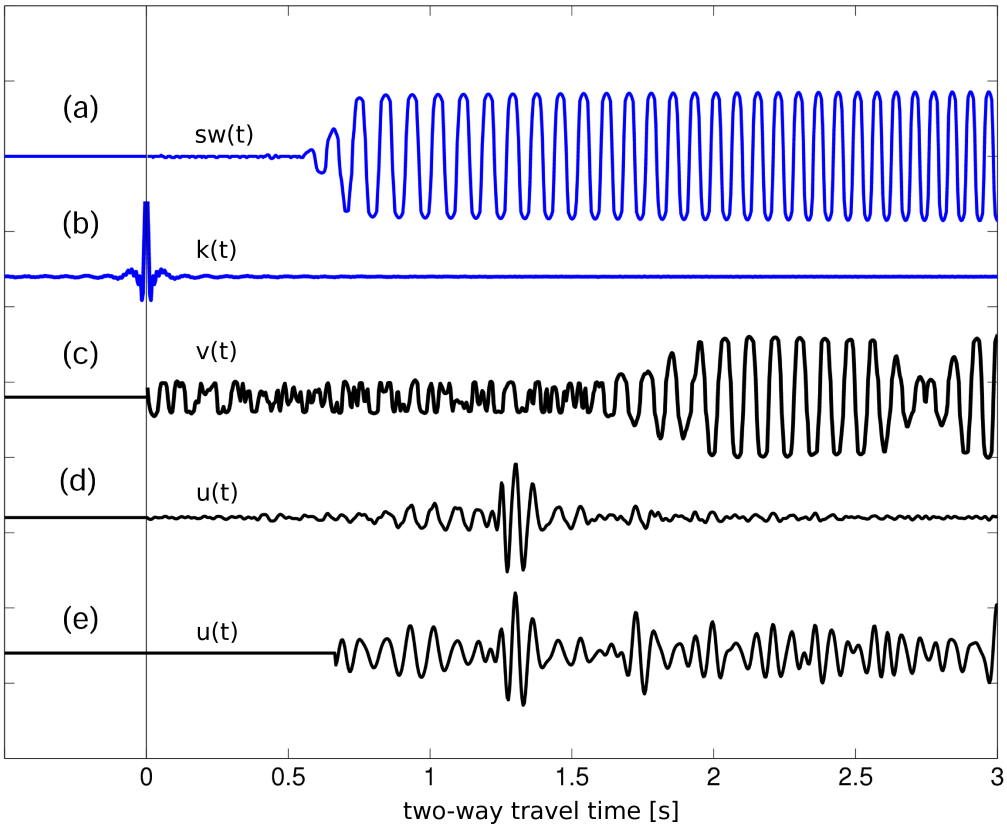

Figure 4.11: *Overview on vibroseis correlation: a) upsweep signal $sw(t)$; b) autocorrelation function of the sweep signal $k(t)$; c) reflection signal $v(t)$ before crosscorrelation; d) reflection response $u(t)$ after crosscorrelation; e) reflection response $u(t)$ corrected for geometrical spreading.*

$$v(t) = sw(t) * e(t) * w(t) \tag{4.1}$$

Hence, the sweep signal has to be removed in order to obtain single reflection events in the seismogram $u(t)$. Therefor the sweep signal $sw(t)$ is crosscorrelated with the vibrogram $v(t)$.

$$u(t) = v(t) * sw(-t) \tag{4.2}$$

In frequency domain this operation is simply a multiplication of the vibrogram $V(\omega)$ with the complex conjugate of the sweep $SW^*(\omega)$.

$$U(\omega) = V(\omega) \cdot SW^*(\omega) \tag{4.3}$$

$V(\omega)$ can now be substituted by equation 4.1 which is a multiplication in frequency domain as well.

$$U(\omega) = SW(\omega) \cdot E(\omega) \cdot SW^*(\omega) \cdot W(\omega) \tag{4.4}$$

Considering the amplitudes and phases one can write:

$$U(\omega) = A_{SW}(\omega) \cdot A_E(\omega) \cdot A_W(\omega) \cdot A_{SW}(\omega) \cdot e^{i(\phi_{SW}+\phi_E+\phi_W-\phi_{SW})} \tag{4.5}$$

$$U(\omega) = A_{SW}^2 \cdot A_E(\omega) \cdot A_W(\omega) \cdot e^{i(\phi_E+\phi_W)} \tag{4.6}$$

Applying the inverse Fourier transform yields the crosscorrelogram $u(t)$ in the time domain. The powerspectrum of the sweepsignal A_{SW}^2 is its autocorrelation $k(t)$ in the time domain, called klauder wavelet. The crosscorrelogram $u(t)$ writes as follows

$$u(t) = k(t) * w(t) * e(t) \tag{4.7}$$

Thus, the application of crosscorrelation collapses the reflections into wavelets and the seismogram is compressed to 6 seconds two-way travel time. Figure 4.11 illustrates how crosscorrelation collapses reflection signals into wavelets. The top blue curves represent the sweep signal $s(t)$ and its autocorrelation function $k(t)$. The sweep signal stretches the reflection response of the original field data $v(t)$ c) and makes it therefor not suitable for imaging. The bottom curves show the crosscorrelogram $u(t)$ without amplitude scaling d) and with amplitude scaling e).

The 6 seconds two-way travel time records are much to short for our purposes, that is, imaging the lower crust and the deep San Andreas fault. For this reason 20 seconds of zeros were addedto the original field data before crosscorrelating it with the corresponding sweep signal. The results are correlated records of 26 seconds two-way travel time. During this procedure high frequencies are gradually lost with increasing time yielding a bandwith of 10 Hz to approximately 20 Hz at the end of the correlated records. This bandwidth is considered sufficient as late reflections in the original field data predominantly contain frequencies between 10 and 20 Hz.

Frequency filtering and amplitude balancing

The correlated single shot records are further bandpassfiltered within a frequency range between 10 Hz and 25 Hz. The recorded signals are gradually attenuated with increasing offset and travel time due to geometrical spreading and other causes of attenuation. These effects are corrected by applying automatic gain control (AGC) to all traces. A time window of 500 ms is used to calculate the scaling factor for each particular sample. Therefor the maximum value of the corresponding trace is divided by the mean value within the time window and multiplied with the corresponding amplitude value. Afterwards trace balancing is applied to all common shot gathers by dividing each time sample by the maximum of the corresponding AGC-corrected trace within each common shot gather. Finally, an offset mute was applied to the data.

Figure 4.12 shows a seismogram sample of the SJ-6 data. Further, the frequency-time dependence for one single trace of the seismogram sample is illustrated at the right hand side of the Figure. Figure 4.12 a) and b) show the vibrogram of one single shot gather. No clear reflection signals can be recognized as the wavetrains are stretched by the overlapping sweep signal. The sweep signal can clearly be seen in the time-frequency plot in Figure 4.12 c) as a linear slope. Figure 4.12 d) and e) is the same data sample but recorrelated with the sweep signal. Direct arrivals as well as prominent horizontal reflections can clearly be recognized for early two-way travel times. However, late arrivals are hard to discover as the amplitudes are unbalanced. The gradual loss of frequencies with increasing time is clearly shown in the time-frequency plot in Figure 4.12 f) and becomes more clear in Figure 4.12 i) showing the same for the preprocessed data. The final preprocessed single shot section of the same sample is shown in Figure 4.12 g) and h), respectively.

Figure 4.12: *Single shot gather sample. Left hand side: full data range, middle: first* 6 *seconds data, right hand side: frequency-time dependency. a-c) uncorrelated data, d-f) correlated data and g-j) full preprocessed data.*

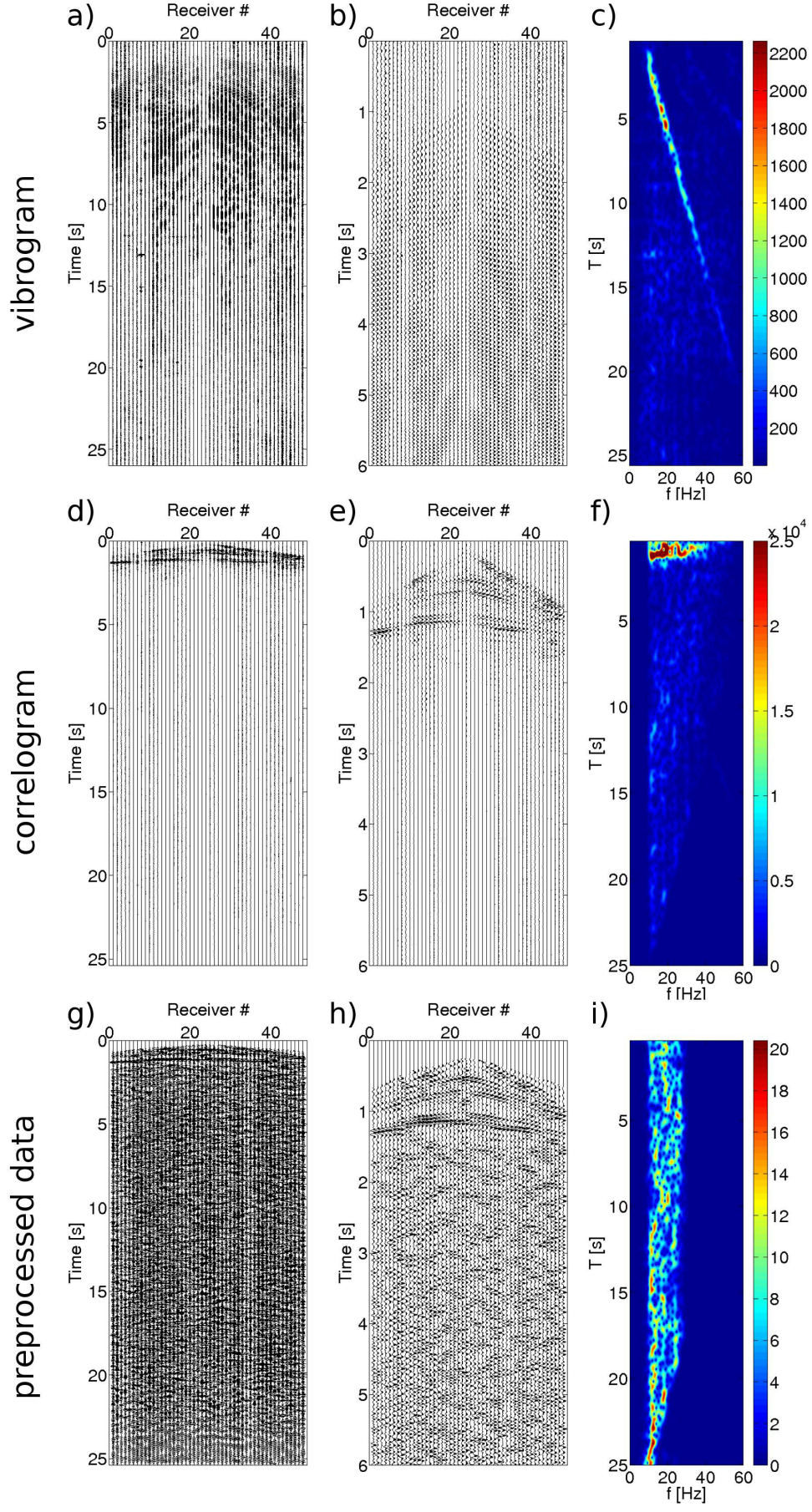
vibrogram
correlogram
preprocessed data
a)
b)
c)
d)
e)
f)
g)
h)
i)
Receiver #
Time [s]
T [s]
f [Hz]
x 10^4

4.4 Seismic imaging

In the following, Kirchhoff Prestack Depth migration, Fresnel Volume migration and Reflection Image Spectroscopy will successively be applied to the SJ-6 data set. The following sections describe the respective migration and stacking procedures that are used to optimize the image quality.

Kirchhoff Prestack Depth migration, Fresnel Volume migration and Reflection Image Spectroscopy follow in general the same workflow which is illustrated in Figure 4.13. All preprocessed single shot sections are migrated separately. In order to account for the true shot and receiver positions during the migration process, the migration scheme is implemented in 3D as proposed by Buske et al. (1999). The total amount of single shot gathers is indeed large. As a consequence computational time and the amount of data volume is significantly high. In order to reduce the computational time, the migration processes are all performed on a parallel computer cluster system providing 184 nodes.

All migrated single shot sections are then stacked yielding a final migrated 3D section that holds the reflectivity information along the respective segment of line SJ-6. The term *reflectivity* in this case does not allow any conclusion about the actual reflection coefficient. It is rather used in the term of apparent reflection response as we aim to obtain qualitative information on the subsurface structures.

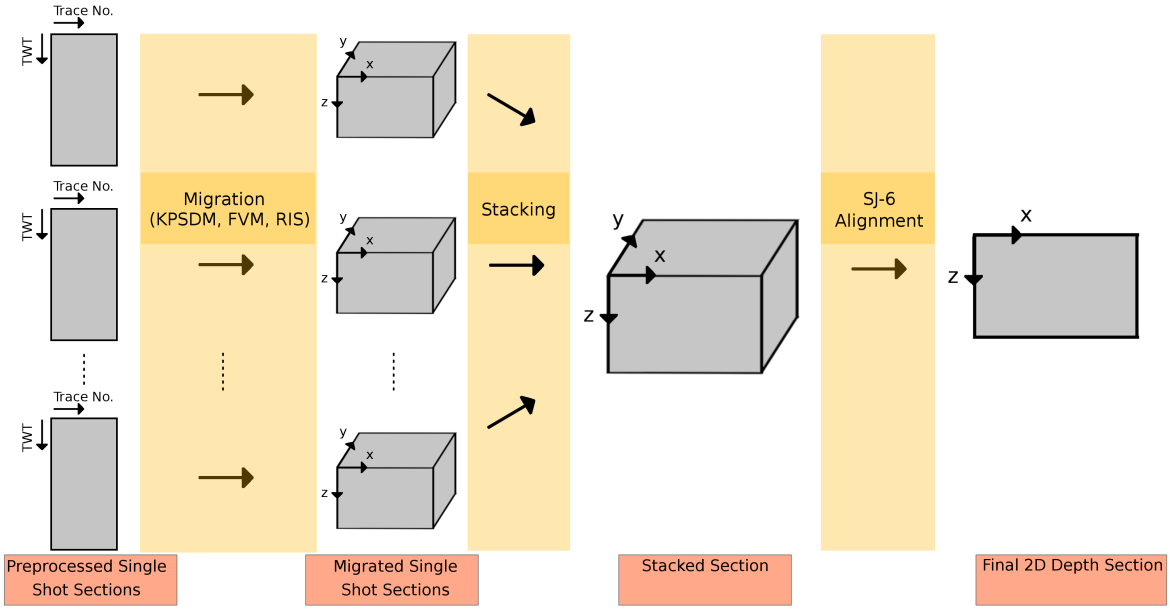

Figure 4.13: *General workflow of the migration processing sequence. Migration schemes are implemented in 3D. The reflectivity values within the stacked 3D section are aligned to line SJ-6 in order to obtain a final 2D depth image.*

The reflectivity values from beneath the actual receiver line are extracted from the stacked 3D volume and displayed in a 2D depth section to better visualize the final results. The following paragraph describes this procedure in detail.

Visualization of the Migration Results

The data quality within the migrated 3D sections strongly depends on the receiver locations along line SJ-6 that is partially crooked in some regions. The image quality is highest beneath the receiver line and decreases apart from it. The visualisation of the final results therefore becomes difficult as every depth slice throughout the 3D section needs to be examined separately. Figure 4.14 shows depth slices through the stacked 3D section of the Fresnel Volume migrated data. The inconsistency of the image quality can clearly be seen by the variable distribution of high reflectivities in accordance to the position of the receiver line.

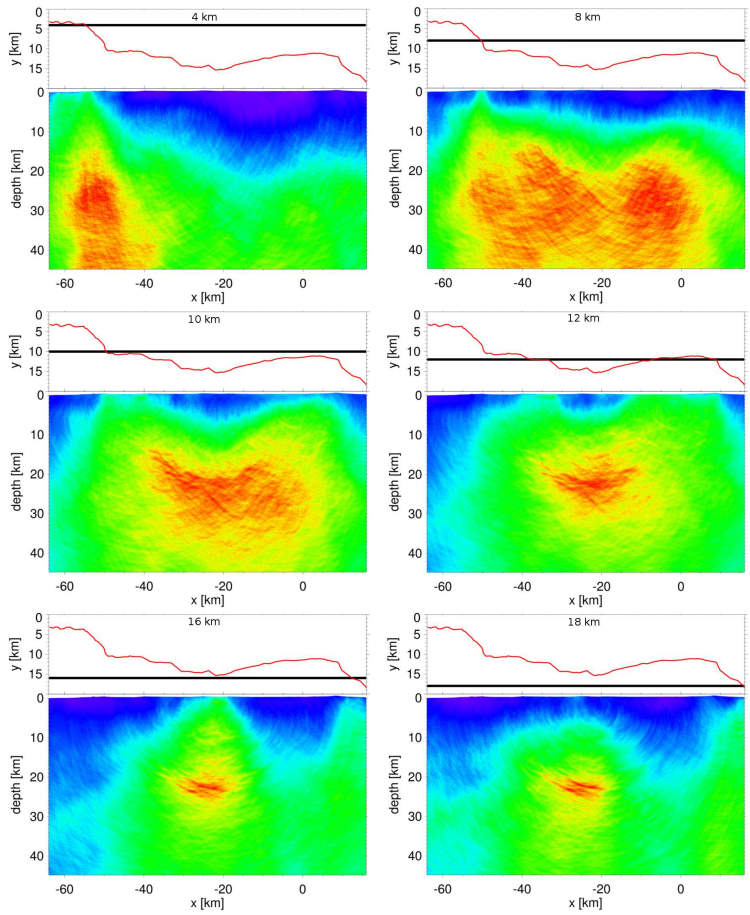

Figure 4.14: *Depth slices through the stacked 3D section of the Fresnel Volume migrated data and respective map views of the southwestern SJ-6 line segment. Black lines in map view indicate the location of the depth slices, red lines represent the SJ-6 receiver line.*

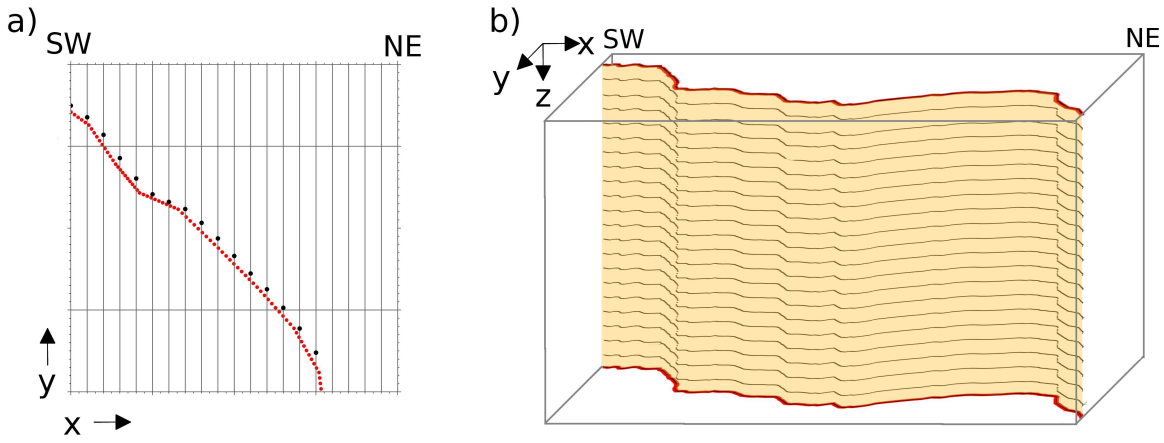

Figure 4.15: *Adjustment procedure to obtain a final 2D depth section. a) Detailed map view of a particular crooked SJ-6 line segment, red points are true receiver locations and black points adjusted receiver locations, respectively. b) Depth projection of the adjusted receiver locations. The orange shaded plane includes the results for the final 2D depth image.*

In order to simplify the visualisation procedure, final 2D depth images are produced in the following that provide the migration results from beneath the actual receiver line. The receiver positions are therefore adjusted to the grid node positions of the subsurface model. In the following explanation y denotes the component perpendicular to the predominating orientation of line SJ-6, that is northwest-southeast for the southwestern line segment and north-south for the eastern line segment. Accordingly x denotes the direction along the predominating direction of line SJ-6, southwest-northeast for the soutwestern segment and west-east for the eastern segment, respectively. Figure 4.15 a) presents a detailed map view of line SJ-6 where receiver locations deviate extremely in y-direction. Red points represent true receiver positions and vertical gray lines represent grid node positions along the x-direction. In the first step, all receiver locations that are located between each of two grid nodes (vertical gray lines in Figure 4.15 a)) along the x-direction are identified. Secondly, the average value of the receivers y-components in between each grid node pair is determined and the result is assigned to the easternmost of the grid node pair (black points in Figure 4.15 a)). In the next step, the adjusted locations are projected to each depth layer in the subsurface model (see Figure 4.15 b)) providing a set of locations that define a plane beneath the receiver line. The 3D migration results are finally interpolated to these locations within that particular plane. The results presented in the following sections and in chapter 5 are 2D depth images that have been obtained by applying the above described procedure. High reflectivities will be illustrated by red colours and low reflectivities by green to blue colors, respectively.

4.4.1 Kirchhoff Prestack Depth migration

In the following, Kirchhoff Prestack Depth migration is applied to the SJ-6 data set. For this, travel time tables are required as further input parameter that provide the diffraction curves (two-way travel time isochrones). These are calculated in advance under consideration of the velocity model as described in section 4.3.3. The preprocessed wavefield is then distributed or smeared along these isochrones in dependence of the recorded two-way travel times. Figure 4.16 presents three 2D depth sections of particular migrated single shot gathers from different shot point positions along the southwestern line segment. Shot point locations of the top and middle 2D depth sections are at x = -54 km and -24 km southwest of the San Andreas fault. The bottom 2D depth sections source point is located at x = 6 km northeast to the San Andreas fault, respectively. The size of the corresponding receiver spreads is marked by the triangles representing the first and last active receiver along the corresponding receiver spreads. Note that the maximum offset is only 1.8 km. High reflectivities are distributed within the entire subsurface plane within all three sections. It can be seen that the reflectivities apart from the receiver spread are strongest and broadly distributed almost along the entire two-way travel time isochrones. But directly beneath and in the vicinity of the receiver spread the imaged features are more distinctive and locally restricted along the two-way travel time isochrones.

Standard Stacking Procedure

In order to improve the signal-to-noise ratio and to obtain a structural image from along the entire profile line segment all migrated single 3D volumes are stacked and afterwards adjusted to the actual acquisition line according to the procedure described in section 4.4. Lateral amplitude balancing is applied to the final 2D depth sections after stacking.
A conventional *phase stacking* is performed first meaning that the migrated wavefield of the single shot sections is stacked.

Figure 4.16: (following page) *Migrated single shot sections adjusted to the acquisition line for different shot point locations along line SJ-6. Black triangles mark the x-receiver positions of the first and the last active receivers of the respective receiver spreads; black stars denotes the shot point positions.*

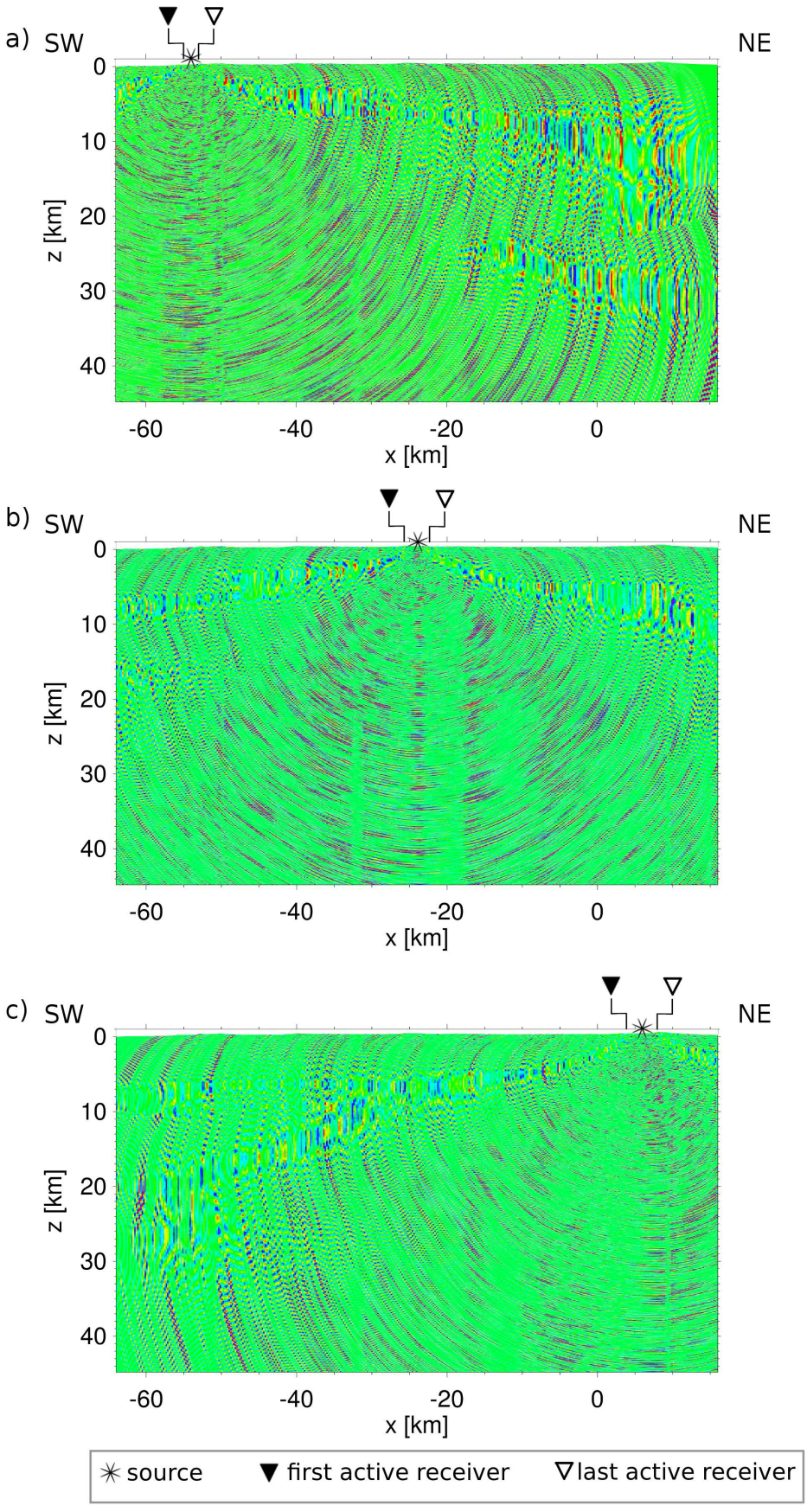
a)
SW
NE
0
10
20
30
40
z [km]
-60
-40
-20
0
x [km]
b)
SW
NE
0
10
20
30
40
z [km]
-60
-40
-20
0
x [km]
c)
SW
NE
0
10
20
30
40
z [km]
-60
-40
-20
0
x [km]
source
first active receiver
last active receiver

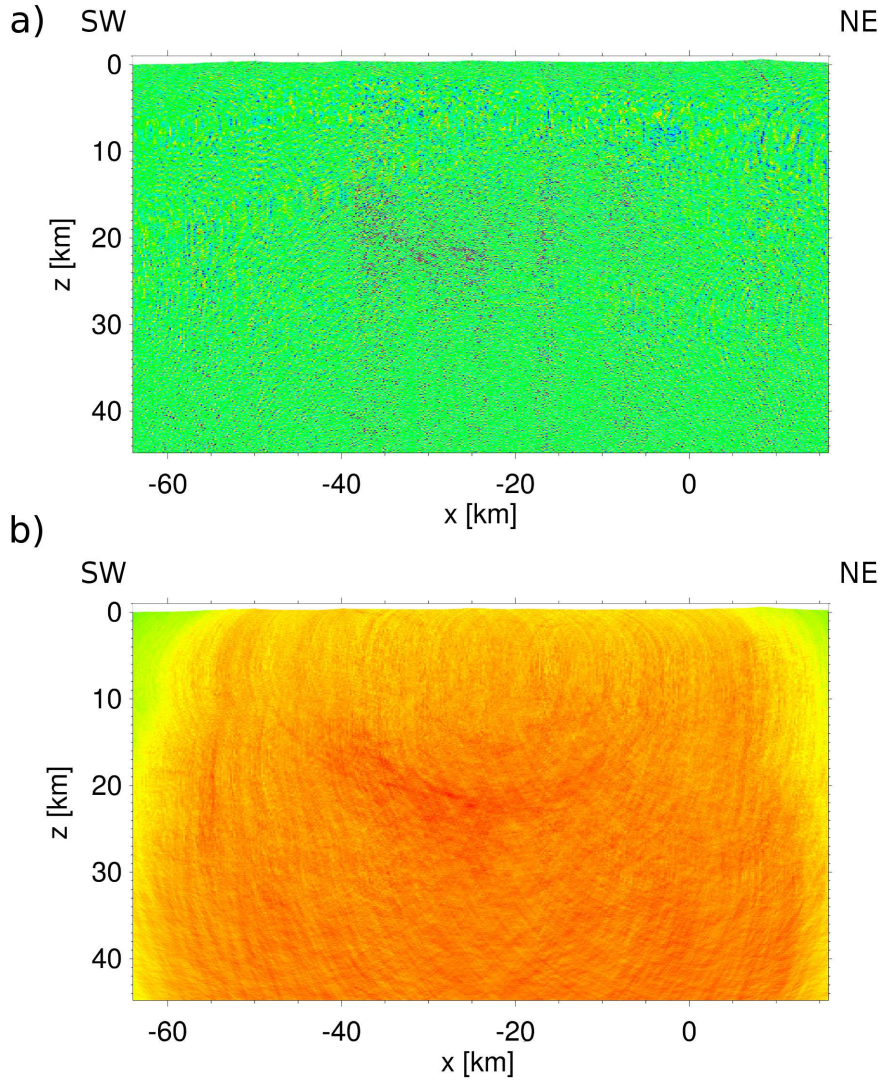

Figure 4.17: *Results for a) phase stacking and b) absolute amplitude stacking for the south-western SJ-6 line segment.*

The result is shown in Figure 4.17 a). The image quality is rather low. Solely in the central part of the image between $x = -20$ km and -40 km some northeast dipping structures can slightly be recognized at depths of approximately 20 km.

To further improve the image quality, absolute amplitudes are stacked in the next step which is illustrated in Figure 4.17 b). In the center of the image the northeast dipping structures are strinkingly pronounced and some single reflector elements can be distinguished. In the shallow subsurface very weak and indistinct subhorizontal reflectors are hardly visible in the centre of the image. However this image is not appropriate for any interpretation as the value of information is still low.

The low signal-to-noise ratio is the result of migration noise that is produced in regions within the single subsurface volumes lying apart from the corresponding receiver spreads (see Figure 4.16). Migration noise superimpose the desired reflector signals especially in the shallower regions apart from the receiver spreads due to the short receiver spreads. The survey layout was once designed for shallow subsurface investigations using the classical CMP-stacking procedure where only shallow subsurface regions directly beneath the survey line are considered. As this work aims to produce images of the entire crust, a large 3D subsurface volume is chosen. The difference in the overall subsurface volume size and the size of the single receiver spreads is a considerable problem that strongly affects the image quality.

Modifcation of the Standard Stacking Procedure in the Case of Low Data Coverage

To deal with the problem described above the migrated single shot sections are clipped to a particular region around the corresponding receiver spreads prior to stacking.
With the given acquisition layout horizontal structures can only be imaged directly beneath the respective receiver spreads. Apart from the receiver spreads only inclined structures can be recorded. The greater the reflectors distance to the receiver spread the more it has to be inclined to be recorded at the surface. In the presence of inclined reflectors in the lower crust the region producing potential reflection energy increases with depth. Therefore, reflection signals overlap to a greater extend in the lower crust as they do

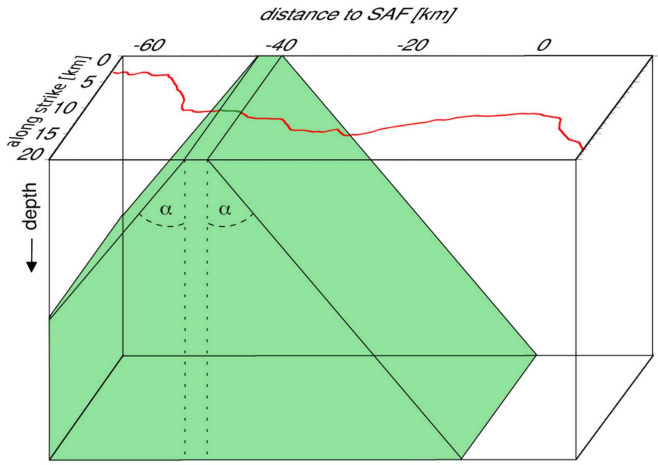

Figure 4.18: *The migrated single shot sections are restricted to the region around the actual receiver spread (green segment); subsurface points outside the green shaded subvolume are set to zero prior to stacking; the isolated subvolume increases with depth according to angle α.*

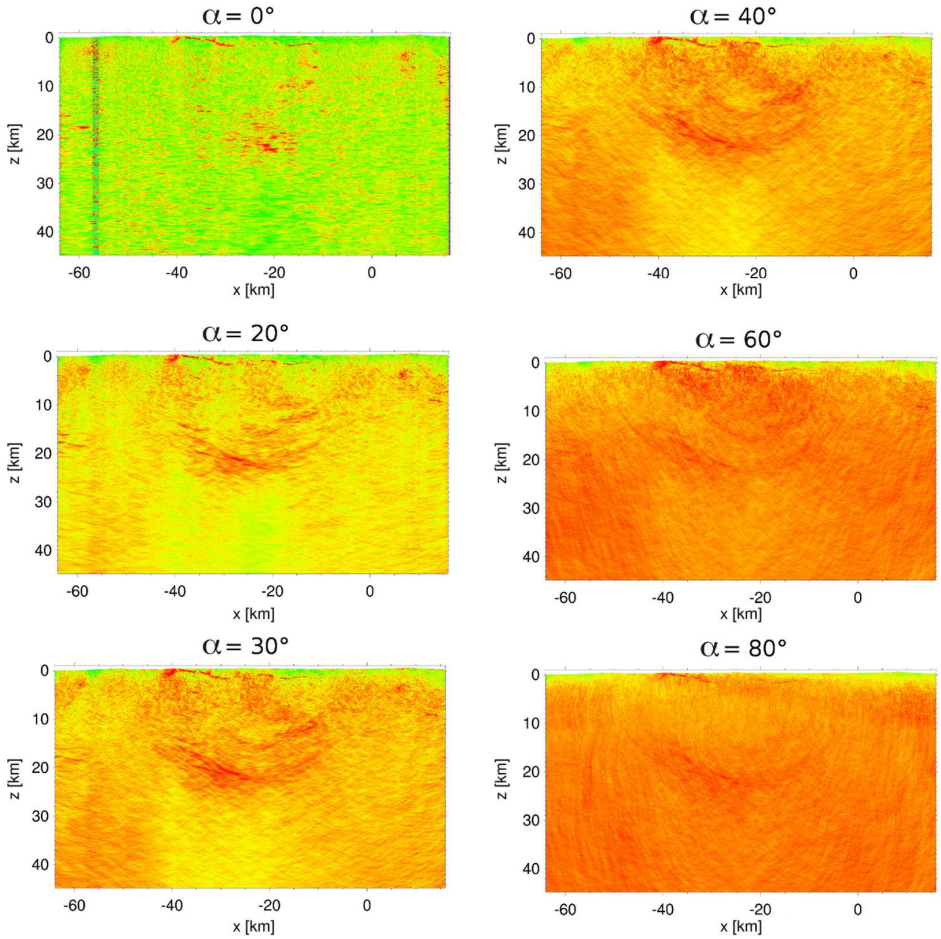

Figure 4.19: *Stacking results for different clipping angles α.*

in the shallower crust when the migrated single shot sections are stacked. Consequently, shallower structures are to a greater extent affected by the superposition of migration noise from distant migrated shot sections than deeper structures.

For this reason the migrated single sections are clipped to the region around the corresponding receiver spreads by setting amplitudes outside a designated subvolume (green shaded area in Figure 4.18) to zero. The angle α determines the lateral extend of the designated subvolume with increasing depth. Thereby the choice of α defines the grade of reflector dips that are considered. Figure 4.19 presents clipped and stacked 2D sections for different values of α. For $\alpha = 0°$ designated subvolumes directly beneath the respective receiver spreads are stacked. Subhorizontal structures are well imaged in both, the shallow and lower crust, respectively. Only in the shallow crust between x = -40 km and x = -10 km slightly dipping structures are visible. With increasing α steeper dipping structures are included into the clipped section. Nevertheless, superposition of noise with reflector signals increases simultaneously.

Average dipping angles of approximately 30° to 40° can be estimated from the unclipped amplitude depth section. Using the estimated dipping angles, α can be determined using geometrical relations. For the given range of dipping angles an α of 40° is chosen for clipping.

The clipping of the migrated single sections causes local amplitude differences within the 3D images. For this reason the amplitudes in the stacked volume are balanced by dividing the sum at each grid node by the number of non-zero values that have been stacked at the respective grid node. Afterwards interpolation to the averaged location of line SJ-6 as described above gives the final 2D depth image that comprises both, information on shallow structures and on deep structures along line SJ-6, respectively, as can be seen in Figure 4.20.

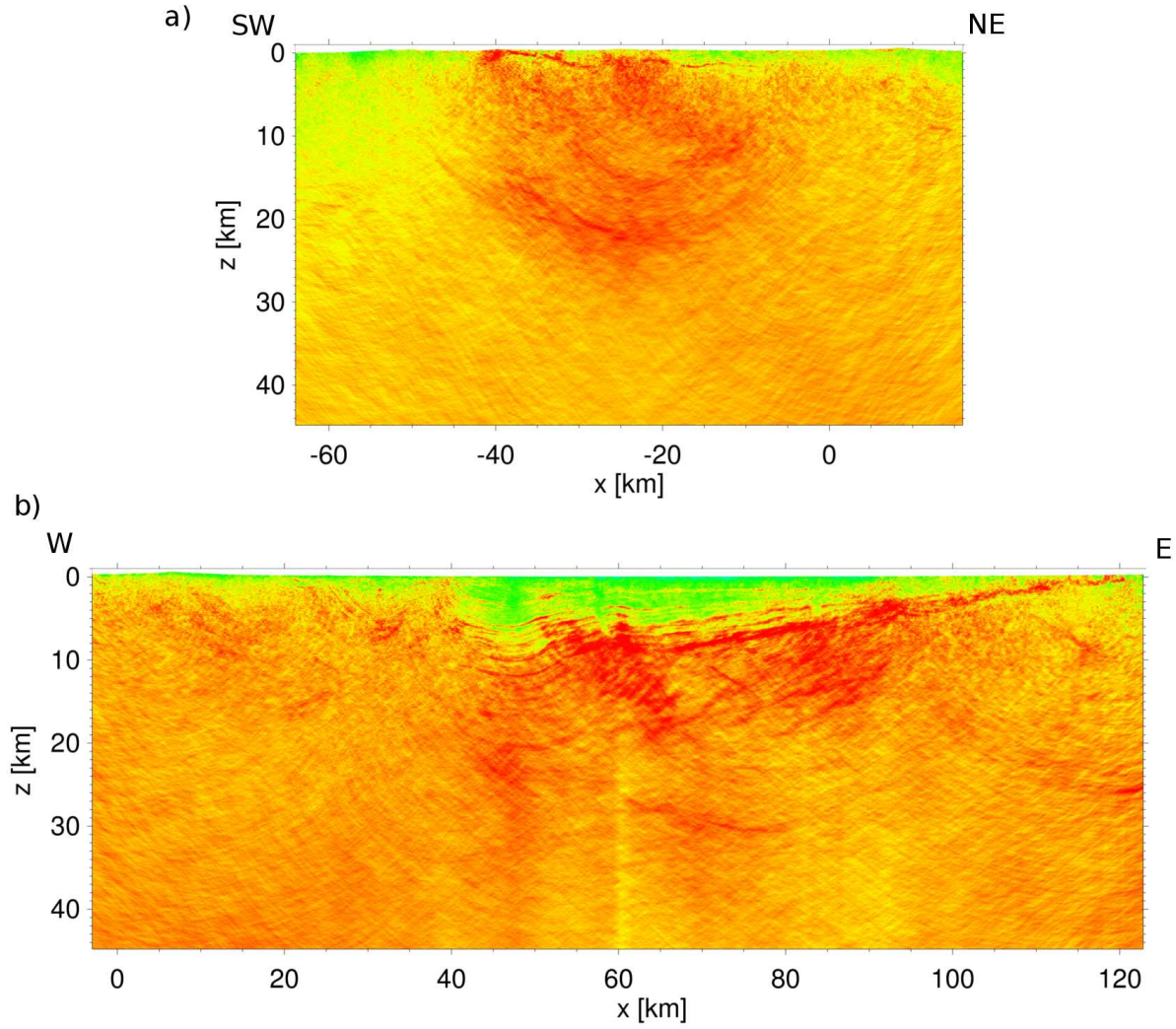

Figure 4.20: *Final Kirchhoff Prestack Depth migration image along a) the southwestern line segment and b) the eastern line segment of line SJ-6 after amplitude stacking of clipped migrated single shot sections.*

4.4.2 Fresnel Volume migration

The processing sequence of Fresnel Volume migration is in principle similar to that of Kirchhoff Prestack Depth migration apart from additional routines that are added to perform the spatial restriction of the migration operator. The criterion for the restriction is the size of the Fresnel Radius of the corresponding rays that are calculated separately for all data samples. A more detailed overview on the processing sequences of Fresnel Volume migration is given in Figure 4.21. The Fresnel Radius is estimated according to equation 3.10 in section 3.2 under consideration of the dominant period, that is estimated from the data, and the ray propagator elements. The latter are calculated for each time sample by performing a ray tracing procedure. The starting angles for the ray tracing are obtained by local slowness calculations as described in section 3.2. Additionally, P-wave velocity information at the acquisition surface and the spatial derivatives of the velocity field are required to perform the ray tracing procedure. The amplitudes are smeared along the diffraction surfaces but weighted in accordance to the local position of the diffraction surface points to the Fresnel Radii of the corresponding rays (see equation 3.11 in section 3.2). The weighted amplitudes along all diffraction surfaces are finally summed to generate the migrated section.

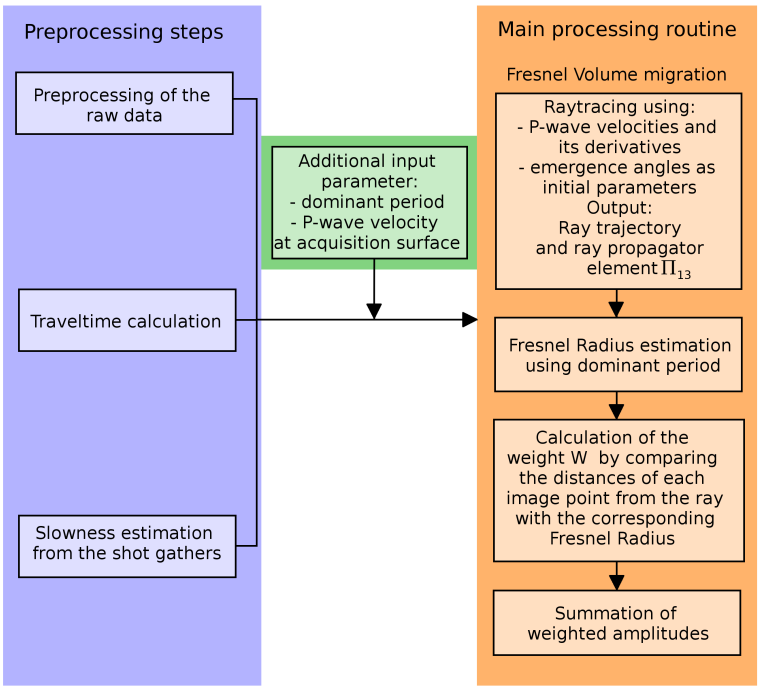

Figure 4.21: *Processing sequence of Fresnel Volume migration modified after Sick (2006).*

Emergence angle estimation along line SJ-6

In section 3.2 the principle of emergence angle estimation was introduced. Horizontal and vertical slowness values are calculated that provide the initial orientation for the ray tracing procedure. In the case of straight 2D receiver lines the wavefield is usually backpropagated in a 2D subsurface model that spans a vertical plane below the survey line. Therfore it is sufficient to now the vertical slowness p_z and the horizontal slowness p_x that is oriented inline with the survey line. In contrast, the SJ-6 data have partly been acquired along windy roads as some regions in the Coast Ranges are difficult to access. Consequently, the receiver locations alternate notably perpendicular to the predominating southwest-northeast orientation and west-east orientation, respectively, of the SJ-6 survey line. In order to account for the true source and receiver positions the migration scheme was implemented in 3D.

At first, pairs of horizontal and vertical slownesses for each time section are calculated. The horizontal slowness is considered as the slowness along the x-axis within our local coordinate system that is for the southwestern part of the profile oriented perpendicular to the strike of the San Andreas fault surface trace and for the eastern part oriented in east-west direction, respectively. The y-axis is horizontally oriented perpendicular to the x-axis. During ray tracing, rays are propagated into the subsurface model starting at each particular receiver location. As the receiver positions along the y-axis are not yet considered, the initial orientation of each ray emenating at the receivers is limited to the x-z-plane spaned beneath each receiver. Figure 4.22 illustrates this situation for three receivers along a crooked acquisition line.

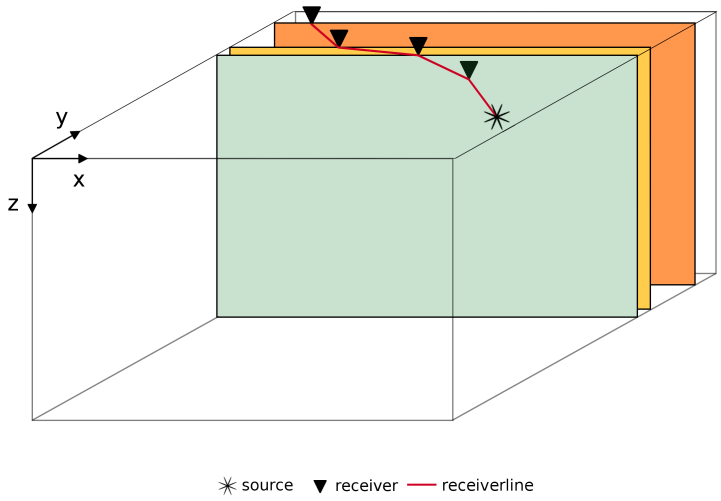

Figure 4.22: *Emergence angles estimated under consideration of one horizontal slowness component p_x are oriented within x-z-planes directly beneath the receiver locations.*

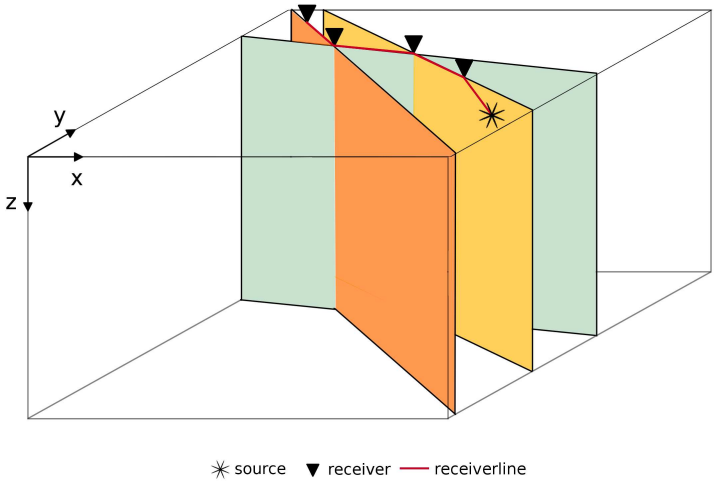

Figure 4.23: *Under consideration of two horizontal slowness components, the vertical plane rotates in the direction of the corresponding receiver offsets.*

As the receiver positions vary significantly along the y-axis the energy is smeared within different x-z-planes according to each particular receiver position without considering the actual orientation of the receiver line. In the case of roughly straight receiver line segments energy is imaged beneath the actual acquisition line. This is not the case along crooked survey lines. In this case, the energy is smeared far away from the receiver line and causes artefacts within the 3D subsurface image. The objective of the following approach is to distribute the reflection energy as accurately as possible below the actual acquisition line during Fresnel Volume migration.

In order to enhance the image quality and to reduce migration artefacts the horizontal slowness $p_h(x,t)$ is calculated according to the true receiver distances in the x-y-plane and accordingly weighted to the respective x- and y-components of the true horizontal offset $\vec{h} = (dx, dy)$. Thus, two horizontal slowness values can be obtained according to the following equations:

$$p_x(x,t) = p_h(x,t) \cdot \frac{dx}{\mid \vec{h} \mid} \tag{4.8}$$

$$p_y(x,t) = p_h(x,t) \cdot \frac{dy}{\mid \vec{h} \mid} \tag{4.9}$$

The initial emergence angle provided for ray tracing now considers the true orientation of the receiver line. Finally, the energy is smeared within a depth plane approximately beneath the receiver line that reflects the orientation of the corresponding receiver offsets. Figure 4.23 shows the vertical planes beneath each receiver in which the inital ray is propagated when the two horizontal slowness components p_x and p_y are considered. Figure 4.24 demonstrates the result of slowness computation for one single shot gather. The newly

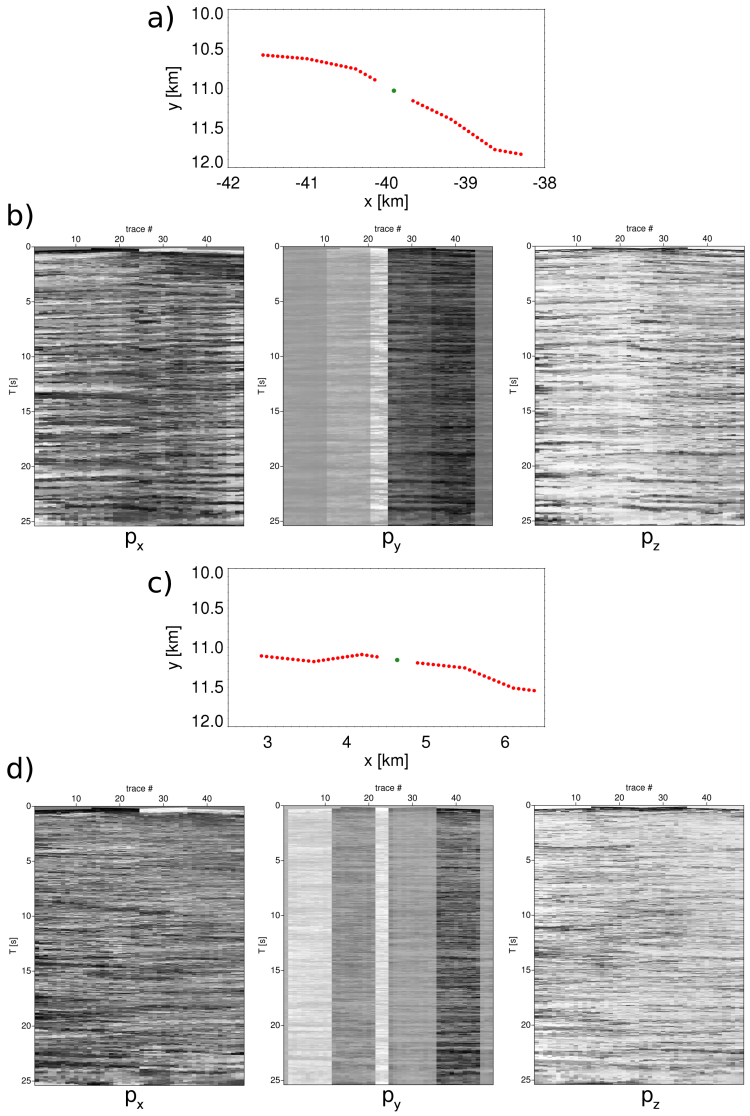

Figure 4.24: *Slowness estimation results for two individual single shot sections. a) and c): respective active receiver line segments in map view, red dots are receiver positions, green dot is the source position, respectively. b) and d) time sections representing the calculated slowness components p_x, p_y and p_z.*

determined slowness component p_y varies laterally in relation to the relative receiver offsets in y-direction. The above presented procedure allows to improve the quality of the imaging results as reflection energy is to a higher extent localized beneath the actual receiver line. Although the imaging technique is implemented in 3D and the true source and receiver locations are considered, it is not possible to image 3D geological structures or identify 3D effects. The true orientation of the recorded wavefield remains unknown and it must be considered that 3D effects influence the image quality and may cause artefacts.

Impact of the second horizontal slowness component on the image quality

The objective of the above presented approach is to attribute the reflectivity values as close to the acquisition line as possible to increase the signal-to-noise ratio of the final 2D depth sections. In the following, the impact of the emergence angle estimation technique on the seismic imaging result is demonstrated. Figure 4.25 shows horizontal slices throught the final Fresnel Volume migrated and stacked subsurface volumes at depths of 1 km, 10 km and 20 km, respectively. The slices on the left hand side of Figure 4.25 represent the imaging results obtained from the standard *straight line approach* that accounts for one horizontal slowness p_x and the right hand side images present the imaging results obtained by the *crooked line approach* that accounts for two horizontal slowness components p_x and p_y. Warm colors represent high reflectivities and cold colors low reflectivities, respectively. It can be recognized that high reflectivity values concentrate within a quite narrow zone around the acquisition line for shallow depths that widens with increasing depths. This is due to the fact that the data coverage is higher for the deeper regions and that the Fresnel Zones slightly increase with depth. The energy is then smeared along larger segments of the two-way travel time isochrones with increasing vertical distance to the corresponding receiver.

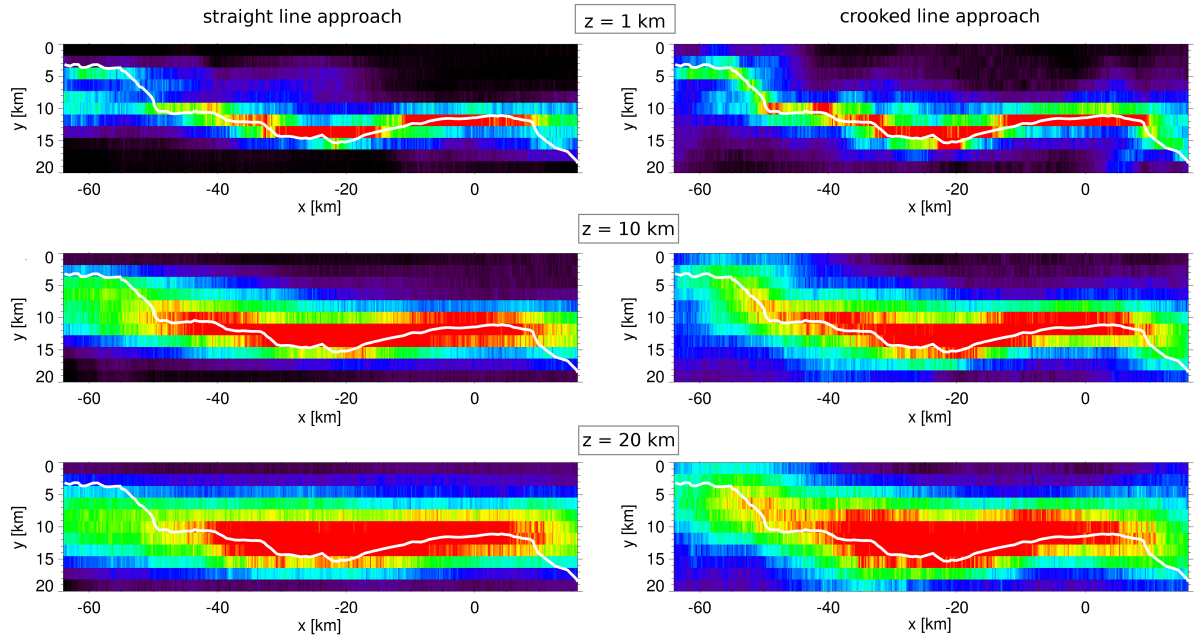

Figure 4.25: *Horizontal x-y-slices through the Fresnel Volume migrated and stacked 3D volumes for $z = 1$ km (top), $z = 10$ km (middle) and $z = 20$ km (bottom). Left hand side figures: imaging results considering one horizontal slowness component p_x, right hand side figures: imaging results considering two horizontal slowness components p_x and p_y, respectively. The white line marks the acquisition line along the southwestern SJ-6 line segment.*

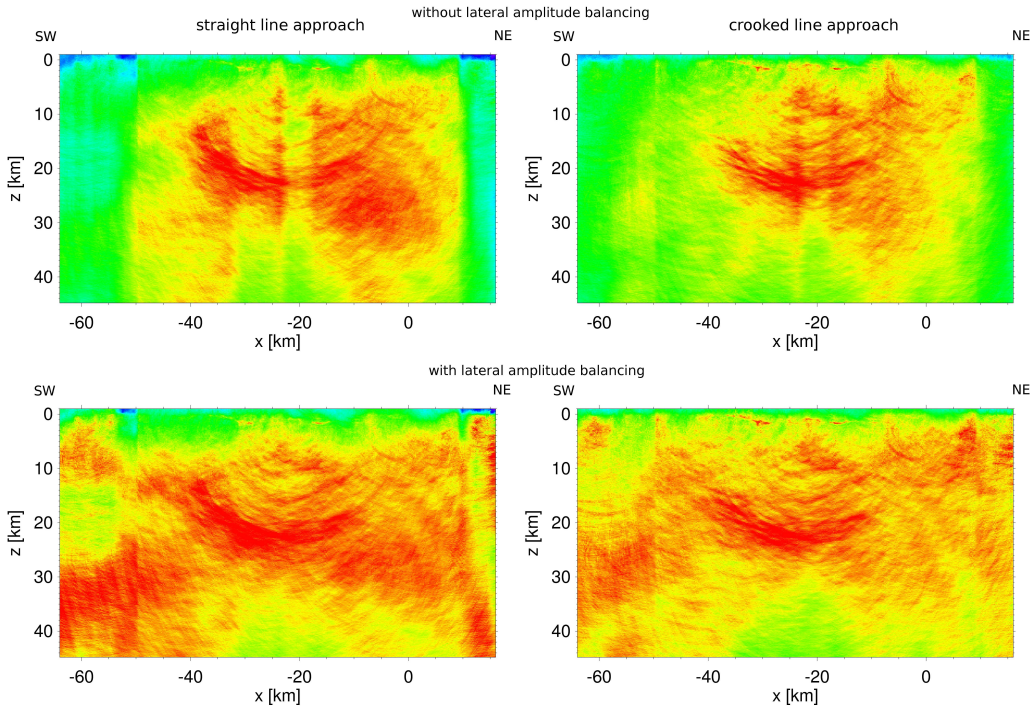

Figure 4.26: *Fresnel Volume Migration depth sections obtained by consideration of one horizontal slowness component p_x (left hand side) and two horizontal slowness components p_x and p_y (right hand side), respectively. Reflectivities in the bottom depth sections are laterally balanced.*

The amount of high reflectivity values is more closely attributed beneath the acquisition line in the right hand side figures of Figure 4.25 that represent the crooked line approach for emergence angle estimation. Whereas the left hand side figures of the straight line approach show a large amount of high reflectivity values that is located offside the receiver line. These reflectivities are not properly imaged and produce a significant amount of migration noise. Furthermore, this particular reflectivity quantities do not provide any reflectivity information beneath the corresponding receiver line position and are therefore absent in the final 2D image. The corresponding migrated 2D depth sections are shown in Figure 4.26. The left hand side images are determined with the straight line approach and the right hand side images with the crooked line approach, respectively. The top images are latterally unbalanced while the bottom images contain lateral amplitude balancing. The crooked line approach provides seismic images of enhanced signal-to-noise ratio compared to the straight line approach. Noise produced by insufficiently imaged signals due to large y-components of the receiver locations is significantly reduced by the application of the crooked line approach. Lateral amplitude balancing clearly enhances the reflectivity values at the margins of the depth sections.

Fresnel Volume Migration

In the following, Fresnel Volume migration is applied to the SJ-6 data. The distribution of the recorded amplitudes along the two-way travel time isochrones is restricted to Fresnel Zones that are calculated for rays that are propagated into the subsurface model under consideration of the velocity field and the initial emergence angle at the corresponding receiver positions. Figure 4.27 shows selected rays and the corresponding Fresnel Zones in the case of one single example trace. In most of the cases the Fresnel Zones increase with increasing time step.

Figure 4.28 shows the same three migrated single shot sections that have previously been presented in section 4.4.1. A comparison of the migrated single shot sections shows significant differences between the Kirchhoff Prestack Depth images and the Fresnel Volume image. The spatial restriction of the migration operator causes the amplitudes to concentrate beneath the actual receiver spreads. Migration noise from regions apart from the receiver spreads as observed in the Kirchhoff Prestack Depth images is considerably reduced. For that reason clipping of the migrated single shot sections prior to stacking is omitted in this case.

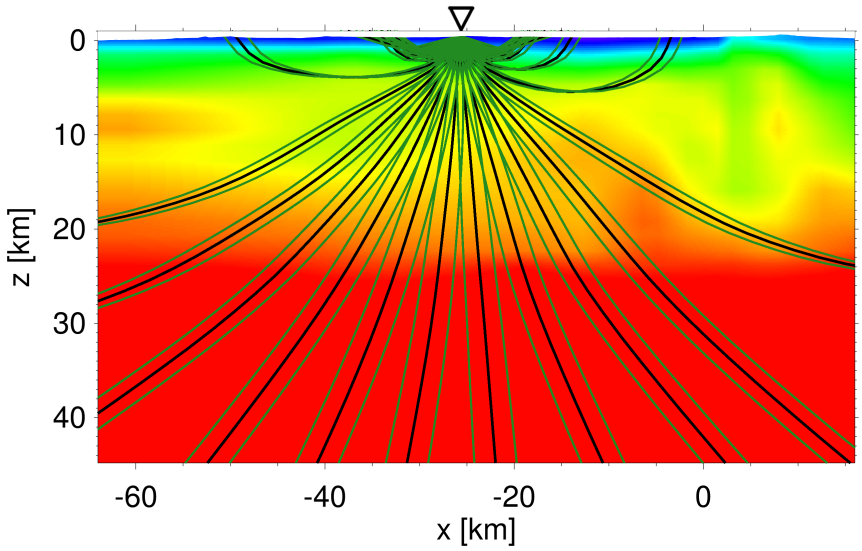

Figure 4.27: *Ray paths for selected time samples of one particular trace infront of the velocity model. Green lines border the Fresnel Zones.*

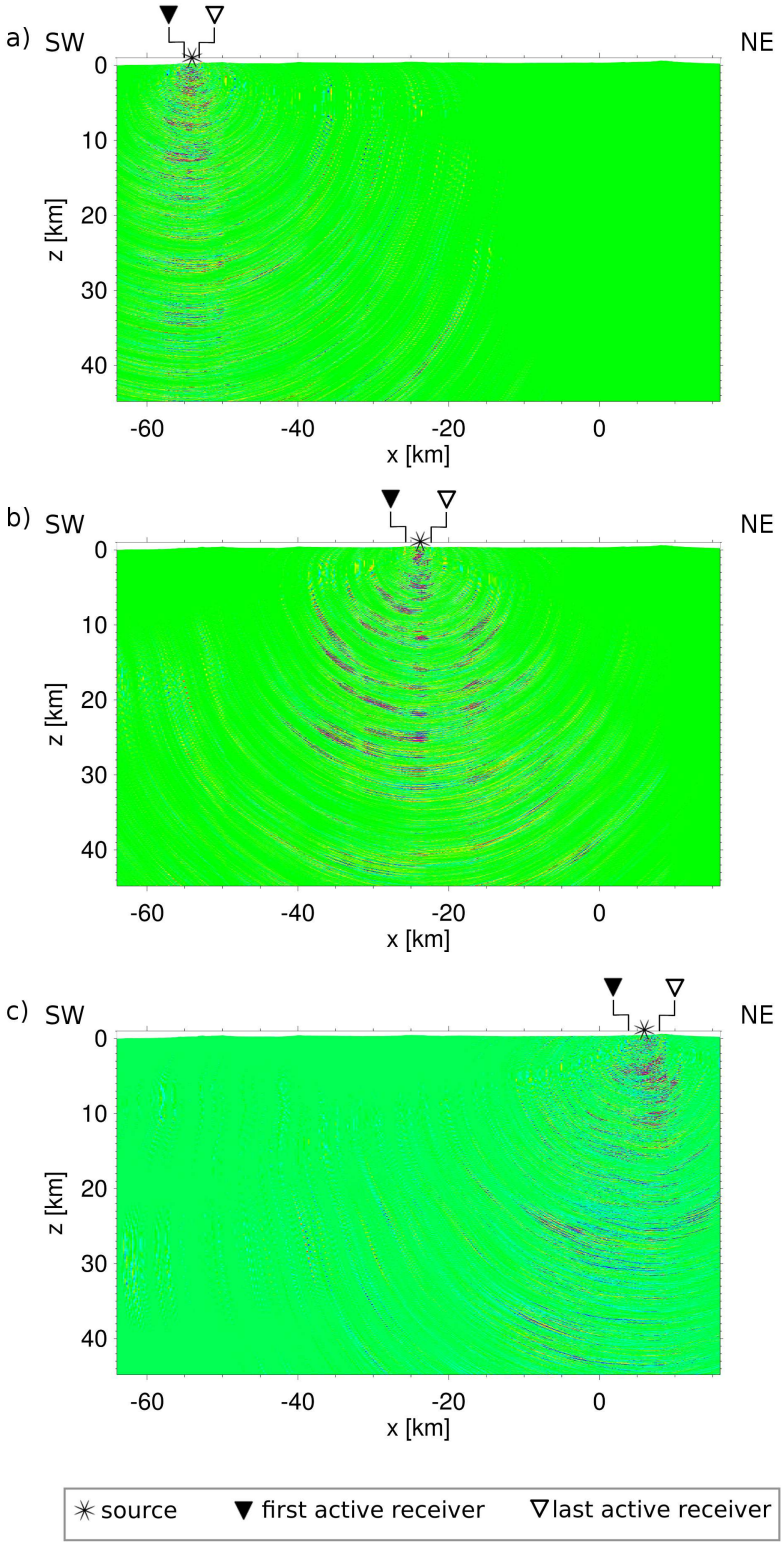

Figure 4.28: *Migrated single shot sections using Fresnel Volume migration adjusted to the survey line for different shot point locations along line SJ-6. Black triangles mark the x-receiver positions of the first and the last active receivers of each spread; black star denotes the shot point position.*

Again, the migrated 3D single shot sections are stacked in order to obtain a depth image from along the entire survey line segments as well as to improve the signal-to-noise ratio. The 2D results of phase stacking as well as the absolute amplitude stack are shown in Figure 4.29 a) and b), respectively. Lateral amplitude balancing is performed on all depth sections after the data have been adjusted to the SJ-6 receiver line.
The phase stack in Figure 4.29 a) includes little structural information although the image quality is significantly enhanced compared to the Kirchhoff Prestack Depth phase stack (Figure 4.17 a)). Distinct features can even be recognised in the shallower regions and at the edges of the depth section. The amplitude stack is not as much affected by migration noise as the corresponding Kirchhoff Prestack Depth amplitude stack and again shows a strong band of northeast dipping reflectors. However, the amplitude stack so far lacks of information on the shallow subsurface.
Due to the short survey spreads, the data coverage is low, especially in the shallow subsurface. The distribution of reflectivities is therefore quite unbalanced within the subvolume. Reflectivities in the shallower regions can be amplified by weighting the stacked values at each grid point by the number of non-zero values that have been stacked at each corresponding node. Figure 4.29 c) demonstrates the effect of weighting. However, deeper reflectivity signals are attenuated compared to the absolute amplitude stack. In order to obtain an image that provides both, information on the lower crust and the upper crust, respectively, the weighted and the absolute stacks are normalized to their respective maxima and summed afterwards. The final result for the southwestern and the eastern SJ-6 line segments are presented in Figure 4.30 and further discussed in chapter 5.

Figure 4.29: (following page) *Results of a) phase stack, b) stack of ambsolute amplitudes and c) weighted stack of absolute amplitudes, respectively.*

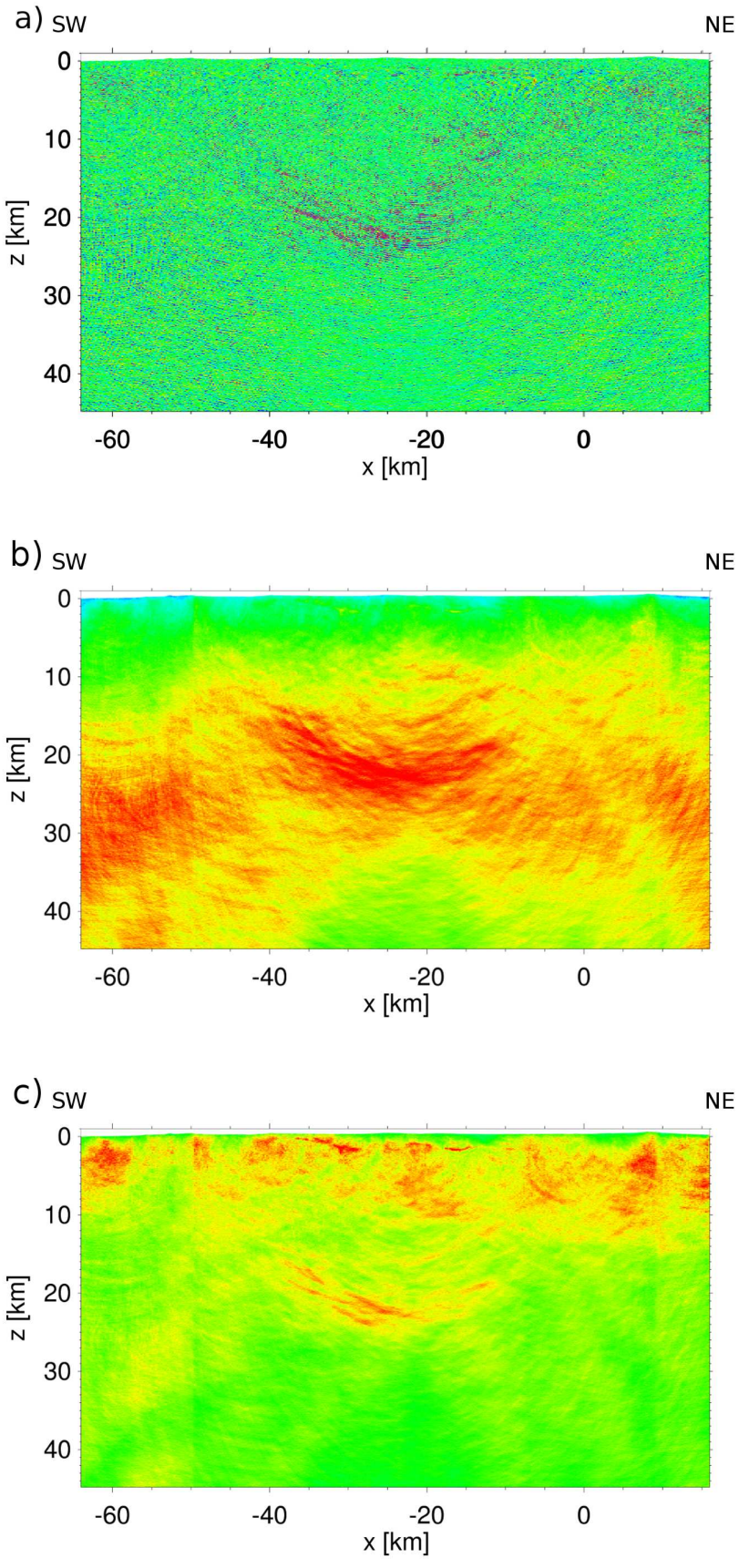
a) SW
NE
0
10
20
30
40
z [km]
-60
-40
-20
0
x [km]
b) SW
NE
0
10
20
30
40
z [km]
-60
-40
-20
0
x [km]
c) SW
NE
0
10
20
30
40
z [km]
-60
-40
-20
0
x [km]

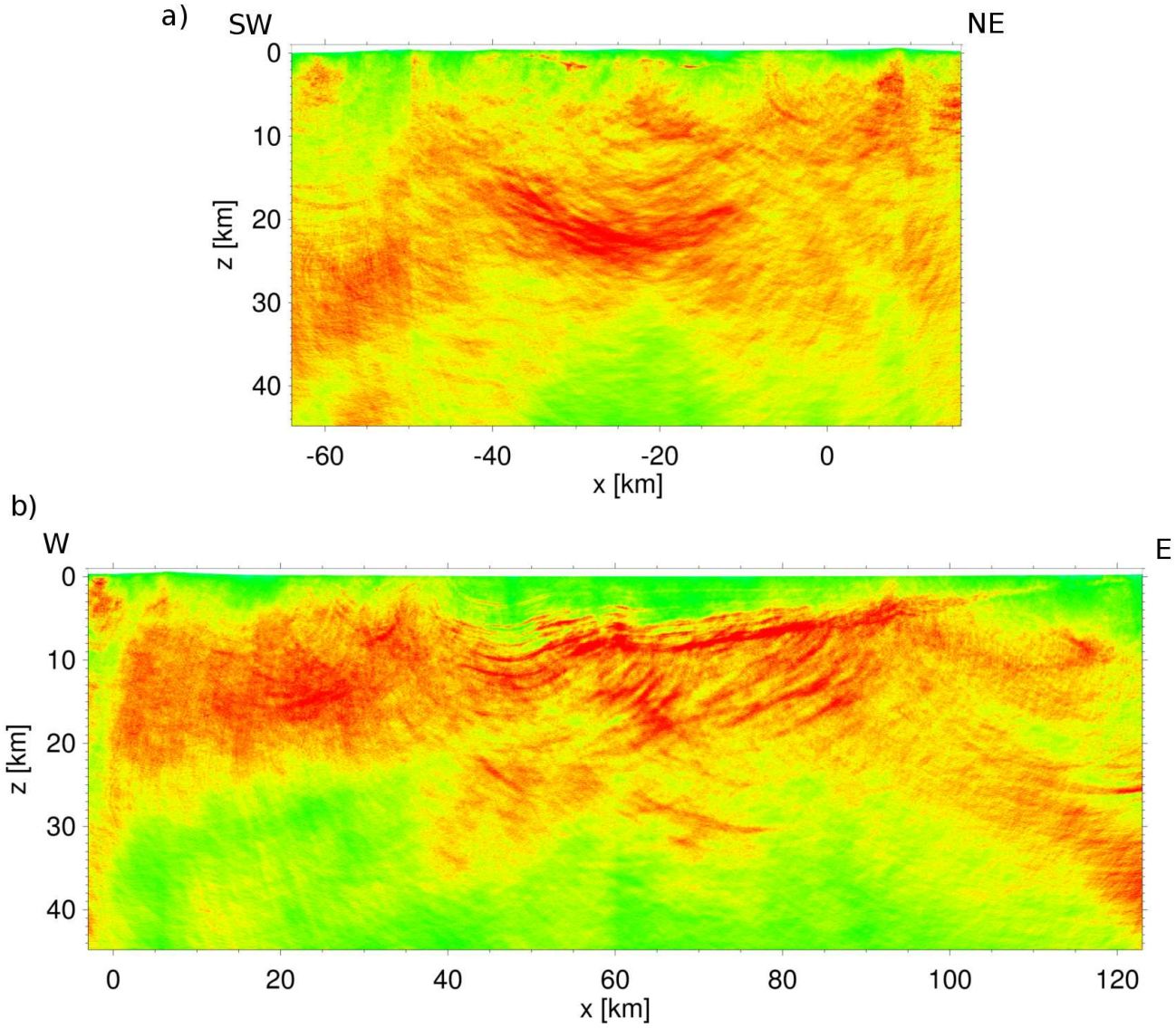

Figure 4.30: *Final Fresnel Volume migration image along a) the southwestern line segment and b) the eastern line segment of line SJ-6 after stacking and lateral amplitude balancing.*

4.4.3 Reflection Image Spectroscopy

In order to extract additional small-scale structures from the resulting depth images we apply Reflection Image Spectroscopy to the SJ-6 data set. As proposed by Yoon et al. (2009) the preprocessed data are bandpass filtered in several discrete frequency bands each containing a banwidth of 5 Hz. The general Reflection Image Spectroscopy workflow is presented in Figure 4.31. Three frequency bands are extracted in the range of $10 - 15$ Hz (low-frequency range), $15 - 20$ Hz (middle-frequency range) and $20 - 25$ Hz (high-frequency range), respectively using a trapezoidal bandpass filter as illustrated in Figure 4.32 a). A, B, C and D represent the corner frequencies. From B to A and from C to D the amplitudes are linearily tapered within a frequency range of 5 Hz. The central corner frequencies are represented by B and C.

Figure 4.32 b)-e) show the amplitude spectra for one single trace from the SJ-6 data set by way of example. The full-frequency range of this trace after crosscorrelation can be seen in Figure 4.32 b). Figures 4.32 c)-e) show the amplitude spectra of the three respective frequency bands after bandpass filtering for that particular trace sample. Each narrrow-frequency data set is migrated separately using Fresnel Volume migration. The respective dominant period for the determination of the Fresnel Radii is estimated from each of the narrow-frequency data sets separately.

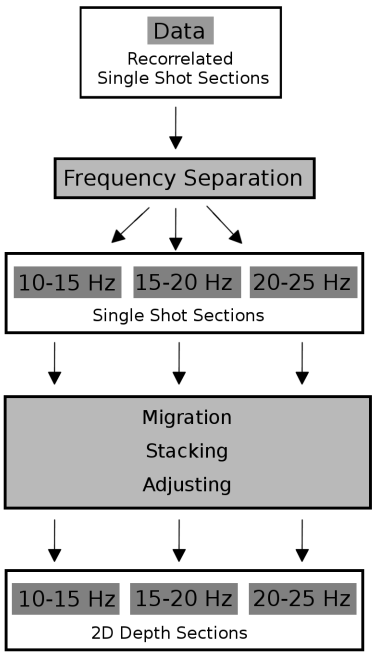

Figure 4.31: *Reflection Image Spectroscopy Workflow.*

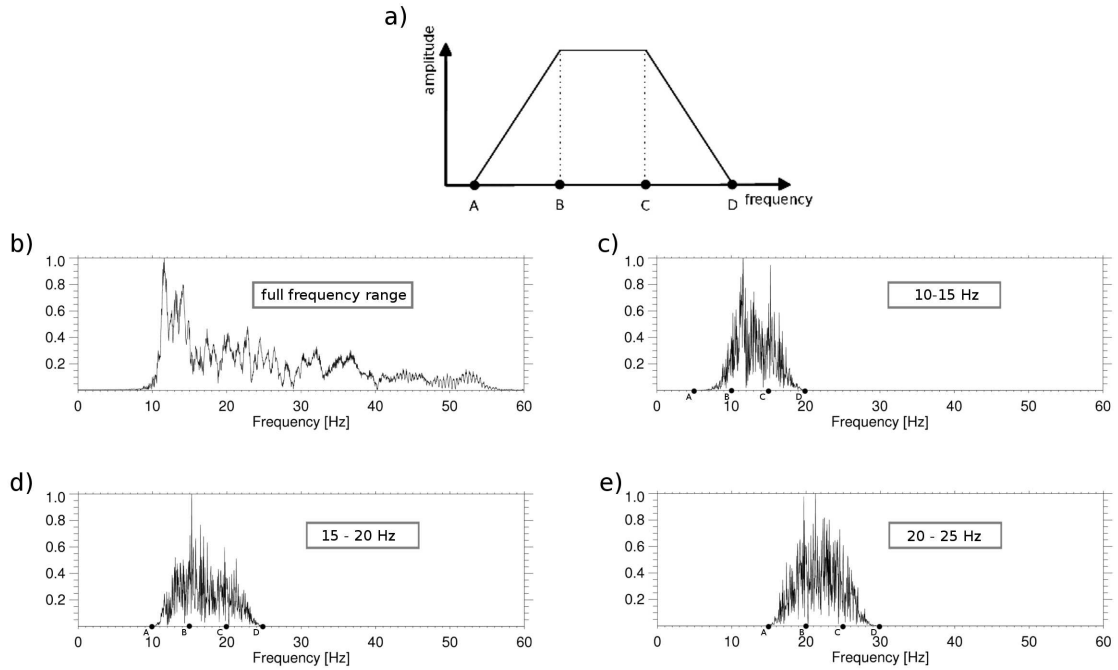

Figure 4.32: *a) Design of trapezoidal bandpassfilter. Corner frequencies are A,B,C and D. b) Full-frequency content of one SJ-6 data trace example after crosscorrelation c-e) Narrow-frequency data examples after application of the respective bandpass filter in the ranges of 10-15 Hz, 15-20 Hz and 20-25 Hz, respectively.*

It is 0.08 seconds for the low-frequency range data, 0.06 seconds for the middle-frequency range data and 0.04 seconds for the high-frequency range data set.
The stacking procedure and the adjustment of the 3D migrated data to line SJ-6 have exactly been performed as described in section 4.4.2.
Figure 4.33 shows the result of Reflection Image Spectroscopy for one single shot gather producing three depth sections, each for a different frequency band. A comparison of the depth sections shows that the intensity and the form of the reflectivity distribution significantly differs. The reflection energy of this single shot section is mainly concentrated in the low- and in the high-frequency range. The final seismic Reflection Image Spectroscopy images are presented in the following chapter.

Figure 4.33: (following page) *Migrated single shot sections for one data example after application of Reflection Image Spectroscopy. a) low-frequency image* $(10-15\ Hz)$*, b) intermediate-frequency image* $(15-20\ Hz)$ *and c) high-frequency image* $(20-25\ Hz)$*.*

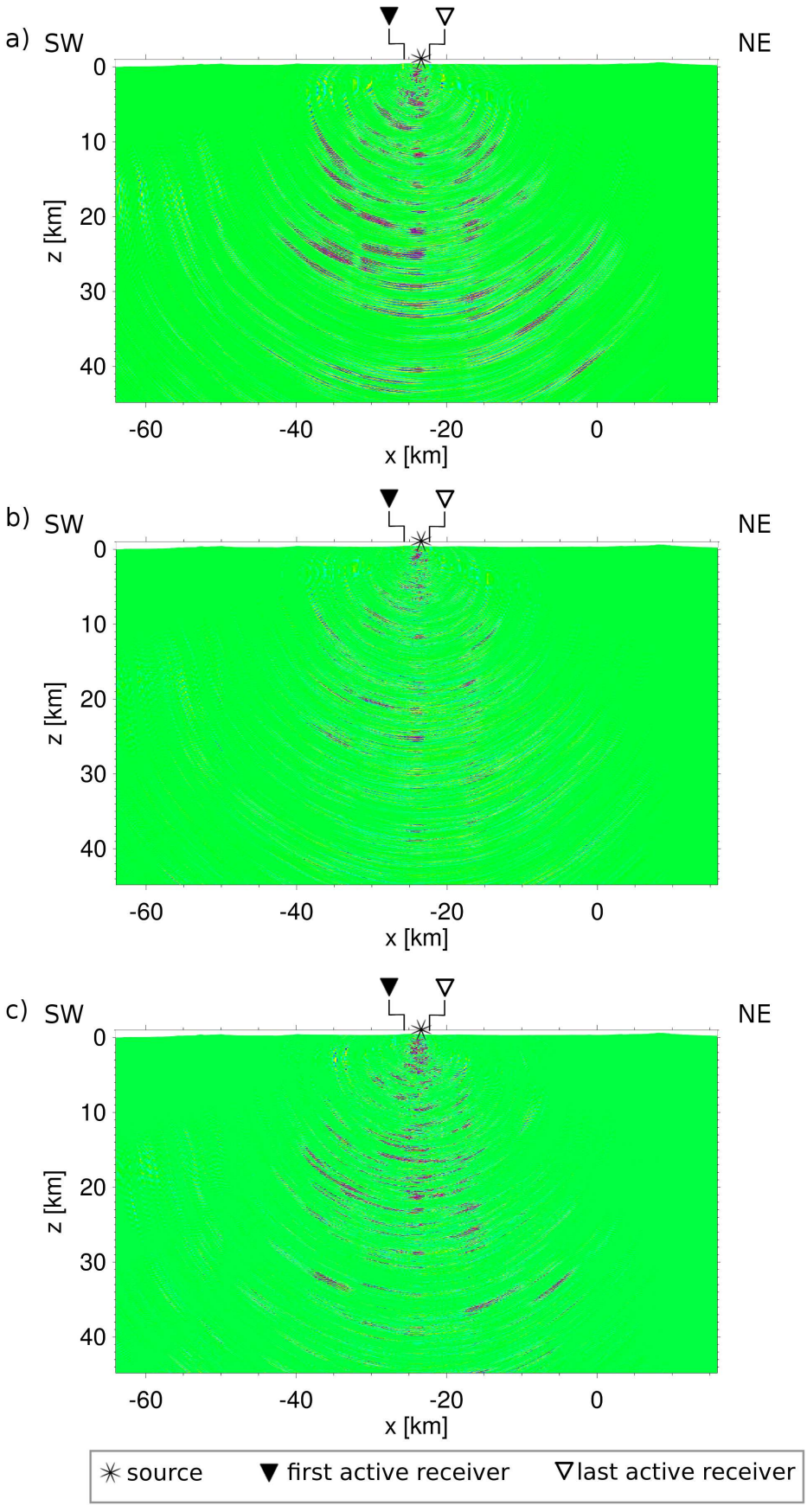
a)
SW
NE
0
10
20
30
40
z [km]
-60
-40
-20
0
x [km]
b)
SW
NE
0
10
20
30
40
z [km]
-60
-40
-20
0
x [km]
c)
SW
NE
0
10
20
30
40
z [km]
-60
-40
-20
0
x [km]
source
first active receiver
last active receiver

5 Reflection Seismic Images along Line SJ-6

The following sections present the results of Kirchhoff Prestack Depth migration, Fresnel Volume migration and Reflection Image Spectroscopy, respectively.
Firstly, the results for the southwestern SJ-6 line segment are presented and discussed in section 5.1 followed by the results for the eastern SJ-6 line segment in section 5.2. The preprocessed single shot gathers that are related to each of the two receiver line segments are all migrated separately and stacked afterwards. The Kirchhoff Prestack Depth migrated sections are clipped before stacking, taking into account the extent of the receiver spreads of each shot gather. The stacked values are divided by the number of non-zero values that contribute to the sum at each particular grid node in order to improve the signal-to noise ratio especially in the shallow regions where data coverage is low due to the short offsets. Equivalent clipping is not necessary for the Fresnel Volume migrated depth sections as the local restriction of the migration operator significantly reduces the amount of migration noise that previously superimposed the actual reflection signal. The stacked depth sections are adjusted to the geometry of line SJ-6 in order to obtain a 2D depth section that displays the reflectivity structure directly from beneath the profile line. Finally, the 2D sections are laterally normalized in order to account for lateral amplitude differences within the sections. The term reflectivity will be used in the following to describe the intensity of the imaged structures. High reflectivities are indicated by red colours and low reflectivities by green and blue colours, respectively.
Each section starts with an overview on the results of the three migration approaches in order to introduce the main structural features beneath the individual line segments and to further evaluate and compare the different results. After this follows a more detailed description of particular line segments that are subdivided according to the prominent pre-existing geomorphological units.

5.1 Southwestern line segment

Figure 5.1 illustrates the final depth sections obtained by Kirchhoff Prestack Depth migration, Fresnel Volume migration and Reflection Image Spectroscopy along the southwestern segment of line SJ-6, respectively,. The course of the respective receiver line segment is illustrated in Figure 5.1 a). Figure 5.1 b) represents the Kirchhoff Prestack Depth migration depth section and c) the Fresnel Volume migration image. The narrow-frequency band images obtained by Reflection Image Spectroscopy are presented in Figure 5.1 d) - f). The profile starts at the Pacific Coast near Morro Bay and extents towards northeast crossing the western Franciscan Block that is juxtaposed against rocks of the Salinian Block by the Nacimiento fault at approximately x = -49 km. The Rinconada fault is located at approximately x = -37 km along the profile line. The San Andreas fault zone separates the Salinian Block from rocks of the eastern Franciscan Block at $x = 0$ km.
The most prominent feature in the depth sections along the southwestern line segment is a bunch of very strong reflectors in the lower crust beneath the Salinian Block. High reflectivities and the appearence of distinct reflectors is limited to the central part of the Kirchhoff Prestack Depth image. The background migration noise level is extremely high southwest to the Nacimiento fault as well as northeast to the San Andreas fault so that structural details there can not be precisely observed. The Fresnel Volume depth section shows a clearly improved image that reveales additional details of the crustal structure compared to the Kirchhoff Prestack Depth image. Distinct reflectors are clearly visible over the full range of the profile line and migration noise is significantly suppressed.
The depth sections obtained by Reflection Image Spectroscopy again improve the image quality because additional structural details are observable in each of the three narrow-frequency images that are not evident in the full-frequency range image.

Figure 5.1: *a) Map view of the southwestern SJ-6 receiver line segment. b) Kirchhoff Prestack Depth image, c) respective Fresnel Volume image, d) Reflection Image Spectroscopy low-frequency image (10-15 Hz), e) intermediate-frequency image (15-20 Hz) and f) high-frequency image (20-25 Hz), respectively, of the same region.*

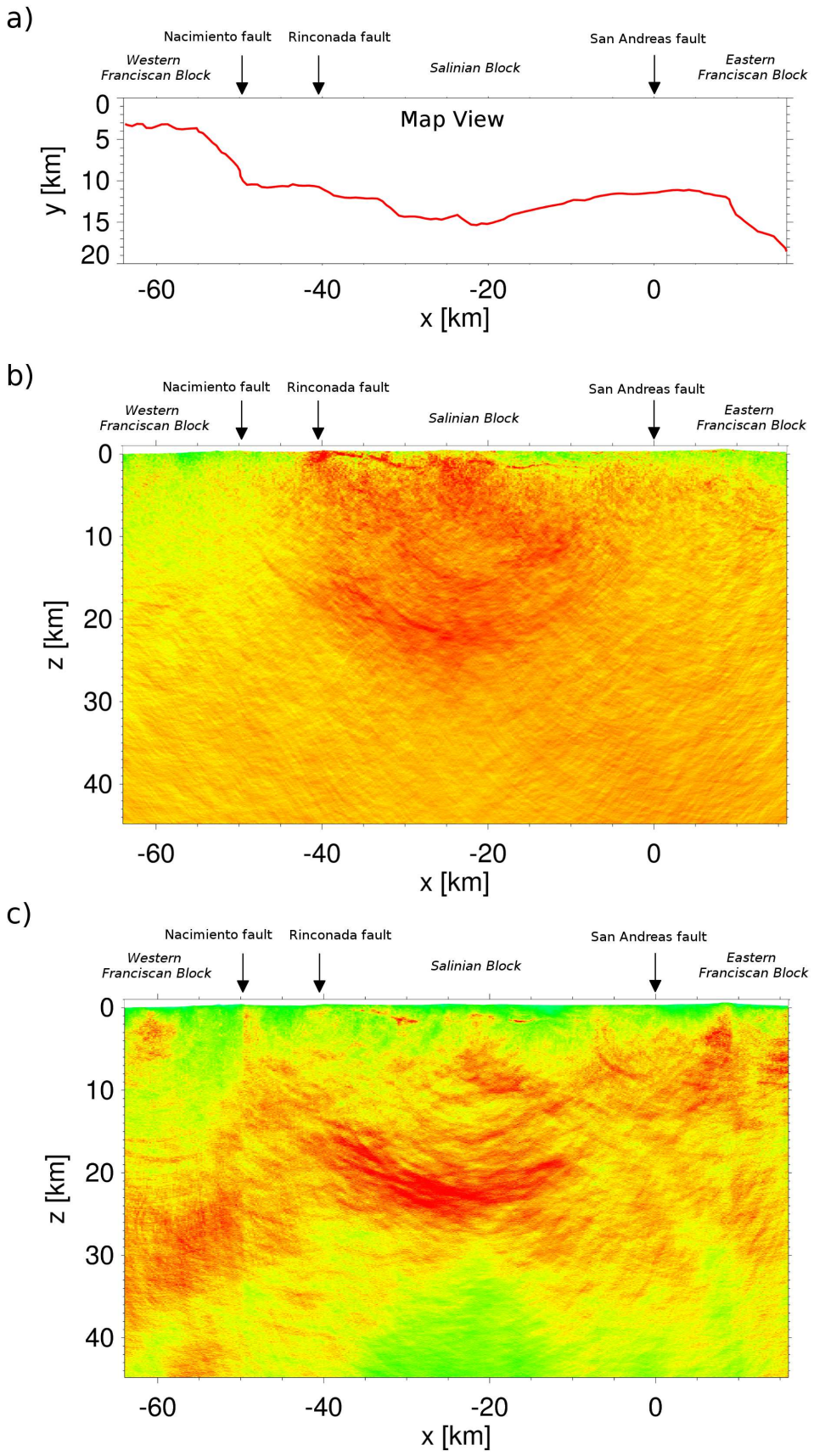
a)
Nacimiento fault
Rinconada fault
San Andreas fault
Western Franciscan Block
Salinian Block
Eastern Franciscan Block
Map View
y [km]
0
5
10
15
20
-60
-40
-20
0
x [km]
b)
Nacimiento fault
Rinconada fault
San Andreas fault
Western Franciscan Block
Salinian Block
Eastern Franciscan Block
z [km]
0
10
20
30
40
-60
-40
-20
0
x [km]
c)
Nacimiento fault
Rinconada fault
San Andreas fault
Western Franciscan Block
Salinian Block
Eastern Franciscan Block
z [km]
0
10
20
30
40
-60
-40
-20
0
x [km]

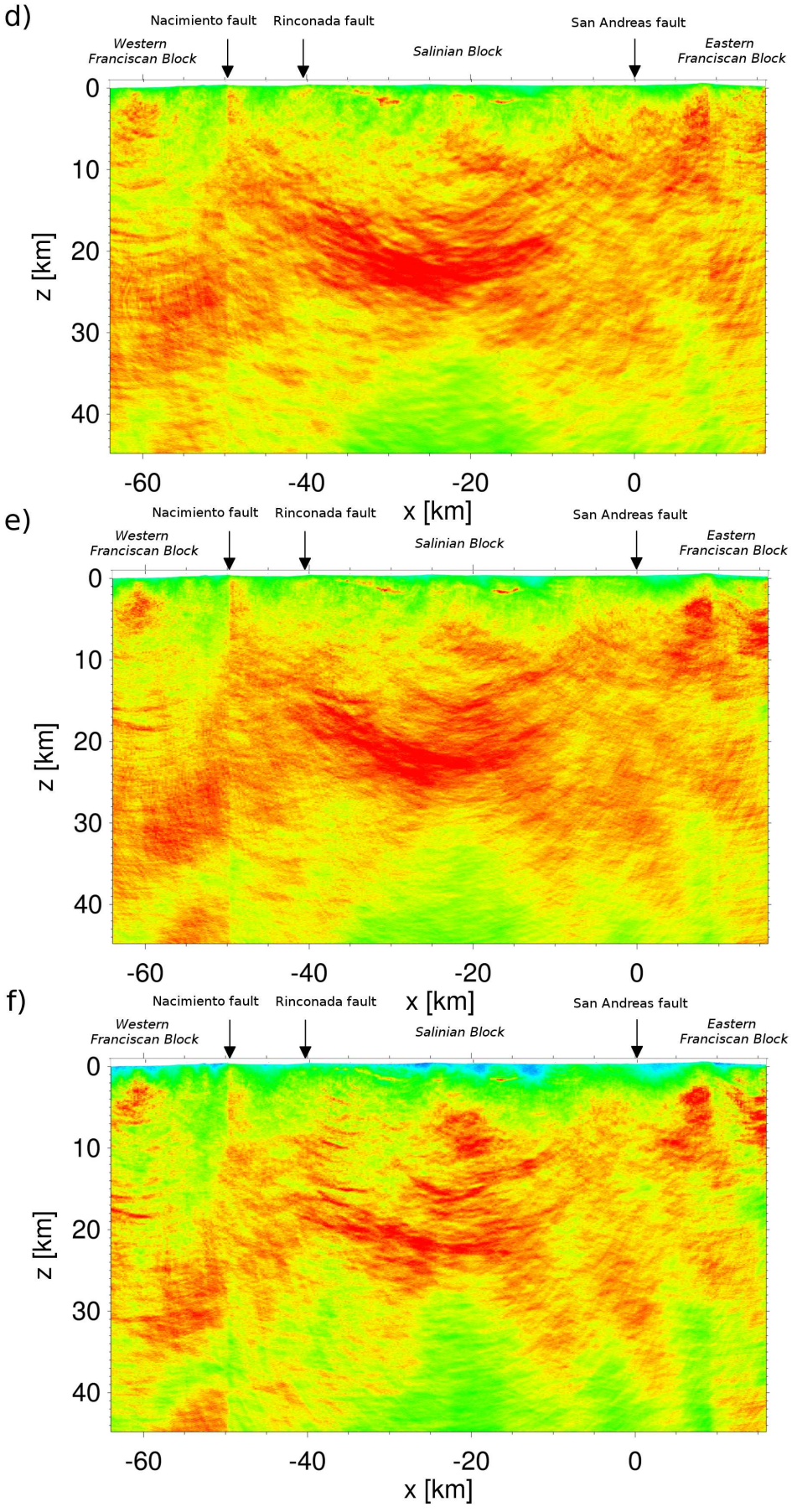

Figure 5.1: *(continued)*

5.1.1 Western Franciscan Block

The western Franciscan Block is located along the southwesternmost section of the profile line. Towards northeast it is bordered by the Nacimiento fault against granitic and metamorphic rocks of the allochthonous Salinian Block. The Nacimiento fault zone is located approximately at x = -49 km. Figure 5.2 and Figure 5.3 depict enlargements of the first 20 km of the SJ-6 profile line that crosses the western Franciscan Block. Distinctive structures are hardly visible in the Kirchhoff Prestack Depth image in Figure 5.2 a). Between depths of 16 km and 21 km three subhorizontal reflectors (A, B and C) can be recognized between the southwestern image margin and x = -55 km. The rest of the image is significantly influenced by migration noise.

The respective Fresnel Volume image presented in Figure 5.2 b) as well as the narrow frequency band images obtained by Reflection Image Spectroscopy in Figure 5.3 a)-c) depict more distinctive features through the entire crust and the uppermost mantle, especially along the relatively straight line segment at the southwestern margin of the depth section. A considerable change in image quality characterizes the Fresnel Volume full- and narrow-frequency images by decreased reflectivity from x = -57 km towards northeast. This is an effect of the strong bend in the profile line between x = -55 km and -50 km

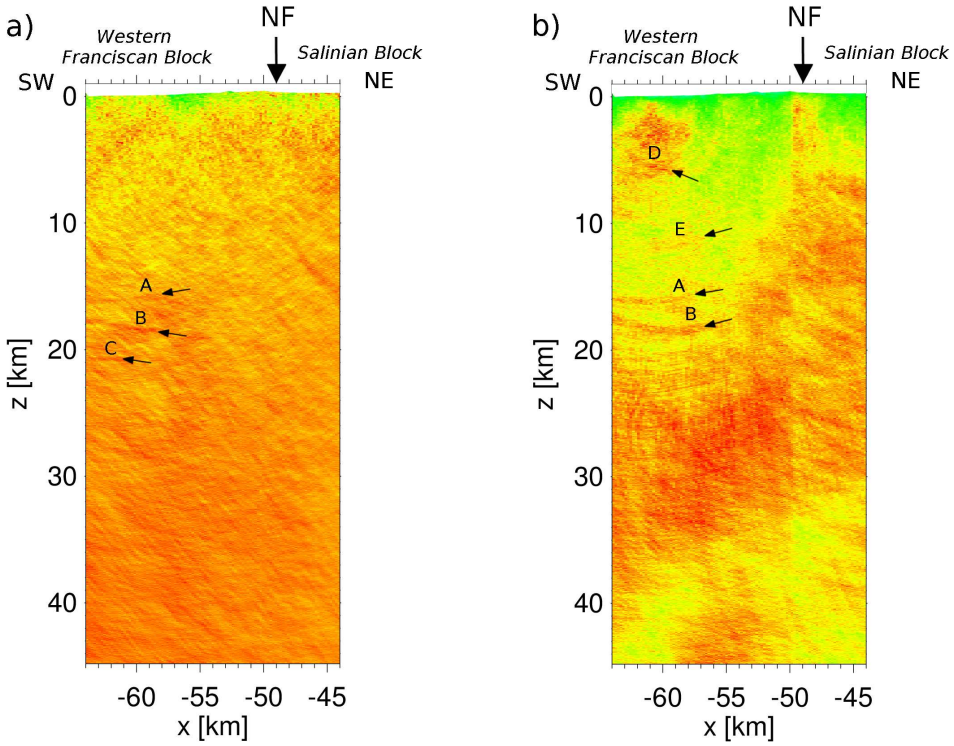

Figure 5.2: *Kirchhoff Prestack Depth image (a) and Fresnel Volume image (b) of the western Franciscan Block between x = -64 km and -44 km. NF- Nacimiento fault.*

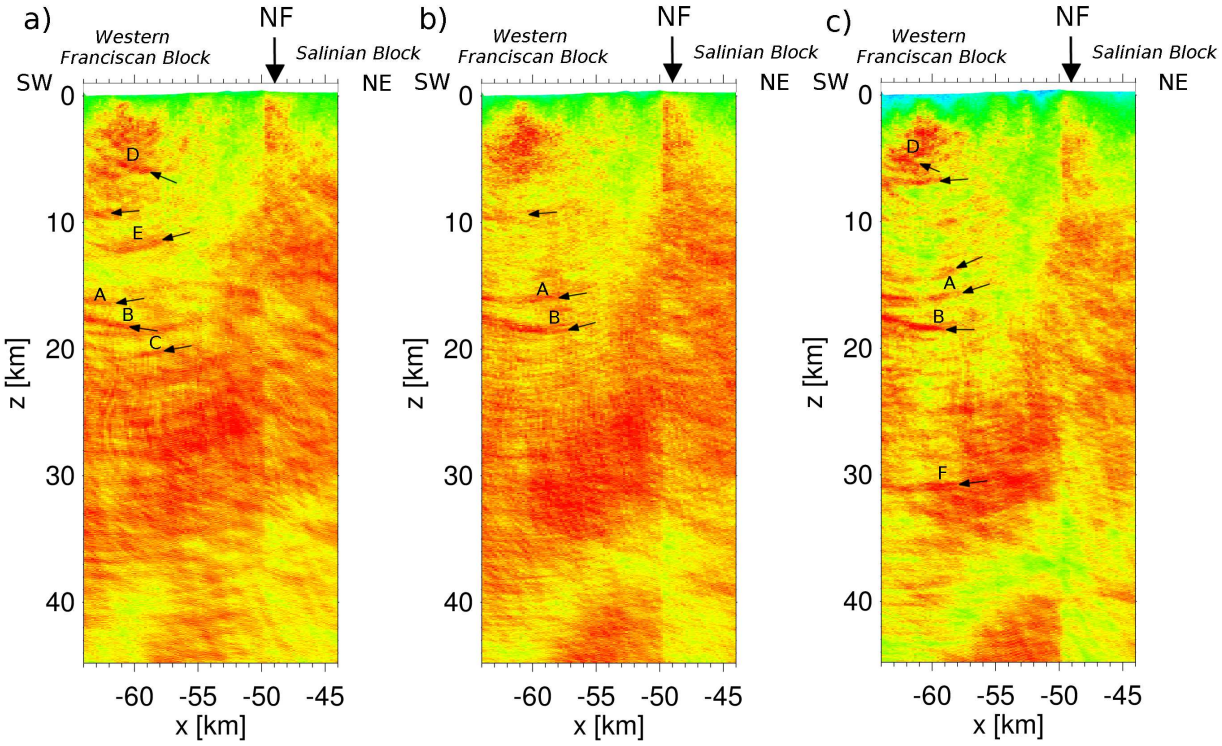

Figure 5.3: *Reflection Image Spectroscopy images of the western Franciscan Block between x = -64 km and -44 km. a) low-frequency image (10-15 Hz), b) intermediate-frequency image (15-20 Hz) and c) high-frequency image (20-25 Hz), respectively. NF- Nacimiento fault.*

that is likely to cause the absence of coherent reflection signals. In addition to that, the data fold is comparatively low along this line segment because shots have been skipped during the acquisition process due to inaccessable regions along this particular part of the profile line (compare to Figure 4.10 in section 4.3.4). Figure 5.2 b) depicts a zone of high reflectivity in the shallow subsurface down to 5 km depth between the southwestern image margin and x = -57 km. Single continuous reflectors can hardly be distinguished in this zone in any of the narrow-frequency Fresnel Volume images of Figure 5.3.

At the bottom of this heterogeneous zone between 4 km and 6 km depth an indistinct northeast dipping reflector (D) can be observed in Figure 5.2 b). The latter appears very strong in the low-frequency image, disappears in the intermediate-frequency image and reappears slightly in the high-frequency image again.

The full-frequency image Figure 5.2 b) lacks of distinctive features between 6 km and 16 km depth. The narrow-frequency range images otherwise expose several details from this depth range. A strong slightly southwest dipping reflector (E) is clearly visible in the low-frequency image at 12 km depth. It can be supposed that scattering of high frequency components in the heterogeneous rocks of the Franciscan Complex might suppress this

structure in the intermediate- and high-frequency images. Reflector E reappears with less clear shape in the full-frequency image. The two distinct reflectors at 16 km depth and at 18 km depth (A and B) that can be observed in the Kirchhoff Prestack Depth image appear weak in the full-frequency Fresnel Volume image but are stronger in the narrow-frequency images. Reflector B shows a northeast dip component in the low- and in the high-frequency image, respectively. Additional details of the deeper parts of the depth sections can be observed in the high-frequency image. There, some weak and indistinct subhorizontal structures are visible between 22 km and 25 km depth and a strong reflector (F) is visible at 31 km depth.

Most of the structures in the western Franciscan Block are subhorizontal, some with a slight southwest dip component. Unfortunately, the data do not reveal any structural information on the Nacimiento fault in particular. However, the predominating orientation of the imaged structures significantly changes at the Nacimiento fault zone from almost horizontal in the Western Franciscan Block to predominantly northeast in the adjacent Salinian Block.

5.1.2 Salinian Block

The Salinian Block is located between the Nacimiento fault zone at x = -49 km and the San Andreas fault zone at x = 0 km. Figure 5.4 depicts enlargements of a) the Kirchhoff Prestack Depth image, b) the Fresnel Volume image. Figure 5.5 shows the narrow-frequency band images.

Subhorizontal reflectors (A) can be observed in the shallow subsurface in all depth sections down to 2 km depth. They appear most continuous in the Kirchhoff Prestack Depth image but less continous in the Fresnel Volume images. No distinct feature can be attributed to the Rinconada fault zone 8 km northeast to the Nacimiento fault. However, the image quality changes across the Rinconada fault as structures towards northeast to the fault appear stronger and more distinctive, especially in the shallow subsurface. The crust between 3 km and 13 km depth northeast to the Rinconada fault can be laterally subdivided into two regions. Between x = -40 km and -22 km the Kirchhoff Prestack Depth image depicts few northeast dipping reflectors (B) that are hardly distinguishable from the background migration noise. This zone appears quite non-reflective in the full-frequency Fresnel Volume image as well as in the low- and the intermediate-frequency image. The high-frequency image in contrast to this clearly confirms the indistinct structures from the Kirchhoff Prestack Depth image as they appear as strong and distinct northeast dipping reflectors. Towards southwest between x = -22 km and -13 km a zone of indistinct but relatively high reflectivity (C) is visible in the Kirchhoff Prestack Depth image between

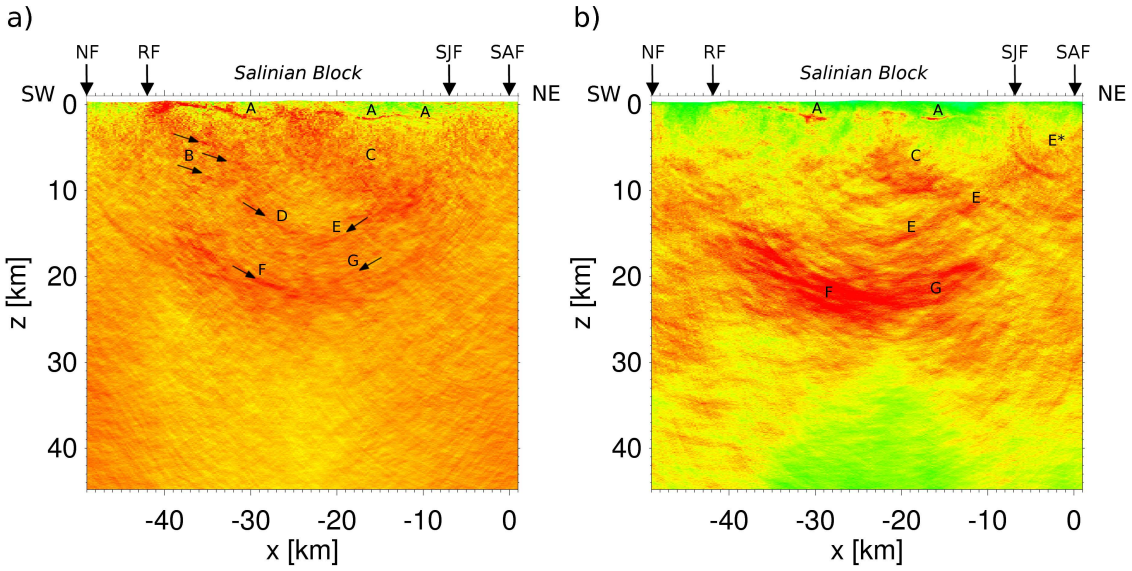

Figure 5.4: *Kirchhoff Prestack Depth image (a) and Fresnel Volume image (b) of the Salinian Block between x = -49 km and 1 km. NF- Nacimiento fault, RF - Rinconada fault, SJF - San Juan fault, SAF- San Andreas fault.*

3 km and 10 km depth. This zone is emphasized in the Fresnel Volume image and the narrow-frequency images, in particular in the high-frequency image. Indistinct structures with a slight southwest dip component can be recognized. At the bottom of this zone at 10 km depth a strong and distinct reflector is clearly visible. At approximately x = -22 km the reflection character changes towards northwest from weak reflectivities to stronger reflectivities in the upper 13 km. This lateral change in reflection character correlates with a change of the predominating orientation of the imaged structures from northeast to southwest.

The Kirchhoff Prestack Depth image shows a distinct northeast dipping reflector (D) that can be traced down from 10 km depth to 14 km depth between x = -32 km and -22 km. There it merges to indistinct southwest dipping structures (E) that can be traced upwards towards northeast to approximately 8 km depth where it is intersected by a very strong northeast dipping reflector. Above the intersecting reflector, reflector E can hardly be traced as E* in the full-frequency Fresnel Volume image. Whereas the northeast dipping reflector D appears rather indistinct in the corresponding Fresnel Volume images the southwest dipping structures E are strongly emphasized. The high-frequency image shows reflector D and E as separate distinctive structures that seem to be thrust upon each other.

The most prominent feature in the Salinian Block is located in the lower crust. It is

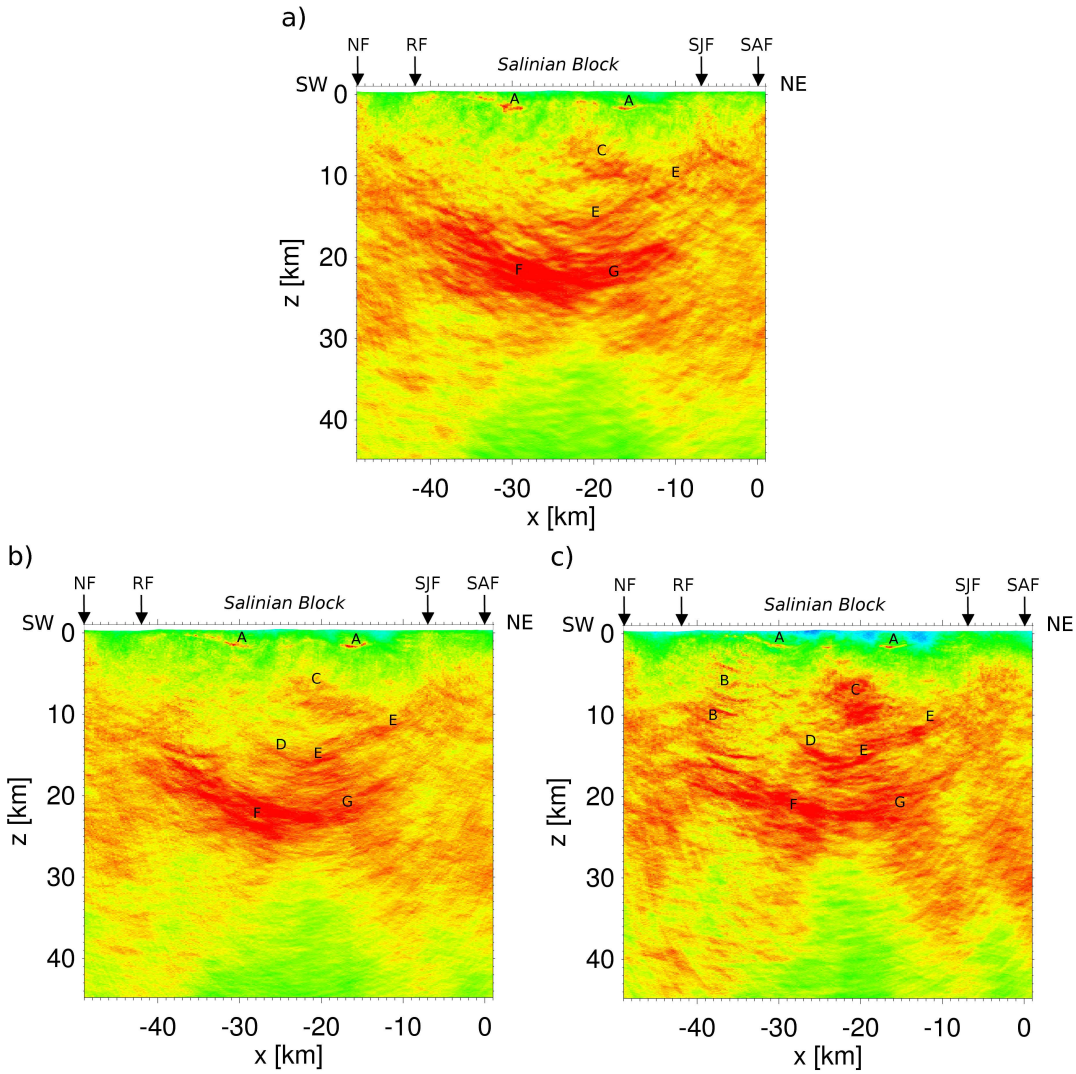

Figure 5.5: *Reflection image spectroscopy images of the Salinian Block between x = -49 km and -1 km. a) low-frequency image (10-15 Hz), b) intermediate-frequency image (15-20 Hz) and c) high-frequency image (20-25 Hz), respectively. NF- Nacimiento fault, RF - Rinconada fault, SJF - San Juan fault, SAF- San Andreas fault.*

characterized by strong subparallel reflectors between x = -40 km and -10 km (F and G). The Kirchhoff Prestack Depth image depicts only few single distinct northeast dipping reflectors southwest to x = -22 km and few slighly southwest dipping reflectors farther northeast. The Fresnel Volume image in contrast shows a cluster of very strong nearly subparallel northeast dipping reflectors. This cluster has a width of approximately 5 km and can be observed at depths between 15 km and 26 km. From x = -22 km towards northeast the predominating dip of this cluster changes from northeast to southwest. The northeastern of these strong lower crustal reflectors (G) abruptly disappears at x = -10 km. The region below these strong reflectors appears seismically transparent.

5.1.3 San Andreas Fault

Figure 5.6 and Figure 5.7 show the northeastern portion of the southwestern line segment that crosses the San Andreas fault surface trace perpendicular to its predominating strike. The San Andreas surface trace is located at $x = 0$ km. There, rocks of the Salinian Block are supposed to be juxtaposed against rocks of the eastern Franciscan Block. The today inactive San Juan fault (SFJ) is located approximately 7 km southwest to the San Andreas fault zone.

The Kirchhoff Prestack Depth image in Figure 5.6 a) contains little structural information on the subsurface. Southwest of the San Juan fault distinctive subhorizontal reflectors (A) appear in the upper 2 km. These features are less distinctive and hardly visible in the full-frequency Fresnel Volume image (Figure 5.6 b) and the narrow-frequency images (Figure 5.7 a) - c)). The Fresnel Volume image depicts more structural details from beneath and adjacent to the San Andreas fault zone compared to the Kirchhoff Prestack Depth image.

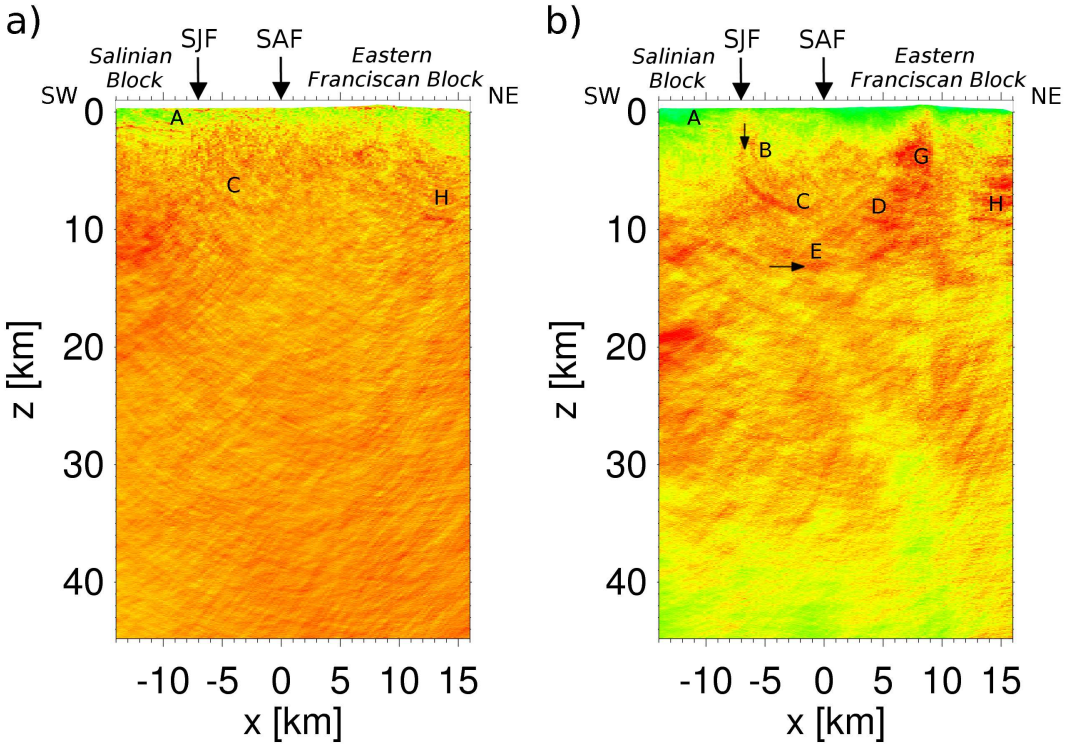

Figure 5.6: *Kirchhoff Prestack Depth image (a) and Fresnel Volume image (b) across the San Andreas fault zone between x = -14 km and 16 km. SJF - San Juan fault, SAF- San Andreas fault.*

Beneath the San Juan fault surface trace an indistinct subvertical structure (B) can be traced down to 5 km depth. There it turns into a northeast directed strong reflector (C) that is bended towards the surface. This reflector becomes indistinct in the intermediate-frequency image and can not be observed in the high-frequency image. Where it is visible, the reflector abruptly terminates when it approaches the San Andreas fault at $x = 0$ km. The latter can be characterized as a zone that lacks of coherent reflections. The San Andreas fault zone can therfore be specified as 4 km wide zone between $x = 0$ km and 4 km. At $x = 4$ km reflector C seems to reappear (reflector D in Figure 5.6 b)) and reflectivities are increased compared to those from within the fault zone. The 4 km wide fault zone can be traced to approximately 13 km depth.

There, a very indistinct subhorizontal structure (E) is visible within the fault zone between $x =$ -2 km and 1 km. The lower crust beneath 13 km depth does not reveal any distinct reflectors towards northeast from $x =$ -10 km where the strong lower crustal reflectors of the Salinian Block abruptly terminate. A similar change in reflectivity character can not be observed in the lower crust towards northeast. The high frequency-image depicts some very short but rather distinct subparallel reflectors (F) directly below the San Andreas fault surface trace between depths of 23 and 30 km. These reflectors have a very slight southwest dipping component.

Northeast to the San Andreas fault distinct reflectors can be observed from the surface downwards to 13 km depth. Between $x = 5$ km and 10 km slightly southwest dipping reflectors are visible (G). The strong bend in the profile line from $x = 9$ km towards northeast causes a significant decrease of reflectivity values. At the northeastern image margin distinct subhorizontal reflectors (H) are visible at depth between 4 km and 10 km. The intermediate-frequency range image shows slight northeast dipping reflectors (I) that seem to connect the reflectors directly northeast to the San Andreas fault with those at the image margin.

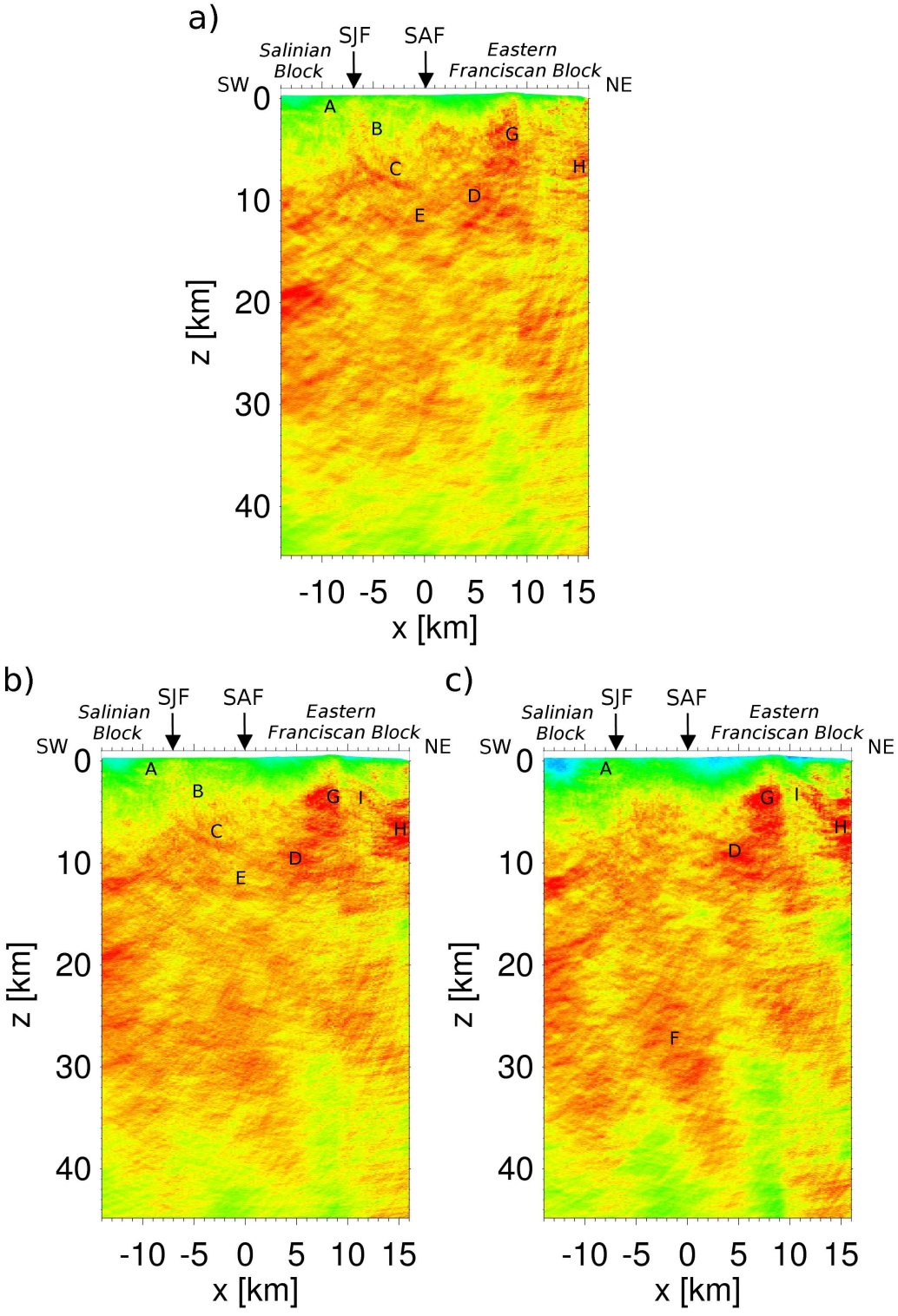

Figure 5.7: *a) Reflection Image Spectroscopy images across the San Andreas fault zone between $x = -14$ km and 16 km. a) low-frequency image (10-15 Hz), b) intermediate-frequency image (15-20 Hz) and c) high-frequency image (20-25 Hz), respectively, of the same region. SJF - San Juan fault, SAF- San Andreas fault.*

5.2 Eastern line segment

Figure 5.8 illustrates the final depth sections along the eastern SJ-6 line segment. In accordance to section 5.1 Figure 5.8 a) illustrates the course of the respective receiver line segment in map view. The migration results are presented in Figure 5.8 b) for Kirchhoff Prestack Depth migration, Figure 5.8 c) for full-frequency Fresnel Volume migration and finally Figures 5.8 d)-f) for the narrow-frequency band images determined by Reflection Image Spectroscopy. Note that the perspective changes to west-east compared to the southwestern line segment. The eastern SJ-6 profile segment crosses the Eastern Coast Ranges including the San Andreas fault zone and the Great Valley , the eastern Franciscan Block as well as parts of the Sierra Nevada foothills. Both, the Kirchhoff Prestack Depth image as well as the Fresnel Volume image depict most of the prominent structures. The migration background noise level is significantly higher in the Kichhoff Prestack Depth image that consequently reduces the image quality compared to the Fresnel Volume full- and narrow-frequency images.

Reflectivities in the Eastern Franciscan Block appear obscured and less distinctive compared to the structures beneath the San Joaquin Valley to the east. The upper crust beneath the San Joaquin Valley consists of west dipping sequentially layered reflectors that are folded in the basin syncline at the western border of the Valley. Beneath these sequences of reflectors, steeper west dipping reflectors can be observed in the Kirchhoff Prestack Depth image that are more clearly resolved in the Fresnel Volume image. Each of the narrow-frequency images from Reflection Image Spectroscopy shows additional structural details compared to the full-frequency range Fresnel Volume image.

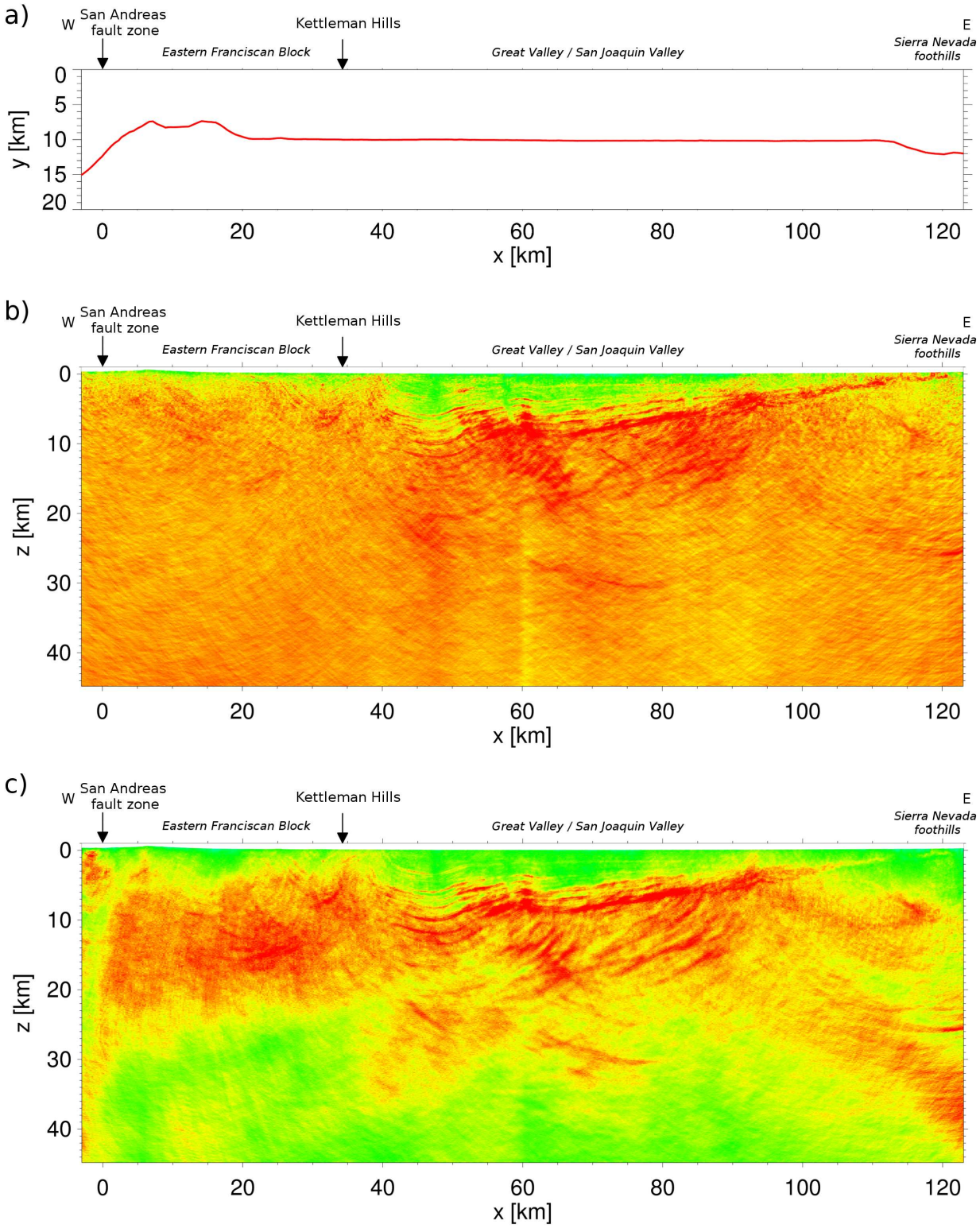

Figure 5.8: *a) Map view of the eastern SJ-6 receiver line segment. b) Kirchhoff Prestack Depth image, c) respective Fresnel Volume image, d) Reflection Image Spectroscopy low-frequency image (10-15 Hz), e) intermediate-frequency image (15-20 Hz) and f) high-frequency image (20-25 Hz), respectively, of the same region.*

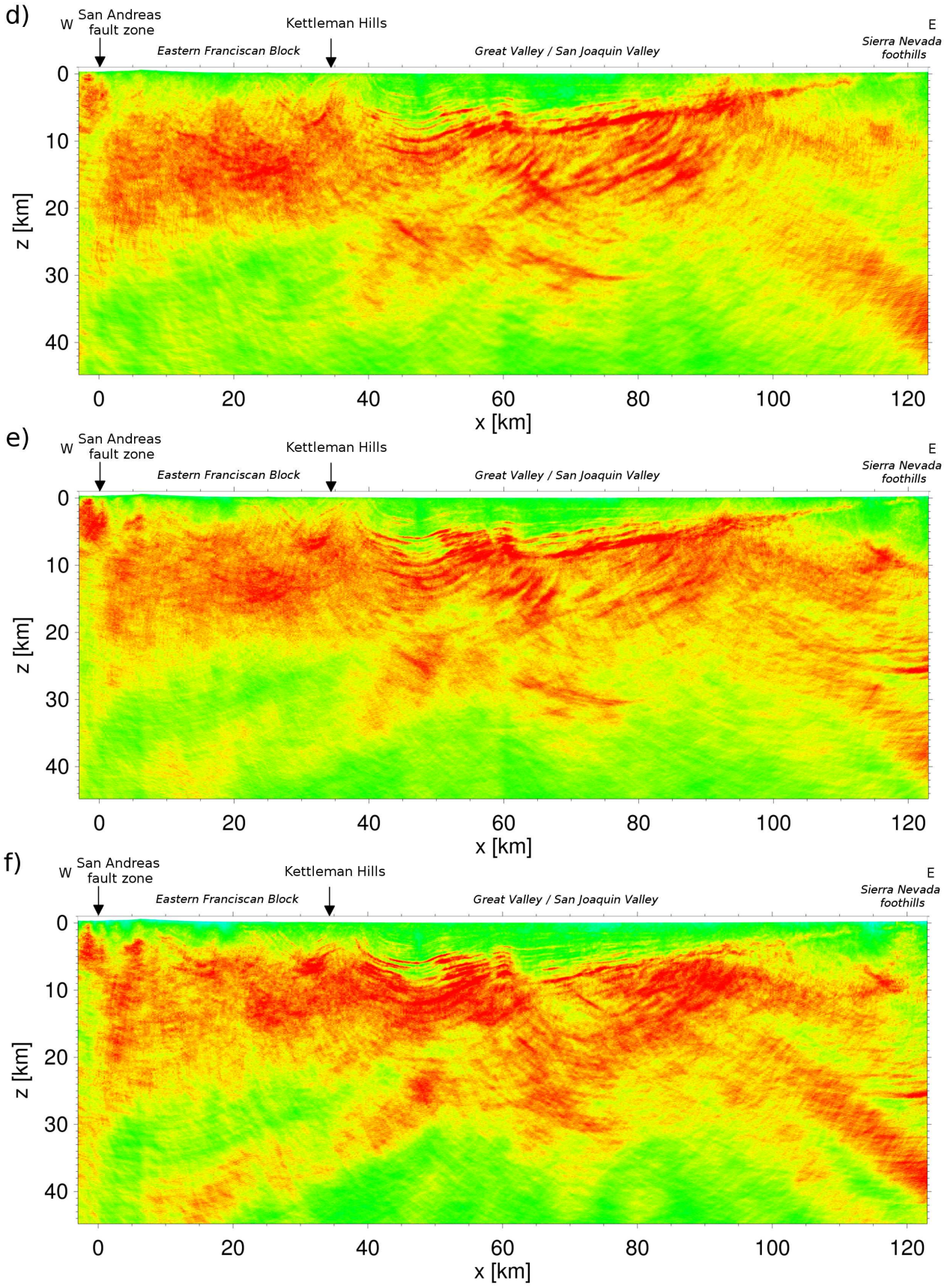

Figure 5.8: *(continued)*

5.2.1 Eastern Franciscan Block

The eastern Franciscan Block is located northeast to the San Andreas fault zone. A detailed view of the corresponding Kirchhoff Prestack Depth image and the Fresnel Volume image is shown in Figure 5.9 a) and b). The narrow-frequency images are presented in Figure 5.10 a)-c), respectively.

The San Andreas fault zone reappears as a non-reflective zone. However, this zone is not straight in depth but dips towards west in this perspective. The latter can be clearly observed in the Fresnel Volume images showing a sharp reflectivity contrast to the surrounding subsurface. East to the San Andreas fault a west dipping reflector (A) reappears in all five images. It can also be identified in the images of the southwestern line segment. Further east, the Kirchhoff Prestack Depth image reveals three indistinct quasi subparallel east dipping reflectors (small black arrows) between x = 5 km and 18 km down to depths of 10 km. The latter are poorly resolved in the corresponding Fresnel Volume images except for the lowermost that appears strongest in the Fresnel Volume full-frequency image and the low-frequency image but disappears in the high-frequency image. Between x = 10 km and 28 km the Fresnel Volume images show a wedge shaped like structure directed towards east that can be distinguished by single distinct reflectors and higher

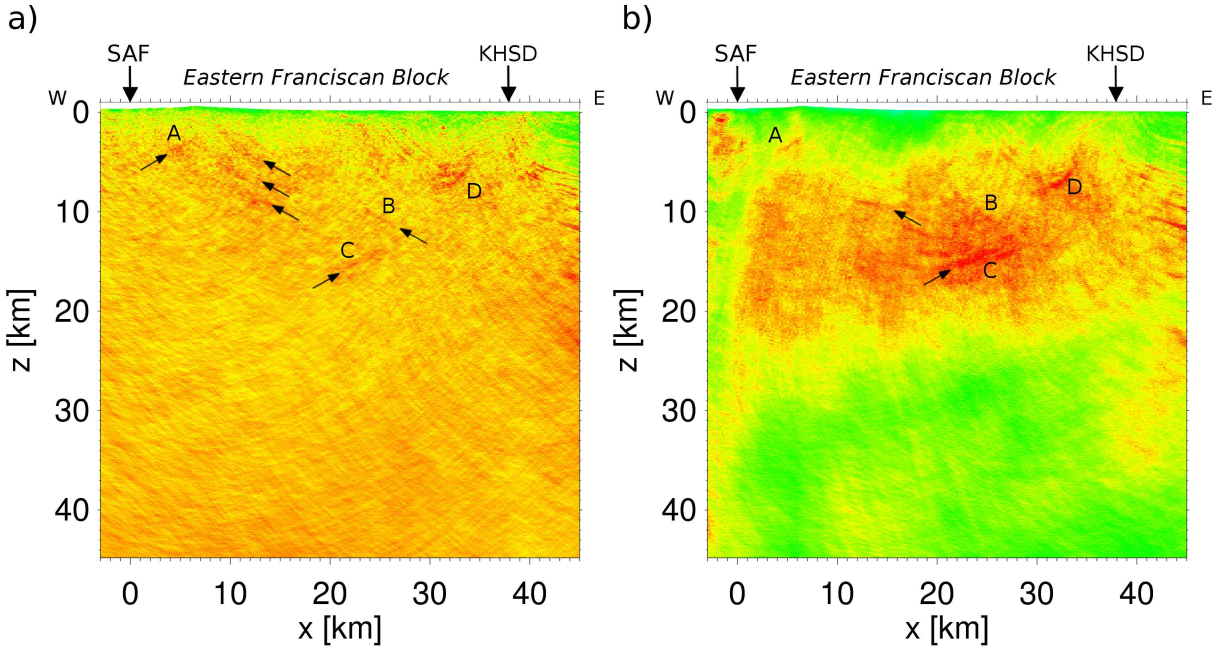

Figure 5.9: *Kirchhoff Prestack Depth image (a) and Fresnel Volume image (b) of the eastern Franciscan Block between x = -3 km and 45 km. SAF- San Andreas fault, KHSD - Kettleman Hills South Dome.*

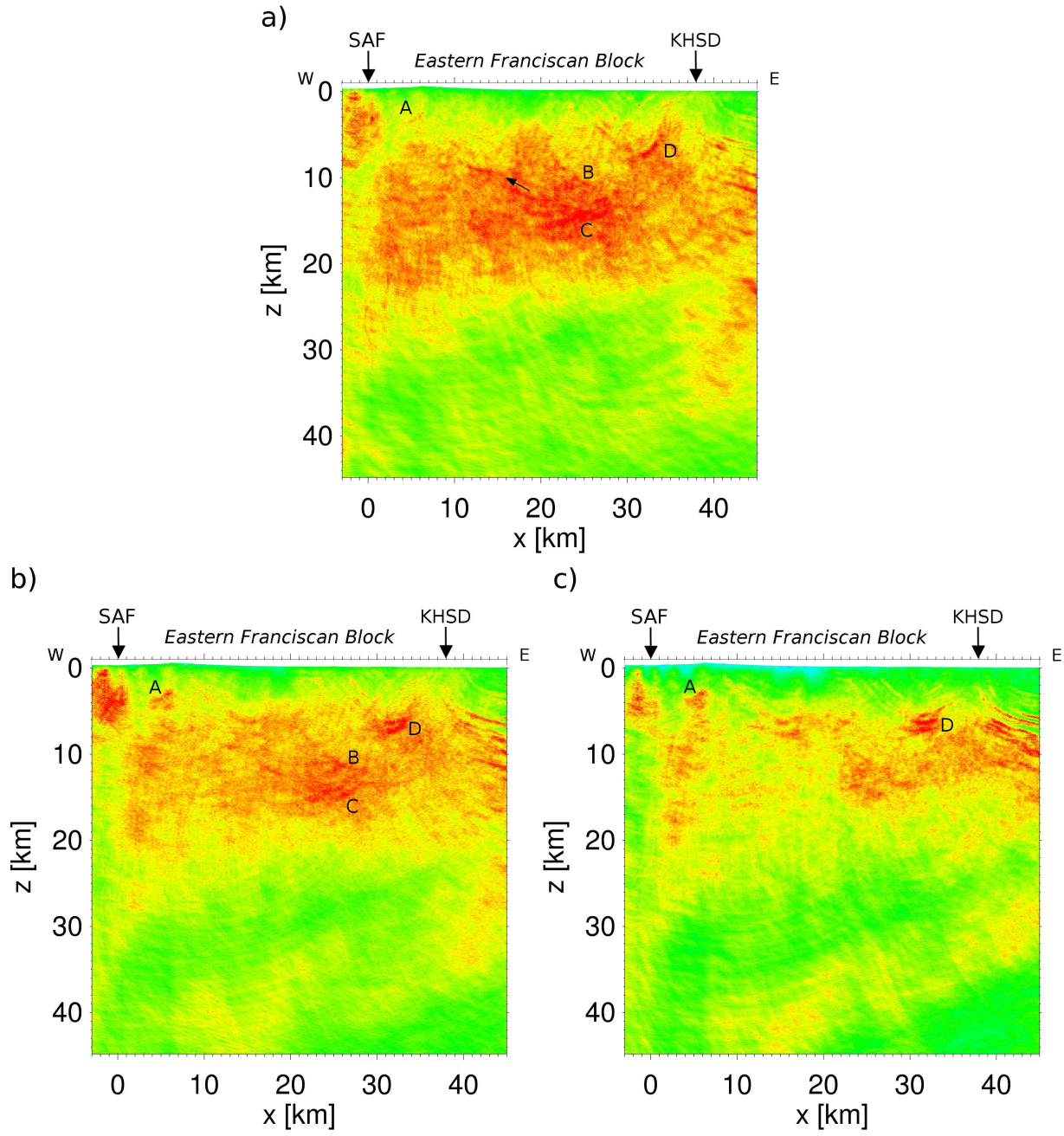

Figure 5.10: *Reflection Image Spectroscopy images of the eastern Franciscan Block between x = -3 km and 45 km. a) low-frequency image (10-15 Hz), b) intermediate-frequency image (15-20 Hz) and c) high-frequency image (20-25 Hz), respectively. SAF- San Andreas fault, KHSD - Kettleman Hills South Dome.*

reflectivities. It is well resolved in the full- and low-frequency image but poorly resolved in the high-frequency image. The Kirchhoff Prestack Depth image only depicts the outer shape of this structure by the east dipping reflector B and the west dipping reflector C. Above the wedge shaped structure each depth section contains a west dipping zone that

completely lacks of distinct reflectors spanning a width of aproximately 4 km between 5 and 15 km depth. Above and east to this zone the Kirchhoff Prestack Depth image shows very distinct subparallel reflector sequences that form a complete fold sequence in the upper 8 km. Three strong reflectors are visible at the base of the corresponding syncline from which the lowermost reflector (D) is discordant compared to the uppermost. These reflector sequences can be observed in the Fresnel Volume image but the reflectors do not appear that distinctive when compared to the Kirchhoff Prestack Depth image.
Both, the low-frequency as well as the intermediate-frequency image depict the west dipping reflector (D) that cuts discordantly through the west flank of the syncline.
Reflectivity is significantly reduced below 20 km depth.

5.2.2 Great Valley fore-arc basin

The depth sections along the easternmost segment of line SJ-6 across the San Joaquin Valley are displayed in Figure 5.11. The Kirchhoff Prestack Depth image in Figure 5.11 a) and the Fresnel Volume image in Figure 5.11 b) both illustrate the most strikingly features beneath the San Joaquin Valley. The difference is again the high background noise level in the Kirchhoff Prestack Depth image. The narrow-frequency images are shown in Figure 5.12 c) - e).
Subparallel west dipping reflector sequences (A) can be observed in the shallow crust from the easternmost image margin westward to the Great Valley syncline where they are folded down to depths of approximately 13 km. The shallowest of these reflectors (A*) appears most distinctive in the Kirchhoff Prestack Depth image . The lowermost of the above described reflectors appears very strong in all depth sections besides the high-frequency image. In the high-frequency image it is distinguishable but weak compared to the other depth sections.
Steeper west dipping reflectors (B) can be identified below the shallow reflector sequences beneath the center of the San Joaquin Valley. These structures are strongly emphasized in the full-frequency Fresnel Volume image and the low-frequency image down to depths of 20 km. The Kirchhoff Prestack Depth image contains a steeply east dipping reflector (C) at $x = 70$ km that cuts through the above described structures between 11 km and 14 km depth. This feature is not imaged by the Fresnel Volume image. Only the high-frequency image reveals this structure as well.
Lower crustal reflectors beneath the Great Valley can be observed in both, the Kirchhoff Prestack Deph image and the Fresnel Volume image, respectively. Beneath the Great Valley basin syncline between $x = 44$ km and 50 km a strong steeply east dipping reflector (D) can be observed at depths between 21 km and 25 km. Another slightly shallower east

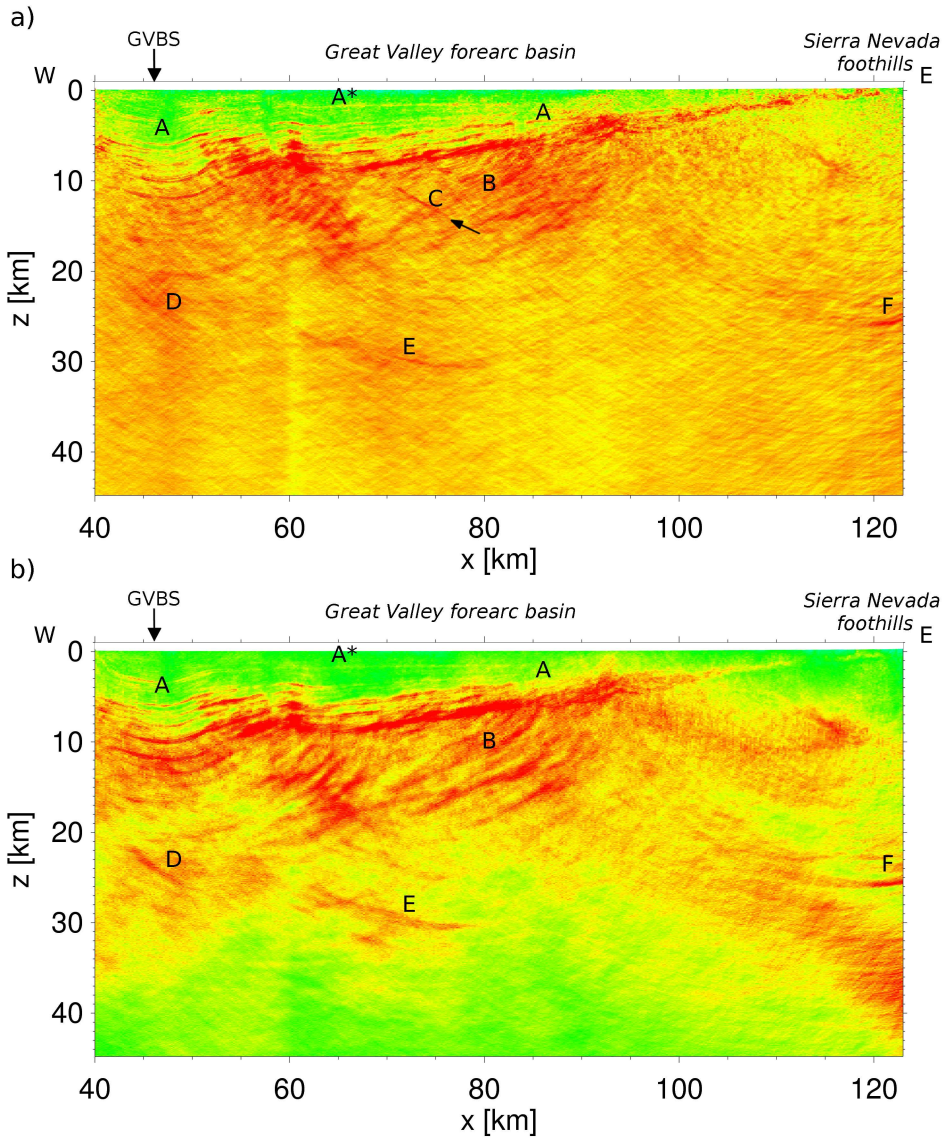

Figure 5.11: *a) Kirchhoff Prestack Depth image and b) Fresnel Volume image of the Great Valley between $x = 40$ km and 126 km. GVBS -Great Valley basin syncline.*

dipping reflector (E) appears farther east beneath the Great Valley between $x = 63$ km and 80 km. These reflectors do not appear in the high-frequency image.

At the eastern margin of the depth sections beneath the Sierra Nevada foothills a very strong subhorizontal reflector (F) is visible at 25 km depth. It is not imaged by the low-frequency data. The intermediate- and high-frequency images additionally reveal slight subhorizontal reflectors above reflector F.

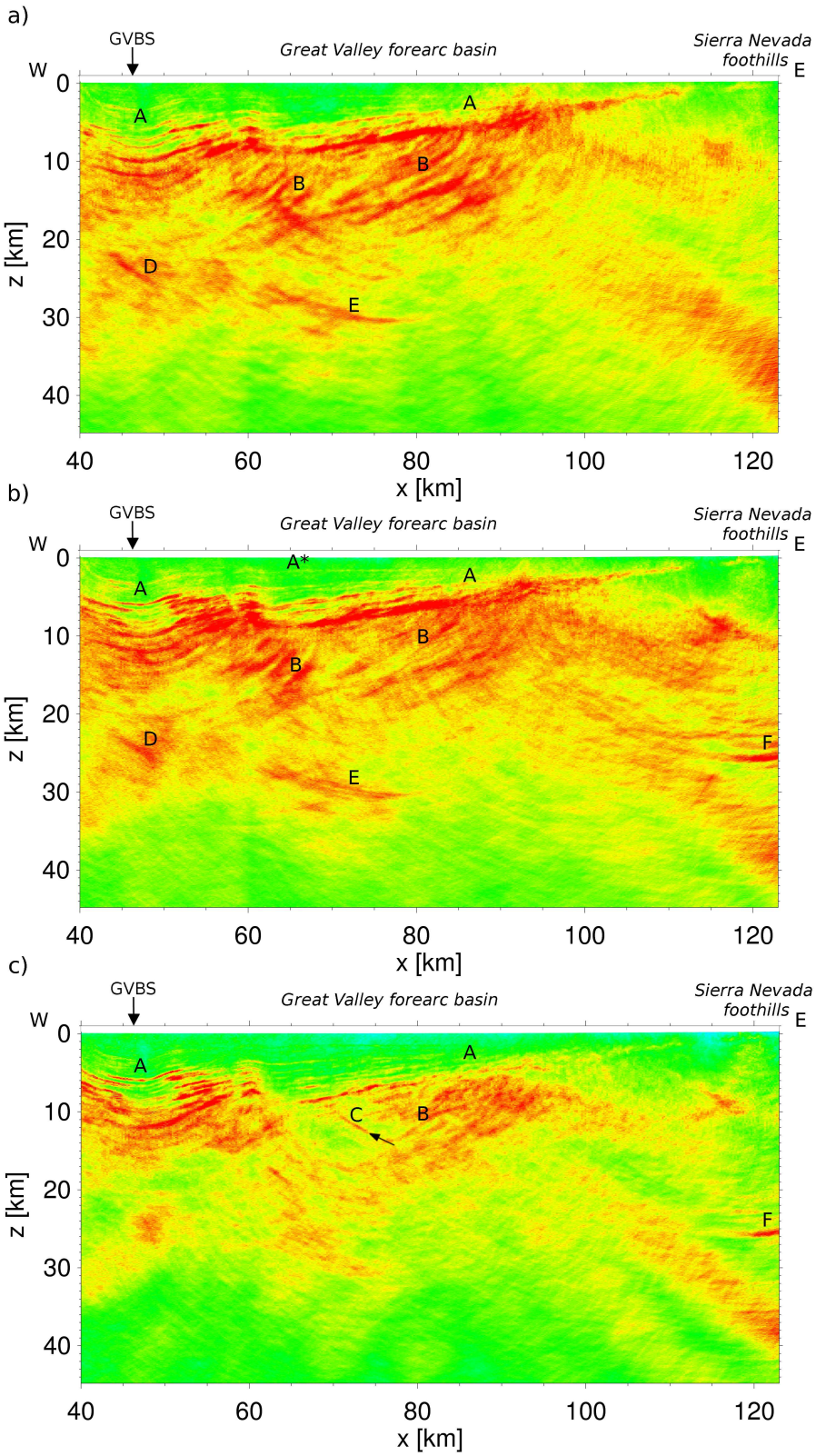

Figure 5.12: *Reflection Image Spectroscopy images of the Great Valley between $x = 40$ km and 126 km. a) low-frequency image (10-15 Hz), b) intermediate-frequency image (15-20 Hz) and c) high-frequency image (20-25 Hz), respectively. GVBS - Great Valley basin syncline.*

5.3 Impact of the velocity model

The prestack migration techniques as used in this work depend on a priori P-wave velocity information. To investigate the influence of the velocity information on the resulting depth images, Fresnel Volume migration is applied to the southwestern SJ-6 line segment using two different velocity models. The other migration input parameters remain equal for both migration processes. Beside the tomographic 3D velocity model (Thurber et al., 2006 and Lin et al., 2010) that has been used to migrated the SJ-6 data, the data are additionally migrated using the Southern California Earthquake Center Community Velocity Model CVM-H6.0 (Süss and Shaw, 2003). The CVM-H6.0 velocity information have been obtained from sonic logs and stacking velocity measurements from industry reflection profiles in Southern California. A depth slice through each velocity model along the southwestern SJ-6 line segment is illustrated in Figure 5.13 a) and b). The tomographic 3D velocity model is already introduced in section 4.3.2 and compared to the velocity information obtained from previous refraction data analysis along line SJ-6. Low-velocity zones and a smooth transition between lower crustal and mantle velocities are included into the model. The shallow subsurface consists of low velocities (2000 $\frac{m}{s}$) that rapidly increase with depth. The CVM-H6.0 model includes fast velocities in the shallow subsurface (4500 $\frac{m}{s}$) and increases not that rapidly with depth compared to the tomographic 3D velocity model. The crust-mantle transition is marked by an abrupt velocity increase from 6500 $\frac{m}{s}$ to approximately 8000 $\frac{m}{s}$. Low-velocity zones can not be identified in the CVM-H6.0 velocity model. The corresponding imaging results are shown in Figure 5.13 c) for the tomographic 3D velocity model and Figure 5.13 d) for the CVM-H6.0 model. The overall most significant structures, like the strong reflective lower crust as well as the prominent southwest dipping reflector southwest of the San Andreas fault are imaged in each of the depth sections. The depths of single structures slightly differ due to velocity differences. Shallow subsurface structures in the Salinian Block appear sharper and more distinct in the depth section obtained by the tomographic 3D velocity model. The San Andreas fault zone can be identified as a non-reflective zone within both depth sections. Consequently, the non-reflectivity from within the fault zone is caused by the reflection data itself and not by the low-velocity zone in the tomographic 3D velocity model. The relatively low velocities beneath 24 km in the tomographic 3D velocity model compared to the CVM-H6.0 velocity model cause higher reflectivities in the corresponding migrated section that will cause difficulties to locate the crust-mantle boundary from the reflection data while the clear velocity contrast in the CVM-H6.0 velocity model correlates with a clear contrast in the reflectivity character from high reflectivities above the velocity

contrast to low reflectivities beneath. All in all, the tomographic 3D velocity model provided by Thurber et al. (2006) and Lin et al. (2010) yields depth images of higher resolution. Nevertheless, the shape, the location and also the strength of the imaged structures depend on the accuracy of the velocity information.

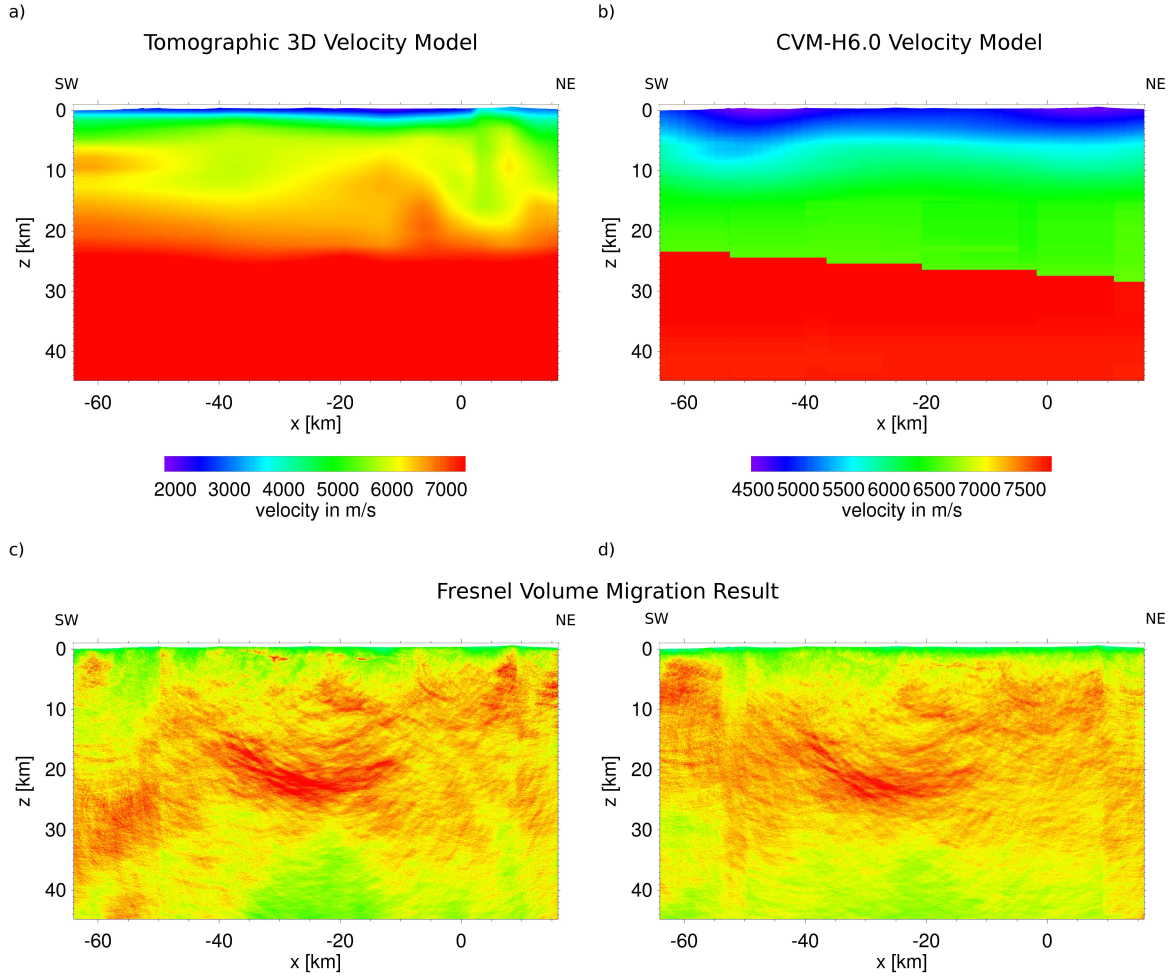

Figure 5.13: *Top: Depth slices through the a) tomographic 3D velocity model (Thurber et al., 2006 and Lin et al. (2010)) and b) CVM-H6.0 velocity model (Süss and Shaw, 2003). The depth slices are located along to the southwestern SJ-6 line segment. Bottom: Fresnel Volume migration results under consideration of c) the tomographic 3D velocity model and d) the CVM-H6.0 velocity model.*

5.4 One-sided images

The SJ-6 data have been recorded using a common split-spread geometry so that seismic signals are recorded from both sides of the source. The imaging results indicate a heterogeneous subsurface with particular zones of high reflectivities as well as reflectors of variable dips and sizes. Seismic signal responses from small-scale structures or steeply dipping structures are in some cases better resolved using data from only one side of the spread. Figure 5.14 shows a simple example of a steeply dipping reflector beneath a split-spread geometry. In Figure 5.14 a) where the reflector is close to the source the reflection response signal is only recorded by the receivers on the left hand side of the source. With increasing lateral distance of the reflector to the source as illustrated in Figure 5.14 b) a reflection response is recorded almost along the whole spread. The sampling density, however, is highest for signals recorded along the left hand side of the source and will therefor create a more precise image of the reflector. In order to enhance or even unmask steeply dipping structures as well as small-scale structures only traces from one side of the spread are considered for migration in the following. Figure 5.15 illustrates the Fresnel Volume migration depth sections of a) the full spread, b) the half spread southwest of the source and c) the half spread northeast of the source for the southwestern SJ-6 line

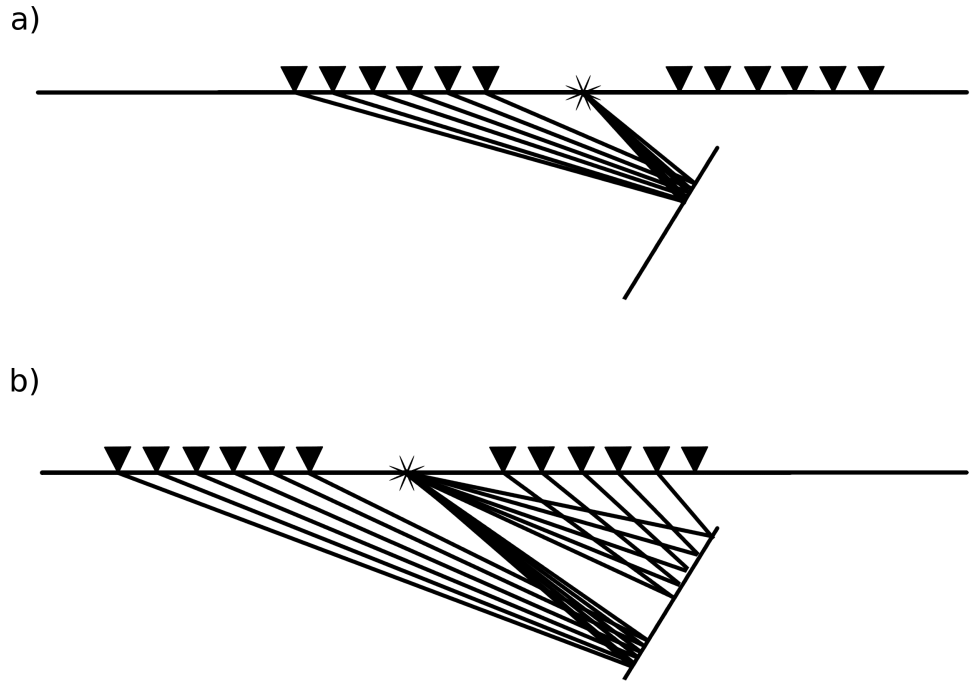

Figure 5.14: *Split-spread geometry above a steeply dipping reflector. The sample density and the ability to sample the reflector differs along each side of the spread: a) close to the source and b) with greater distance to the source.*

segment. The same is illustrated in Figure 5.16 for the eastern SJ-6 line segment.
The image quality of the one-sided images is less compared to the original image as the fold is halved. The comparison of the *left-lateral* seismic image in Figure 5.15 b) and the *right-lateral* image in Figure 5.15 c) shows a significant difference in the background reflectivity. Basic features, for example the high reflective lower crust, appear in both depth sections. The right-lateral image seems to contain weaker amplitudes compared to the left-lateral image. The most significant differences between the images are highlighted by arrows in Figure 5.15. Southwest dipping structures are better constrained in the left-lateral image and northeast dipping structures in the right-lateral image, respectively. Structures at the image margins are better resolved in the left-lateral image. However, structures in the right-lateral depth section appear more distinct and less obscured compared to the left-lateral depth section. The right-lateral image contains short northeast dipping reflectors in the upper crust between x =-45 km and -40 km that have only been imaged by the high-frequency data using Reflection Image Spectroscopy (Figure 5.1 f)).
Along the eastern SJ-6 segment the one-sided images considerably differ and new structures appear that are masked in the original image. Figure 5.16 c) shows a gap of data which is caused by a change of the acquistion geometry from split-spread to end-on spread. All 48 receivers have been placed east to the source across the San Joaquin Valley. Nevertheless, the left-lateral image contains distinct reflectors in the western Franciscan Block at midcrustal depths between 8 km and 20 km depth and along the east flank of the San Joaquin basin syncline down to 12 km depth. Furthermore, a steeply east dipping structure appears beneath the antiformal structure farther west at depths between 8 km and 18 km. Along the eastern San Joaquin Valley the left-lateral image contains a region of high reflectivity beneath the sedimentary basement reflector between $x = 95$ km and 105 km. Smaller east dipping reflector elements can be observed in the middle crust farther east. The prominent subhorizontal lower crustal reflector at 25 km depth at the eastern margin of the image appears much stronger compared to the right-lateral image and the full-spread image. The well constrained features observed in the left-lateral image are superimposed in the full-spread image by background migration noise from the right-lateral data.
Migration of particular traces selected by their relative position left or right to the source yields additional structural information of particularly small or strongly dipping reflectors that are otherwise superimposed by migration noise in the seismic images obtained from the complete spread.

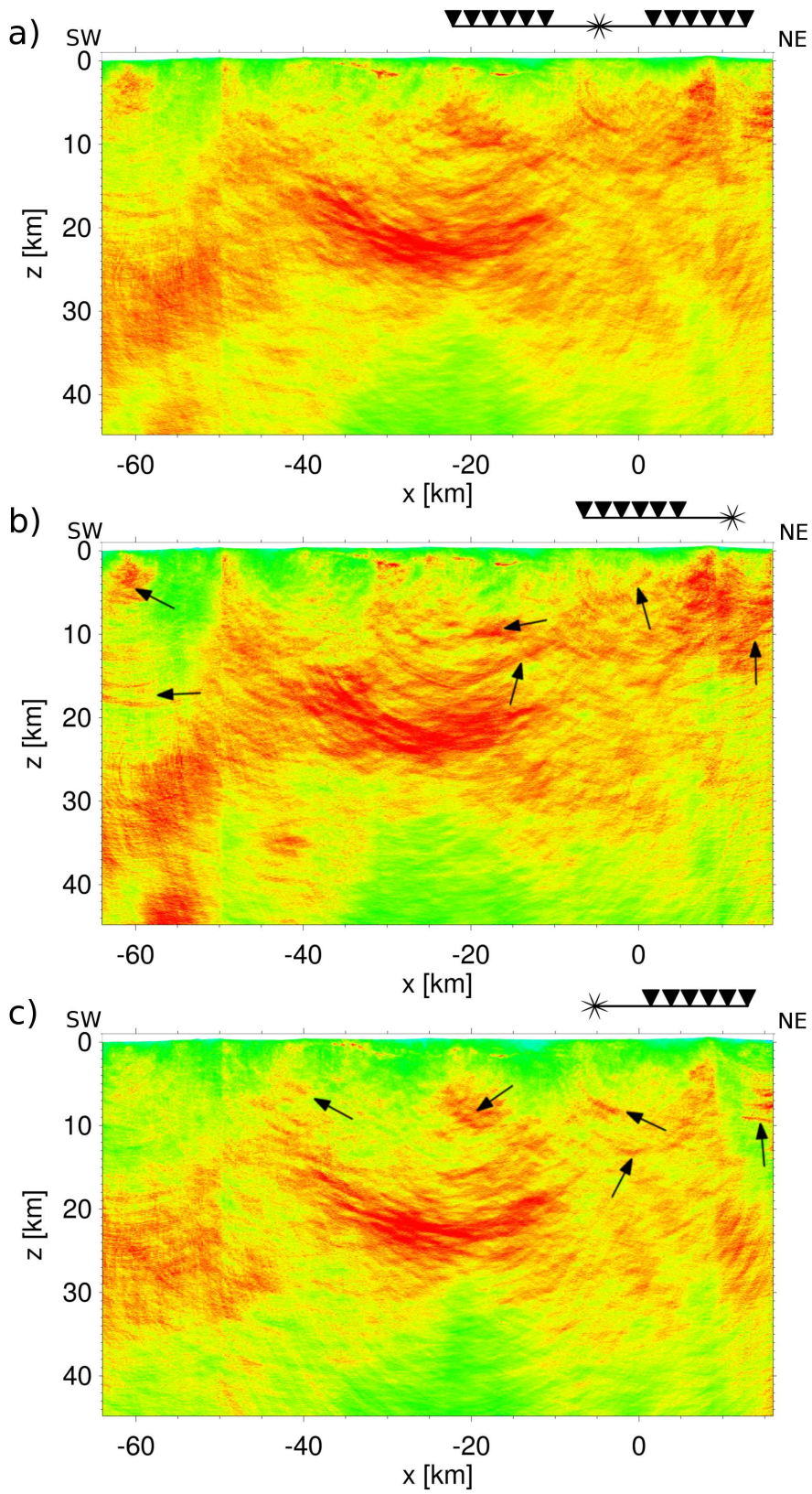

Figure 5.15: *One sided seismic images from migration of only one half of the spread along the southwestern line segment. a) full spread, b) southwestern spread and c) northeastern spread.*

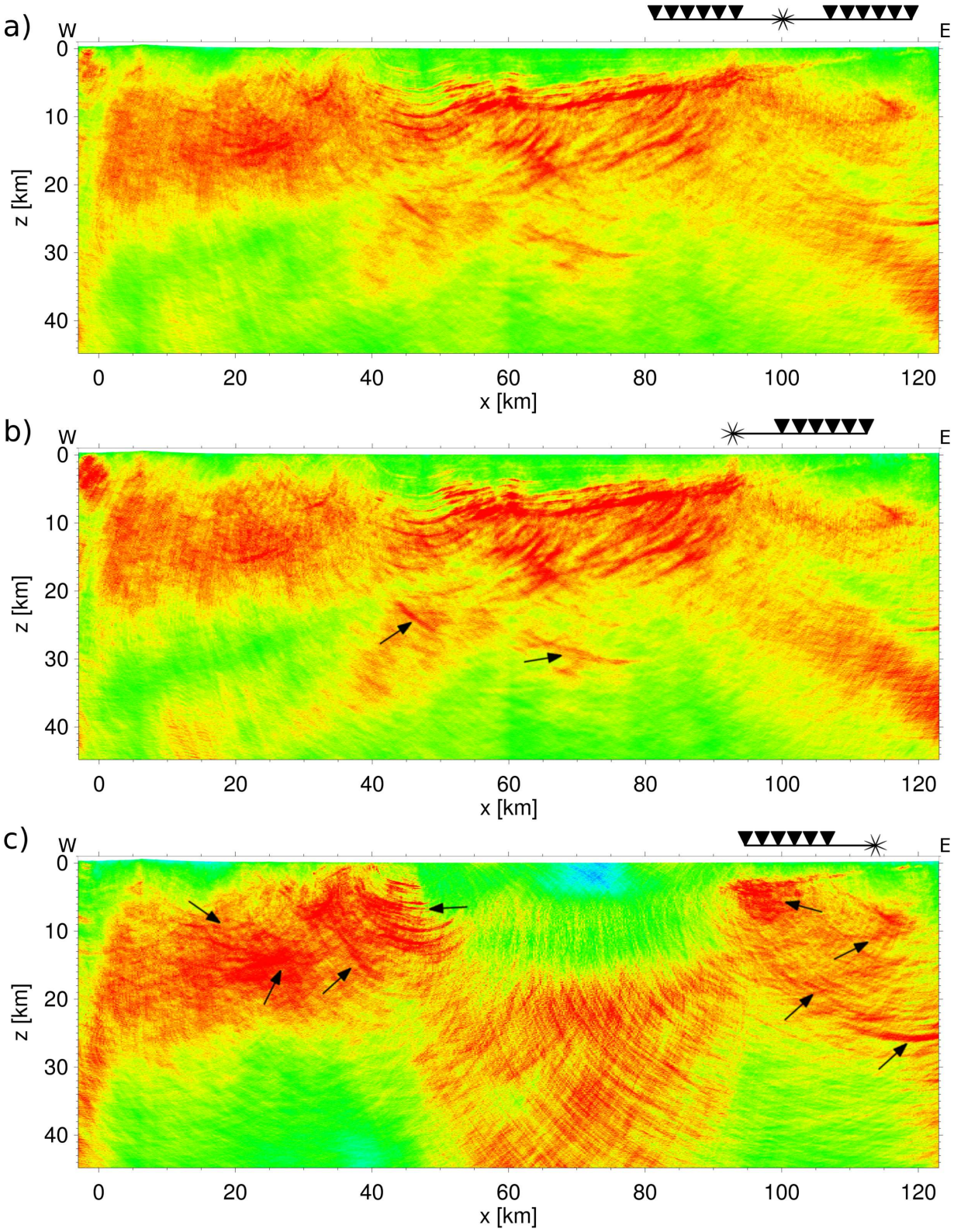

Figure 5.16: *One sided seismic images from migration of only one half of the spread along the eastern line segment. a) full spread, b) western spread and c) eastern spread.*

5.5 Conclusion

The migrated and stacked depth sections resulting from Kirchhoff Prestack Depth migration, Fresnel Volume migration and Reflection Image Spectroscopy applied to the SJ-6 reflection data set show a various amount of very distinctive structural details throughout the entire crust beneath the Coast Ranges and the San Joaquin Valley. However, the results show considerable differences in resolution and quality of the imaged structures.

Three imaging approaches by comparison

The Kirchhoff Prestack Depth images give a first impression of the large scale structures in the centre of the depth sections. Potential structures at the image margins and in the lower crust are superimposed by a high level of background migration noise. However, the shallow subsurface structures in the Salinian Block as well as beneath the Great Valley appear considerably more coherent and stronger in the Kirchhoff Prestack Depth image as in the corresponding parts of the Fresnel Volume image.
The Fresnel Volume images show significantly higher signal-to-noise ratios and reveal more structural details than the Kirchhoff Prestack Depth images, especially within the lower crust. However, some single structures can be identified in the Kirchhoff Prestack Depth images that remain hidden in the corresponding Fresnel Volume images (e.g. reflectors B and D in Figure 5.4 and reflector C in Figure 5.11). Therefore, Reflection Image Spectroscopy in combination with Fresnel Volume migration provides narrow-frequency band images that expose additional structural details. Reflectors that have not been imaged in the Fresnel Volume depth sections as mentioned above reappear in the high-frequency depth sections. Where attenuation of high frequencies in the upper crust is low as it is for example in the Salinian Block, deeper structures are imaged properly and the resolution is significantly enhanced as individual narrow reflector elements can be distinguished down to depths of 20 km.
Fresnel Volume migration is strongly frequency dependent. The dominant frequency is important for the calculation of the Fresnel Volume. Another frequency dependent parameter is the choice of the time window when comparing the trace to trace coherence for emergence angle estimation. The results show that the time window for the comparison of the trace to trace coherence is chosen too large for imaging the high frequency components in the full-frequency data range. That is why reflector C in Figure 5.11 c) remains hidden. A possible solution to this problem would be to simply reduce the number of samples in the time window. This would in contrast expulse low-frequency components.

All in all, Kirchhoff Prestack Depth migration is capable to image deep structures of the SJ-6 reflection data set although the depth sections are strongly influenced by migration noise. The advantage over Fresnel Volume migration is that calculation time is rather fast even though the data volume is large. The additional routines that are necessary to restrict the migration operator during Fresnel Volume migration are time consuming but produce seismic images of enhanced quality that reveal more structural details compared to the Kirchhoff Prestack Depth images. However, the method strongly depends on the frequency content of the data as Reflection Image Spectroscopy confirms. It is therefor an important tool to image additional high- and/or low-frequency components that would have been hidden in the full-frequency range image.
Additional structures could be exposed from the data by migrating selected traces from one side of the original split-spread geometry. Especially steep dipping structures could be better resolved and one east dipping reflector beneath the Kettleman Hills could be uncovered that was neither imaged by Fresnel Volume and Kirchhoff Prestack Depth migration nor by Reflection Image Spectroscopy.

Reflector maps

The application of three migration techniques yields depth sections that are similiar on the whole but show significant differences in the quality by means of resolution and appearence of the imaged structures. The individual results are combined by examining each individual depth section for distinctive reflectors that are traced and pictured in Figure 5.17 for the southerwestern SJ-6 line segment and the eastern SJ-6 line segment, respectively. Altogether, seven depth sections have been compared for each line segment separately, the Kirchhoff Prestack Depth image, the Fresnel Volume image, the three narrow-frequency band images and finally the two one-sided images.
Distinctive structures can be traced through the whole depth section along the entire profile line. The only exception is the region beneath the Nacimiento-Rinconada fault zones where data coverage is low. The strong bend of the acquisition line might also disrupt the imaging results.
In contrast to the results of Trehu and Wheeler (1987) the new images depict a large number of distinctive structures, especially from beneath the western Franciscan Block and the San Andreas fault zone. The deep northeast dipping lower crustal reflectors as well as the west dipping middle crustal reflectors of the Salinian Block are confirmed.
The most significant difference to previous studies of Bloch et al. (1993) and Walter et al. (1987) along the eastern SJ-6 line segment are the west dipping structures from beneath

the basin sediments and deeper crustal reflectors below the San Joaquin Valley. The resolution of the background model does not provide such a detailed image and classification of the sedimentary layer sequences as was derived by Bloch et al. (1993) but middle to lower crustal structures are firstly imaged using the SJ-6 data set.

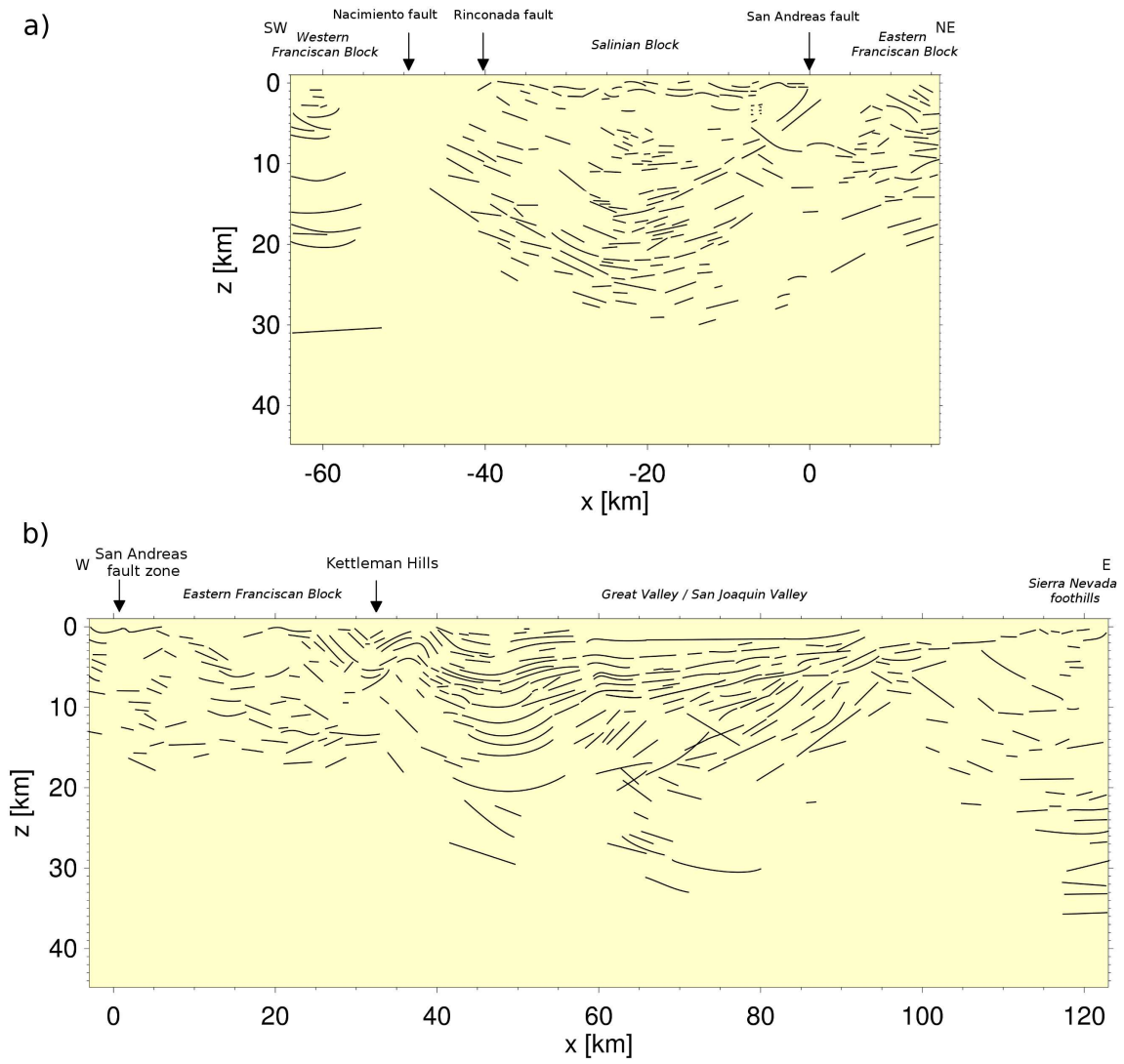

Figure 5.17: *Reflectors map along a) the southwestern SJ-6 line segment and b) the eastern SJ-6 line segment, respectively.*

6 Discussion of the Imaging Results

The following chapter attempts to discuss and partially interpret the SJ-6 imaging results on the basis of other recently obtained geophysical data from the SJ-6 investigation area but also from other sites across the San Andreas fault zone. These data include local seismicity and non-volcanic tremor locations that have previously been introduced in section 2.1.2 and 2.1.3, magnetotelluric data obtained by Becken et al. (2011) that have been further investigated by Tietze et al. (2013) as well as the combined velocity information of Thurber et al. (2006) and Lin et al. (2010). Existing interpretations from the reflection/refraction Transec C2 near Monterey Bay from Fuis et al. (1990) approximately 200 km northwest of Cholame, and from Parkfield (SAFOD2003 reflection/refraction data) are incorporated.

Figures 6.1 a) and 6.1 b) show the local seismicity and non-volcanic tremor locations superimposed on the Fresnel Volume depth sections of the southwestern and the eastern SJ-6 line segment, respectively. Seismic events are commonly supposed to occur in rock formations of predomiantly brittle rheology. From this the brittle-ductile transition zone is inferred from the maximum depths of the seismic events (white dashed lines). It can be seen that the seismic activity is densely concentrated within the fault zones, such as the Nacimiento fault and the San Andreas fault zone, respectively. Seismic events are broadly distributed apart from the fault zones, especially beneath the western margin of the San Joaquin Valley. Non-volcanic tremor events have been located within the deep San Andreas fault zone. The vertical onset of non-volcanic tremor correlates with the break-off of seismic activity. The locations of non-volcanic tremor events are broadly distributed and the majority of events concentrate southwest of the San Andreas fault zone. Figure 6.2 illustrates the 3D inversion results derived from magnetotelluric data by Tietze et al. (2013) from a profile that runs nearly perpendicular for the most part of line SJ-6. Further, the iso-velocity lines of the interpolated and combined velocity models of Thurber et al. (2006) and Lin et al. (2010) in comparison with the reflectors map are shown in Figures 6.3 a) and b). In the following, each segment along the SJ-6 profile line is discussed separately according to the major geomorphological units.

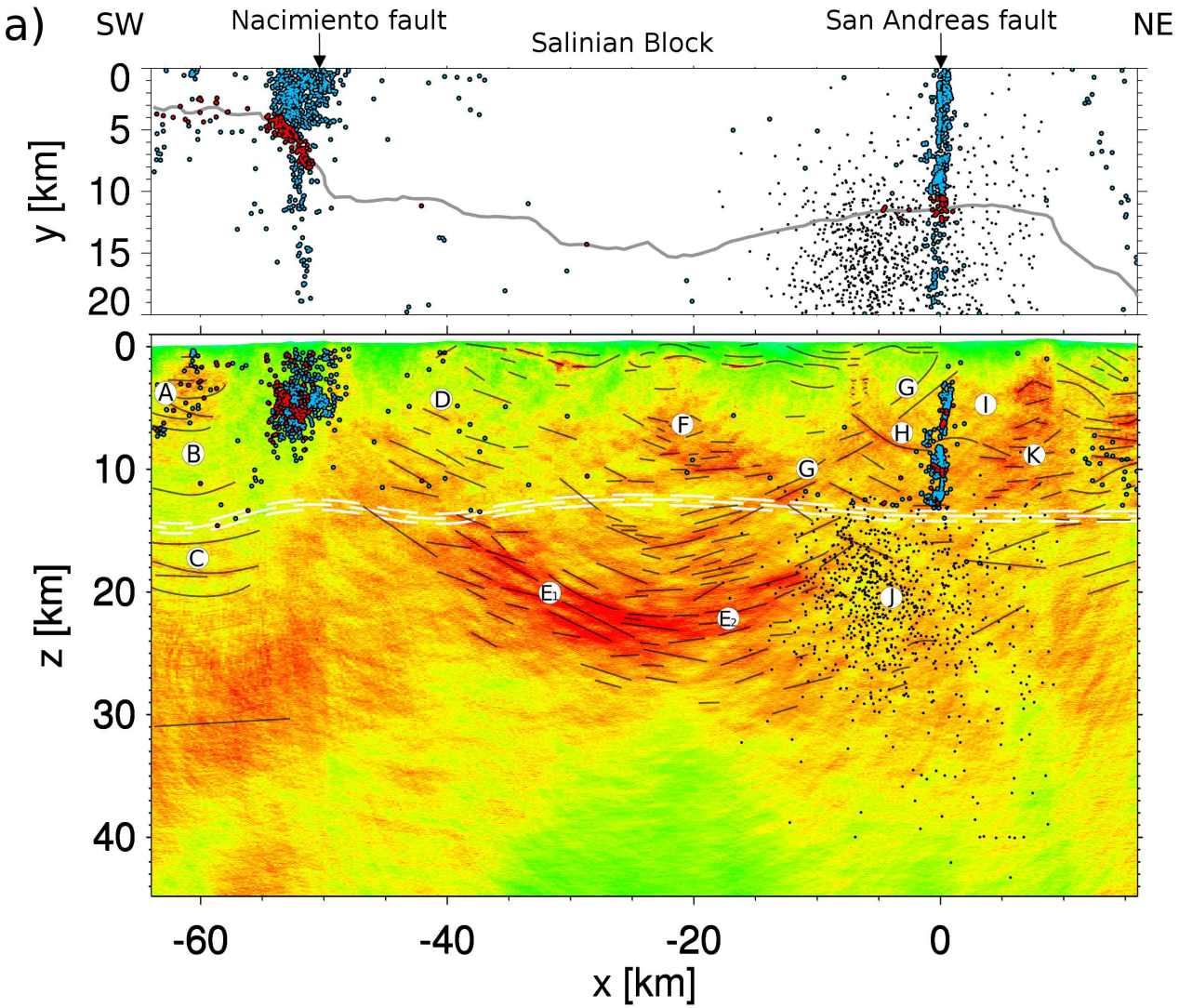

Figure 6.1: *Seismicity vs. Reflectivity. Local seismicity (blue points) from Waldhauser and Schaff (2008) and non-volcanic tremor locations (black dots) from Nadeau et al. (2009) superimposed on the Fresnel Volume depth section and reflector map (black lines) of a) the southwestern SJ-6 line segment and b) the eastern line segment, respectively. Respective map views are on top. Red points indicate seismic events from within* 1 *km distance to the SJ-6 survey line.*

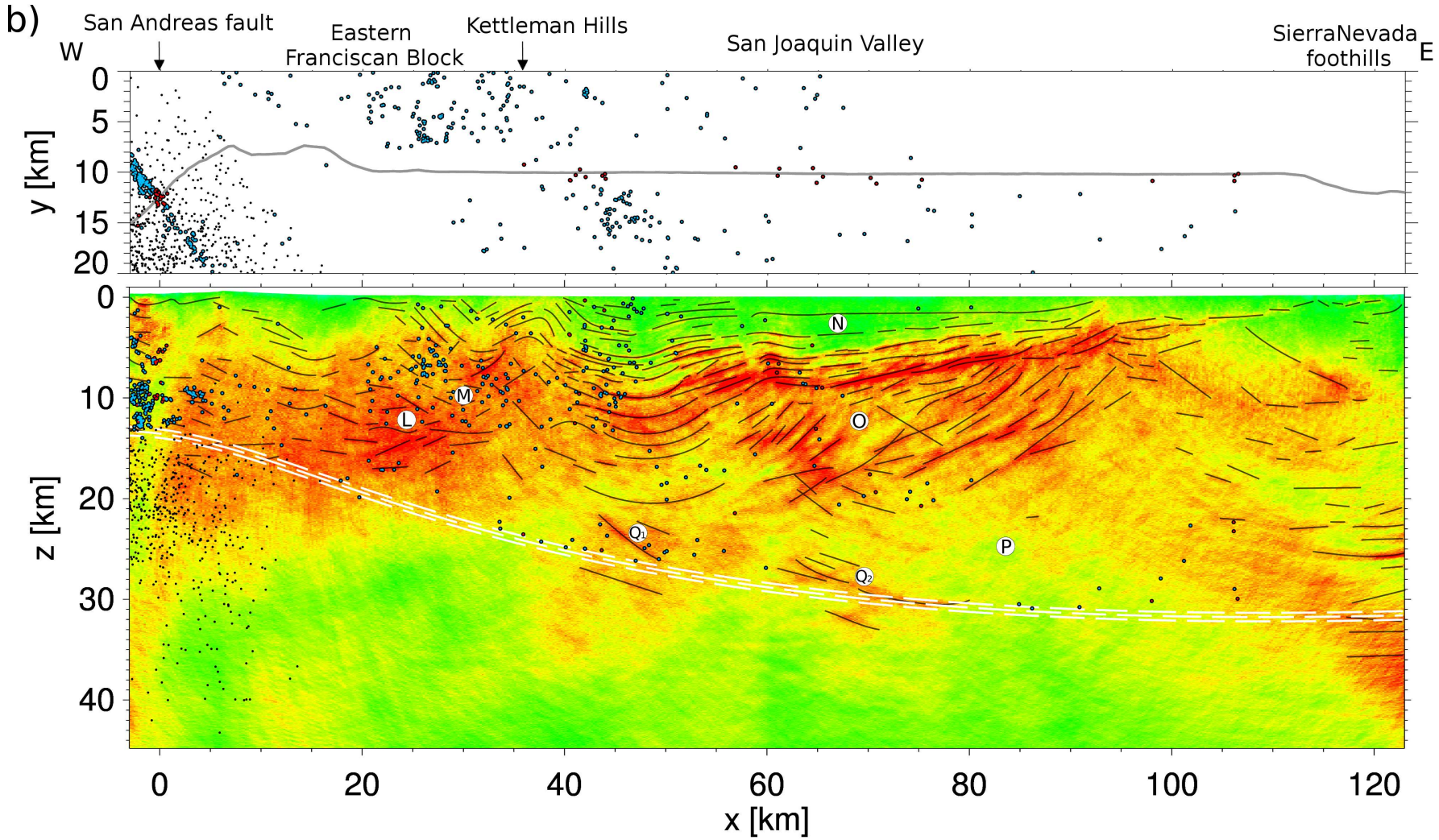

Figure 6.1: *(continued).*

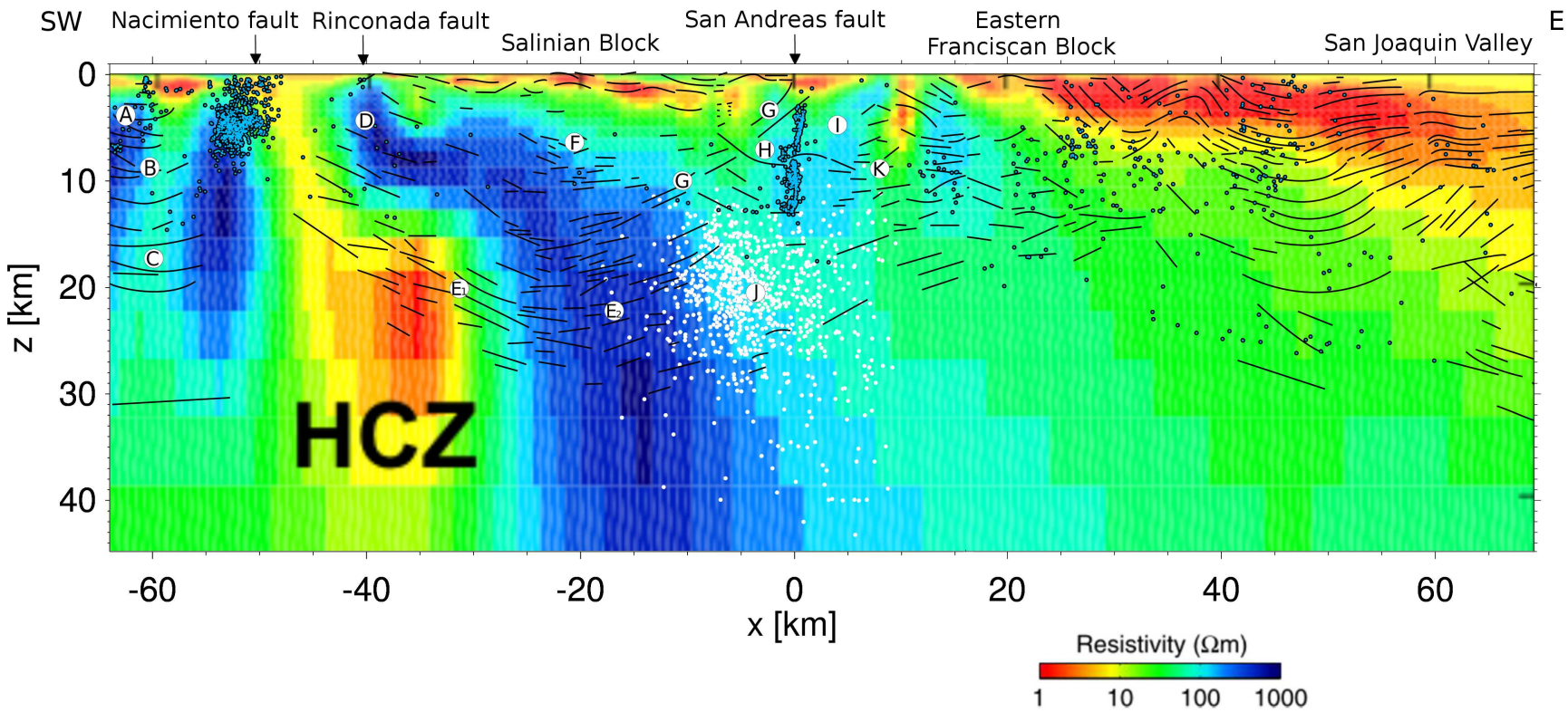

Figure 6.2: *Resistivity structure from 3D inversion of magnetotelluric data (Tietze et al., 2013) conducted near Cholame. White dots represent non-volcanic tremor locations, blue dots seismicity, black lines represent the reflectivity structure from the SJ-6 reflection data. HCZ - high conductivity zone.*

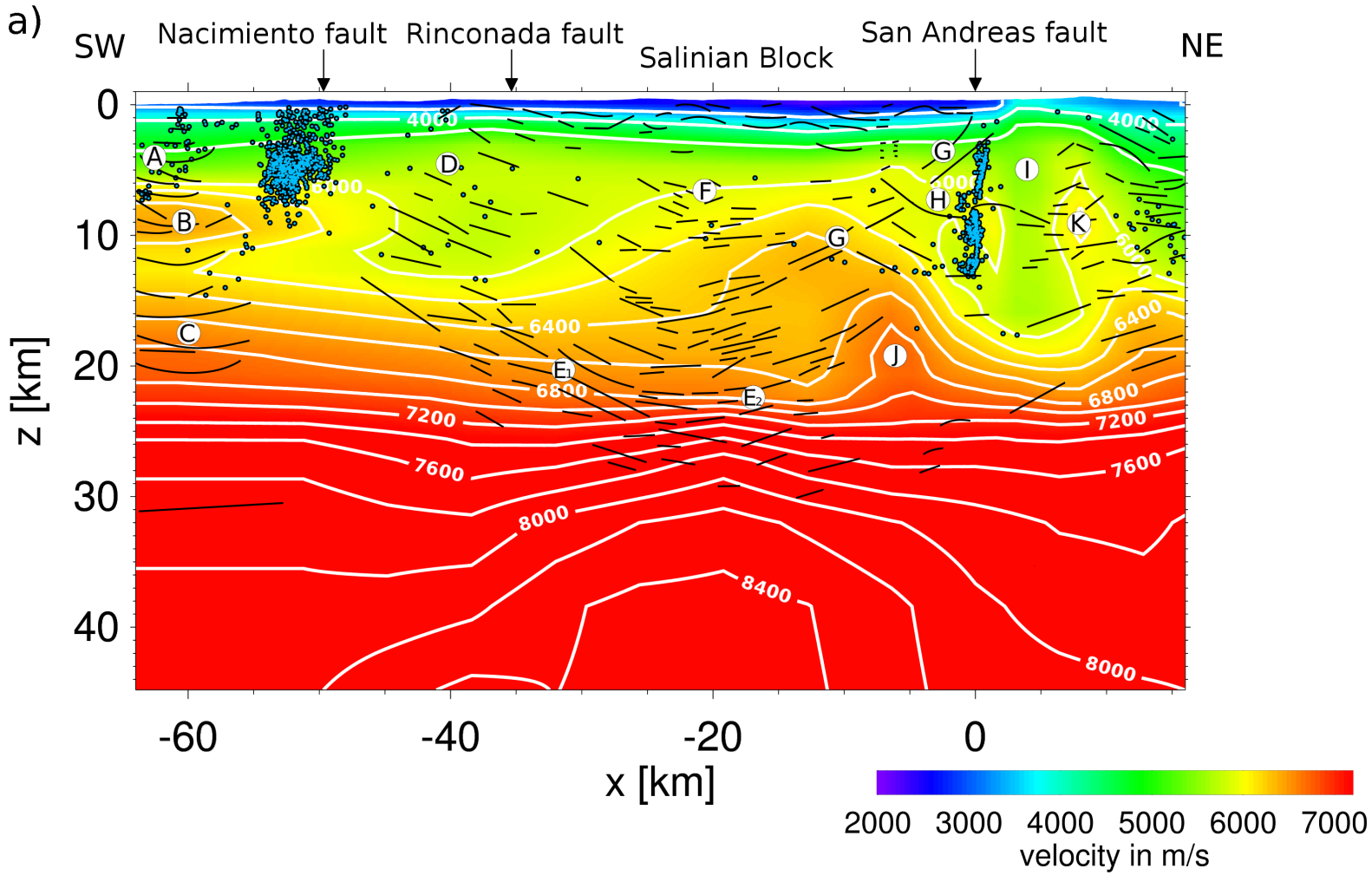

Figure 6.3: *Velocity model and isovelocity lines (white lines in $\frac{m}{s}$) from the interpolated velocity models of Thurber et al. (2006) and Lin et al. (2010). Black lines represent reflectors from the combined imaging results of a) the southwestern SJ-6 line segment and b) the eastern SJ-6 line segment, respectively.*

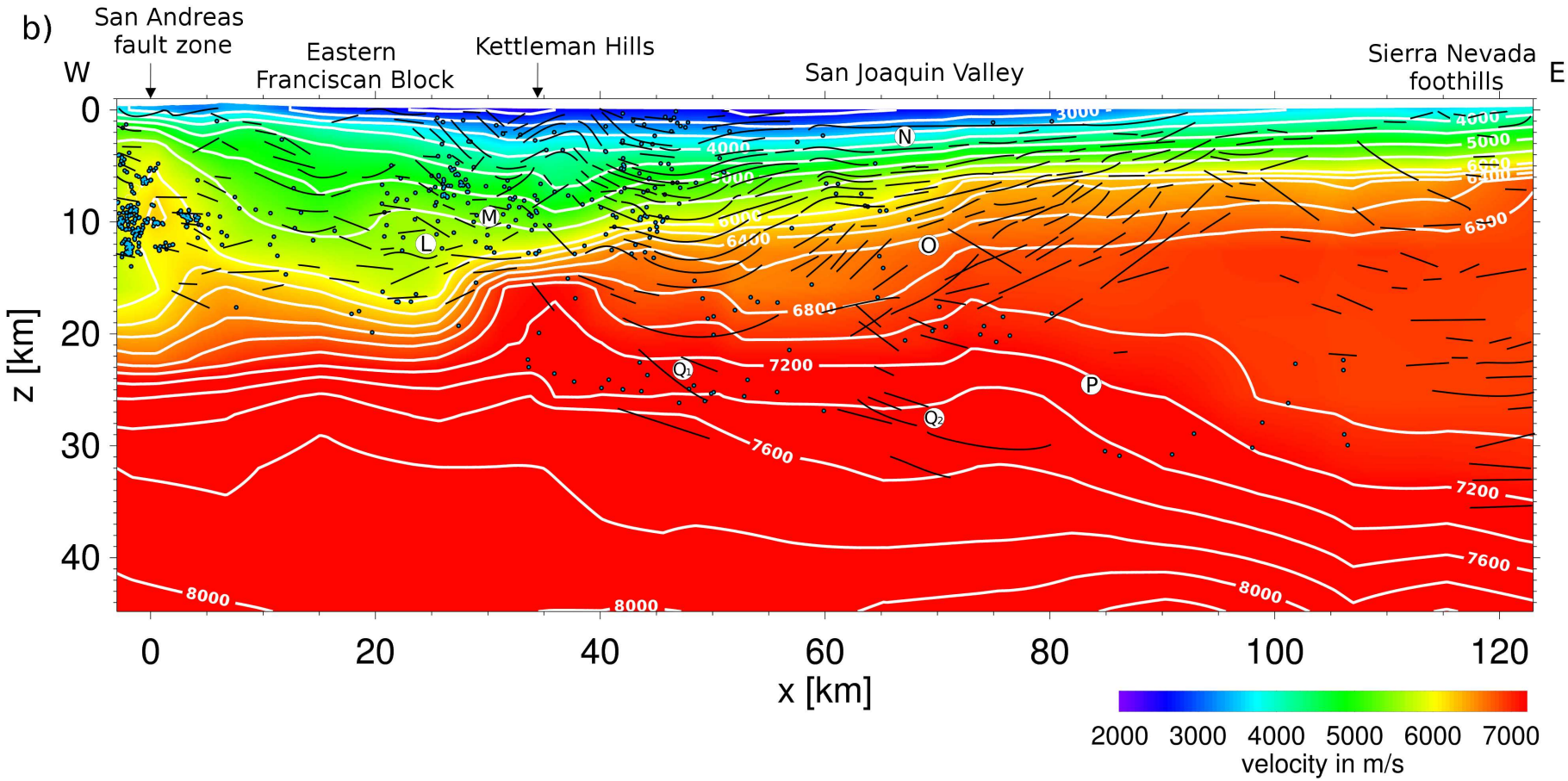

Figure 6.3: *(continued).*

Western Franciscan Block and Nacimiento fault zone

The upper crust of the Franciscan Block is poorly imaged by the SJ-6 data. The boundary between sedimentary sequences and basement rocks can not be inferred from the migrated reflection seismic data. High conductivities in the upper 2 km indicate sedimentary deposits. Below 2 km depth the seismic image reveals a body of high reflectivity (A in Figure 6.1) and subhorizontal distinct reflectors that show a high level of broadly distributed seismic activity. It can be inferred that the upper crust of the western Franciscan Block is faulted. The base of the high reflective body at 7 km depth is marked by a strong and distinct northeast dipping reflector. At this point a zone of increased velocities ($6400\frac{m}{s}$) (B in Figure 6.3) can be observed between 7 and 12 km depth. In his work, Fliedner et al. (2000) reports this velocity increase in the western Franciscan Block as well at identical depths. As Franciscan rocks are melanges of very different rock types that form various subterranes, Fliedner et al. (2000) propose that mixtures of low-velocity Franciscan rocks with high-velocity mafic or ultramafic rocks form this high-velocity zone in the middle crust. It can be noticed that seismic events are occuring outside around this high-velocity zone which implicates a mechanically strong material within this zone.

As velocities slightly decrease below 12 km depth Fliedner at al. (2000) propose that the lower crustal Franciscan rocks are mixed with oceanic crust (C). The strong reflectors in the lower crust can be interpreted as lower crustal detachement zones that additionally might indicate a transition from mixed rocks to more or less pure oceanic crust at the base of the Franciscan Block.

A clear reflector that might represent the Moho can not be observed in this part of the depth section. Fuis et al. (1990) as well as Süss and Shaw (2003) report Moho depths of 24 to 26 km southwest of the Salinian Block.

The Nacimiento fault zone is a complex structure that experienced different types of fault motion in history (Page (1970), Dickinson (1983)). It is expressed at the surface by many fault traces. Unfortunately, the seismic images obtained within the scope of this work do not show any clear reflection signals from within the Nacimiento fault zone. Nevertheless, despite the irregularities in the trend of the survey line and a certain lack of data the termination of reflectors southwest of the Nacimiento fault zone correlate with the onset of densly packed seismic events. Across this broad fault zone the predominating dip of the imaged structures changes from nearly horizontal in the eastern Franciscan Block to predominantly northeast in the adjacent Salinian Block which implies a change of rock types. Catchings et al. (2008) used the SJ-6 data set and imaged steeply dipping faults from which they inferred a positive flower structure within the Nacimiento fault zone. In a broader sense, the northeast dipping structures in the adjacent Salinian Block and the

northeast directed trend of earthquakes close to the SJ-6 line (red points in Figure 6.1 a)) make the Nacimiento fault zone appear as if it mainly consists of currently northeast dipping thrust fault zones.

Salinian Block

The subhorizontal reflectors imaged in the upper 2 km of the Salinian Block represent the basement of the sedimentary layer sequences. Seismic velocities below $5000\frac{m}{s}$ and low electrical resisitivities confirm this interpretation. The sedimentary cover underwent faulting and folding as the disconnected appearence and irregular shapes of the reflectors indicate.

Within the crustal basement two subregions can be distinguished. The southwestern Salinian Block is characterized by low velocities, relatively high electrical resistivities and, apart from some sparsely distributed northeast dipping reflectors (D in Figure 6.1 a) and Figure 6.2), low reflectivities in the upper crust. Only few seismic events are reported from within the Salinian Block. The southwestern events are located within the low velocity zone in the upper crust that coincides with the northeast dipping reflectors D that are suggested to represent faults in the upper crust. The lower crust coincides with a bundle of strong northeast dipping reflectors (E_1) that are located on top and partly within a high conductivity zone. Becken et al. (2012) presumes this high conductivity zone as a fluid source region in the upper mantle, releasing mantle derived fluids or lower crustal fluids into the crustal regions above.

The northeastern part of the Salinian Block exhibits high reflectivities in the upper and middle crust with short subhorizontal reflectors (F). At aproximately the same depth Bleibinhaus et al. (2003) imaged two distinct subhorizontal reflectors southwest to the San Andreas fault zone near Parkfield. They attribute these structures to layers of metasedimentary rocks beneath the granitic rocks of the batholith. This interpretation can not be applied to the SJ-6 imaging results because neither the electrical resistivity structure nor the velocity structure supports this interpretation. Compared to the southwestern Salinian Block the velocities are significantly increased and also electrical resistivities are slightly higher in the northeastern part of the Salinian Block. There, the lower, highly resistive crust again consists of strong layered reflectors (E_2) just as in the southwestern part of the Salinian Block but the predominating dip changes from northeast to predominantly southwest in the northeastern part. These lower crustal reflectors (E_1 and E_2) might represent a laminated lower crust or rather a laminated Moho transition zone. As proposed by Eaton and Rymer (1990) the lamination of lower crust is supposed to indicate its ductility and it may represent a detachement that is a zone of decoupling between

the crust and the upper mantle. Meissner et al. (2006) reports of narrow-angle seismic experiments from various world-wide locations that exhibit seismic lamination in the continental lower crust in conjunction with observed seismic anisotropy. Moreover, Ozacar and Zandt (2009) observed a strong anisotropic lower crust southwest of the San Andreas fault near Parkfield from teleseismic receiver function studies. They relate this anisotropy to fossil fabric of the Farallon subduction consisting of serpentinite or fluid filled schist layers. Near Parkfield their observation correlates with high condictivity and low velocities that can not be observed beneath line SJ-6. According to Meissner et al. (2006), anisotropy studies by wide-angle experiments or receiver function methods in association with seismic reflectivity have a considerable potential to investigate the composition and the processes within the lower crust. Such studies could resolve the character of the lower crust of the Salinian Block.

The strong lower crustal reflectors (E_1 and E_2) terminate abruptly approximately below the San Juan fault surface trace. This termination coincides first, with the onset of non-volcanic tremor activity and second with a steep rise of the $6600\frac{m}{s}$ - isovelocity line, all occurring below reflector G.

The prominent southwest dipping reflector G in Figure 6.1 a) reaches the surface directly where the San Andreas fault is expressed at the surface. The reflector has no seismic signature and can be traced from the shallow crust into the middle crust to 16 km depth. The nature of this prominent reflector is unclear. The quaternary San Juan fault can be recognized from its surface trace position downward as subvertical feature by short reflector elements and increased reflectivity approximately 2 km in width. It can be traced to 7 km depth where it turns into a northeast dipping strong reflector (H) that terminates at the low-reflective San Andreas fault zone. The San Juan fault exhibits low electrical resistivities compared to the high resistivities towards southwest. Seismic velocities that increase in the northeastern part of the Salinian Block decrease at its northeastern margin concurrently with the location of the San Juan fault. As the San Juan fault is an old strike-slip fault it marks the beginning of the transform fault zone that is currently active 7 km northeast at the San Andreas fault.

A transparent reflectivity zone can be seen beneath the lower crustal reflectors (E_1 and E_2) in the center of the depth section at x = -20 km and 26 km depth. The zone coincides with an upward directed bulge of high velocities above $8000\frac{m}{s}$ and is considered to represent upper mantle lithosphere. In either direction from this transparent zone towards the San Andreas fault and the Nacimiento fault zone, the background reflectivity increases and the seismic velocities decrease, simultaneously. This coincidence is the result of the migration process as this particular velocity model served as background velocity model.

As has been shown in section 5.3 the upper mantle is more continuously transparent when a velocity model with less velocity contrasts is used. However, the lower upper mantel velocities in Figure 6.3 a) can be suggested to represent changes in the composition of the upper mantle related to the processes of active fault motion.

San Andreas fault zone

Beneath the San Andreas fault surface trace the seismic reflection data reveal an approximately 4 km wide zone that lacks of coherent reflections (I in Figure 6.1 a)). This zone is interpreted to represent the San Andreas fault zone. The extension of reflector G in Figure 6.1 a) appears to approach the surface directly at 0 km, the surface trace of the San Andreas fault. The left top figure in Figure 6.4 shows the Fresnel Volume imaging result of the SAFOD2003 data set near Parkfield. The southwest dipping one of the two reflectors is interpreted by Buske et al. (2007) to represent the San Andreas fault zone in the upper 4 km. Transferring this reflector to the SJ-6 image (black line in the bottom figure) it coincides with the extension of reflector G. Now the question is, how reflector G is related to the transform motion along the San Andreas transform fault. It might be inferred that reflector G represents a shear zone that could be the structural boundary between Salinian rocks to the southwest and Franciscan rocks to the northeast. It can also be speculated that reflector G is a slip surface that was possibly generated during one or more large earthquakes in historical time.

Seismic event locations form a narrow subvertical band at the southwestern margin of the fault zone between 3 km and 13 km depth while the northeastern part lacks of seismicity. The fault zone, as it is defined by the reflectivity structure, is much broader compared to the seismically defined fault zone. The seismic events define the seismogenic layer where rocks deform predominantly brittle. The brittle to ductile transition is inferred to 13 km depth. The seismic events associated with the fault zone appear to form four clusters as illustrated in Figure 6.4. The upper cluster is vertically elongated within the upper part of the crust showing a slight southwest dip component. At 9 km depth a very small cluster is offset towards southwest. This offset coincides with the appearence of reflector H approaching the fault zone. The third cluster is again located within the San Andreas fault but appears broader compared to the uppermost cluster. The lowermost cluster is located in a low velocity zone between 10 km and 15 km depth. As this particular segment of the San Andreas fault is related to the locked fault segment, the question is where a possible large earthquake would be expected to occur in the future. Would it occur on reflector G, within the seismically active southwestern zone of the San Andreas fault or the seismically inactive transparent northeastern zone?

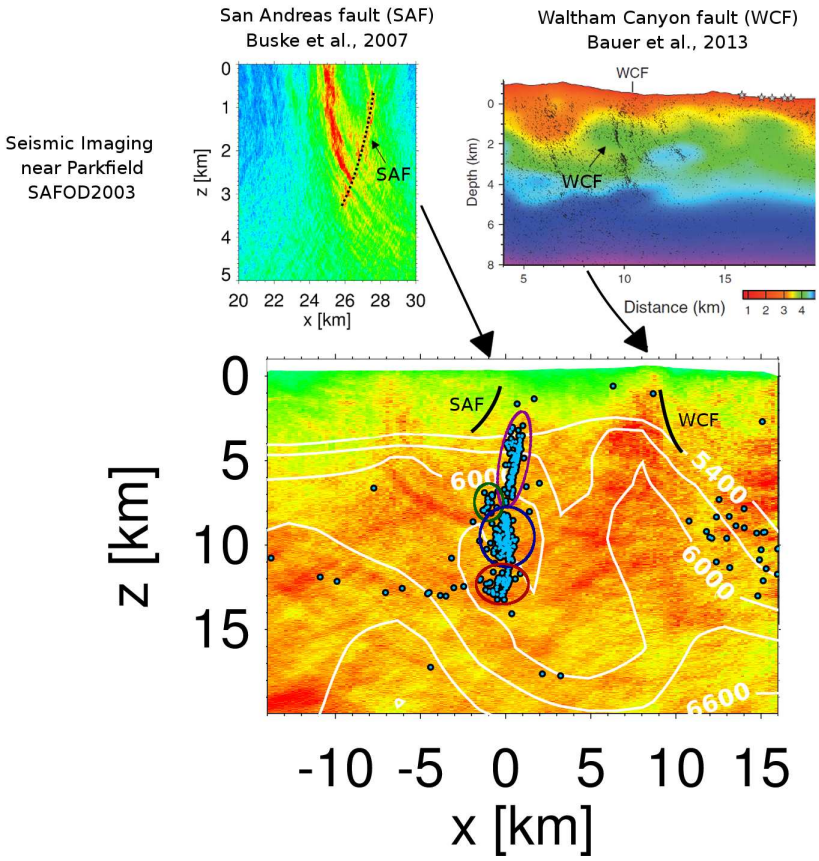

Figure 6.4: *Detailed view of the San Andreas fault zone seismogenic layer. Figures on top are imaging results from the SAFOD2003 data set near Parkfield. Buske et al. (2007) imaged the San Andreas fault down to depths of 4 km as steep southwest dipping reflector. The Waltham Canyon fault is imaged by Bauer et al. (2013) as northeast dipping reflector. The imaging results are transfered to the SJ-6 reflection seismic image at the bottom (black lines). White lines represent iso-velocity lines and blue dots are seismic event locations. The coloured circles mark different clusters that correlate with the reflectivity and the velocity structure.*

The velocity model in Figure 6.3 a) includes a prominent vertical low velocity zone that is offset by approximately 2 km towards northeast from the seismic events. The magnetotelluric data reveal a zone of high resistivity that correlates with the seismic event locations and the low-velocity zone within the seismogenic layer. The low-velocity zone is suggested to be a product of fractured rocks that form a fault gouge. The width of the imaged fault zone remains almost constant within the seismogenic layer but it widens successively with increasing depth below 13 km.

Below the brittle-ductile transition at approximately 13 km depth another type of seismic signals have been located called non-volcanic tremor (black dots in Figure 6.1 a)). Non-

volcanic tremor locations are broadly distributed between x = -15 and 10 km at depths larger than 10 km. Their appearence coincides with the abrupt break-off of seismic events at 13 km depth. The majority of non-volcanic tremor locations concentrate to the south-west side of the deep San Andreas fault beneath the surface trace of the San Juan fault (J in Figure 6.1 a)). The lateral onset of non-volcanic tremor correlates with the termination of the the lower crustal reflectors E_1 and E_2 at x = -11 km. It is supposed that the non-volcanic tremor events are located directly within the deep San Andreas fault zone. The latter is associated with low reflectivities and the absence of coherent reflections in the migrated depth sections. From this, it can be concluded that the San Andreas fault zone widens with increasing depth and that lower crustal deformation occurs across a region that laterally extends over 25 km. The center of the non-volcanic tremor cloud lies directly within a zone of remarkable high seismic velocities. Becken et al. (2012) propose that fluids originating in the high conductivity zone migrate along crustal pathways into the fault zone. North of Cholame they contribute to the process of creep along the fault. Near Cholame these fluids are supposed to be trapped by an impermeable layer beneath the fault and cause high pore fluid pressures that favour brittle deformation in the lower crust and cause non-volcanic tremor activity. However, if the fluid content would be high, one would expect decreased velocities and high contrasts of seismic impedance that would result in strong reflectivities. The increasing seismic velocity might also be explained by a change in rock composition which might have stronger influences on the velocity as potential fluids do.

Although the San Andreas fault is not imaged as a distinct subvertical reflector, it can clearly be identified as an individual structure in the seismic images that penetrates the whole crust.

The crust-mantle boundary beneath the fault zone can not be clearly identified. Reflectivities at depths greater than 24 km are stronger compared to those in the center of the Salinian Block and the adjacent Franciscan Block at the same depths. The seismic images reflect the changing composition of rock formations across the San Andreas fault zone from granitic and metamorphic rocks of the Salinian Block to lower velocity Franciscan Complex rocks towards northeast. Northeast of the fault zone the strong lower crustal reflectors do not reappear and the upper and middle crust is characterized by predominantly subhorizontal reflectors.

Eastern Franciscan Block

The reflectivity structure of the Eastern Franciscan Block differs significantly from the Salinian Block southwest of the San Andreas fault. Highly heterogenous rocks of the Franciscan assemblage in the upper crust cause certain amount of scattering and attenuation that weakens the signal strength of the recorded wavefield. The seismic images contain therefore little structural information on the upper crust northeast of the San Andreas fault where Franciscan assemblage rocks are exposed at the surface between $x = 6$ km and 13 km.

Figures 6.1 b) and 6.3 b) show that the Franciscan Block contains no noticeable velocity anomalies and broadly distributed seismic events within the whole crust down to 20 km depth. The seismic event density significantly increases towards the eastern margin of the Franciscan Block where sedimentary strata sequences are folded in the upper crust.

Figure 6.1 a) shows a noticeable gap of seismicity northeast of the San Andreas fault between $x = 4$ km and 10 km (K). Due to the change of perspective this particular feature is not visible in Figure 6.1 b) as major tectonic structures (e.g. the San Andreas fault and the Kettleman Hills fold) run obliquely with respect to the SJ-6 receiver line. For that reason, the imaged structures can not adequately compared to seismic event locations. Event locations north of the profile line may appear farther west from their related tectonic structures that are imaged in the depth section, just as events from the south are imaged farther east of the related geologic structures, respectively. At $x = 10$ km Figure 6.2 reveals a subvertical low electrical resistivity anomaly and increased seismic velocities between 3 km and approximately 13 km depth. The seismic images show a zone of reduced reflectivity at $x = 10$ km that might indicate a subvertical fault but could be the result of the bad data quality in this region and the significant kink in the SJ-6 survey line as well. However, approximately 30 km northeast near Parkfield Bauer et al. (2013) imaged the Waltham Canyon fault as near vertical structure in the upper crust as it is illustrated in Figure 6.4. Geologic maps (Jennings, 1977) also indicate a fault trace at this location and ultramafic rocks exposed towards southwest of the fault that can explain the observed high velocities.

The base of Franciscan assemblage rocks is supposed to be located between 10 km and 15 km depth underlain by mafic lower crust (Fuis et al. (1990), McBride et al. (1987), Fliedener et al. (2000), Walter et al. (1987), Wentworth et al. (1987)). In the central eastern Franciscan Block the lower base of Franciscan assemblage rocks can hardly be distinguished. Reflectivities are high but distinct reflectors appear infrequently between $x = 0$ km and 20 km. East of 20 km beneath the folded upper crust, the strong reflective wedge shaped structure (L in Figrue 6.1 b)) is accompanied by seismic activity, especially

at the top and at the base of the wedge. Seismic velocities are decreased within and beneath the wedge. According to Walter et al. (1987) and Wentworth et al. (1987) it is assumed that this wedge is composed of Franciscan assemblage rocks that are thrusted beneath the Great Valley Sequence and other rocks towards east. Reflectors on top and at the base of the wedge are suggested to be thrust faults. According to Bloch et al. (1993) the top thrust faults represents the Coast Range thrust that separates Great Valley sequence formations or Coast Range ophiolites in the hanging wall from Franciscan rocks in the foot wall. The wedge tapers out at approximately $x = 35$ km beneath the Kettleman Hills. The top of the wedge is connected to a zone that lacks of distinct reflectors and has lower reflectivities (M in Figure 6.1 b)) compared to the Franciscan rocks beneath. Godfrey et al. (1998) proposes that Franciscan rocks are mixed with ophiolitic rocks and other rock types due to tectonic wedging of Franciscan material beneath the Great Valley. It is possible that this zone is a damage zone that expresses the Coast Range fault itself. Another possibility might be that this zone represents Coast Range ophiolites located between Franciscan rocks and rocks of the Great Valley sequence above.
The sedimentary layer sequences at the eastern margin of the Franciscan Block are folded and faulted. Due to the large grid spacing it is not possible to image the internal structure very presicely as has been done before (e.g. Bloch et al. (1993)). The indistinct reflectivity structures especially beneath the Kettleman Hills South Dome indicate irregular structures.
The crust-mantle boundary can be inferred from the seismic images by a significant change from high reflectivities in the lower crust to low reflectivities in the upper mantle. The Moho depth of approximately 24 km correlates with observations of Fuis et al. (1990) and Fliedner et al. (2000) who propose Moho depths of $24 - 26$ km beneath the eastern Franciscan Block.

San Joaquin Valley

The seismic images reveal west dipping sedimentary layer sequences (N in Figure 6.1 b)) beneath the San Joaquin Valley that are folded at the western margin of the valley. This is consistent with previous studies of Walter et al. (1987), Bloch et al. (1993) and other studies across the Great Valley that are combined and summarized by Godfrey et al. (1998). The basement of the San Joaquin Valley beneath line SJ-6 consist of steeper west dipping reflectors between 10 km depth and 16 km depth in the center of the San Joaquin Valley (O in Figure 6.1 b)). Although the velocity data presented in Figure 6.3 b) do not show any significant velocity anomaly, Fliedner et al. (2000) detected a high velocity body beneath the sedimentary layer sequences that he, according

to Godfrey et al. (1998), referred to as Great Valley ophiolites. The west dipping reflectors may represent shear zones within the Great Valley ophiolite. Seismic events are rather concentrated to the western margin of the San Joaquin Valley and to the base of the Great Valley ophiolite at approximately 20 km depth. According to Fliedener et al. (2000) the Great Valley ophiolite is underlain by old continental crust (P in Figure 6.1 b)) since he observed decreased velocities in the lower crust. The contact of Great Valley ophiolites and the presumably underlaying continental crust can clearly be inferred from the seismic images by the significant change in the reflectivity structure from a body of west dipping strong reflectors to a nearly transparent region beneath and eastward adjacent to approximately $x = 95$ km. The transparent body seems to form a westward thinning wedge that tapers out at approximately $x = 42$ km beneath the western margin of the San Joaquin basin. The lower boundary of the wedge is marked by east dipping reflectors (Q_1 and Q_2 in Figure 6.1 b)) in the lower crust that presumably represent the crust mantle boundary or a detachement in the lower crust. Reflectors Q_1 and Q_2 are accompanied by seismic events that demonstrate brittle deformation in the lower crust. Beneath these distinct reflectors the reflectivity structure is transparent that could indicate upper mantle material. However, it can clearly be recognised that the crust thickens towards east. Subparallel, subhorizontal reflectors beneath the Sierra Nevada foothills at the eastern margin of the image appear beneath 20 km depth. Reflectors beneath 30 km depth are suggested to represent the transition from the lower crust to the upper mantle.

It can not be excluded from the seismic images if there is a local connection between the Great Valley ophiolite beneath the San Joaquin Valley and, if present, the Coast Range ophiolite at the eastern margin of the Franciscan Block.

7 Conclusions

Old seismic data often contain valuable subsurface information that have so far not been revealed by standard processing techniques. This thesis has demonstrated that modern imaging techniques applied to old reflection seismic data are capable to reveal additional information on the reflectivity structure compared to previous studies. Beyond that, the data processing and imaging techniques have been modified in order to extend the target depths from the originally shallow crust to the lower crust and the upper mantle, respectively. Standard Kirchhoff Prestack Depth migration, the advanced Fresnel Volume migration approach and Reflection Image Spectroscopy, respectively, have been applied to the industry reflection seismic data set SJ-6 in order to obtain further structural information on the deep crustal structure across the prominent San Andreas fault system in south central California, USA.

The industry reflection data set SJ-6 was originally acquired for the exploration of oil and gas reservoirs in the shallow crust. Thus, the record length of 6 seconds two-way travel time and the relatively short offsets of 1.8 km are actually not suitable for imaging deep crustal structures. Fortunately, vibration sources of sufficiently long duration have been used so that the record length of the original field records could be extended to 26 seconds two-way travel time in order to extract reflection signals from the deeper parts of the crust and in particular from the deep extention of the San Andreas fault zone.

Due to the crooked course of line SJ-6 and the change of orientation near the intersection with the San Andreas fault zone, the imaging techniques have been implemented in 3D. A final 2D depth image has then be obtained from the migrated 3D volumes by interpolating the migrated wavefield to a vertical plane directly beneath the receiver line. Kirchhoff Prestack Depth migration was able to handle the crooked receiver line geometry. However, due to the very short offsets used during the acquisition process the coverage of the migrated wavefield significantly varied with depth after stacking. Consequently, shallow structures were to a greater extend superimposed by migration noise than deeper structures. For that reason, the stacking procedure has been modified so that shallow as well as deep subsurface structures could be resolved in equal measure. Although Kirchhoff

Prestack Depth migration revealed several significant crustal features, the depth images contain a considerable amount of migration noise, especially at the image margins, that makes structural interpretation difficult.
In contrast, the Fresnel Volume migration approach produced seismic images of enhanced quality that are to a lower extent affected by migration noise and reveal several additional distinct structures. The crooked line geometry had a considerable impact on the image quality and thus had to be considered during slowness calculation. By this means, the wavefield was attributed to the close vicinity of the receiver line during the migration process so that migration artefacts could be reduced significantly. Slowness estimation as well as the calculation of the Fresnel Volumes strongly depends on the dominant frequency of the data. As the frequency range is sufficiently wide several components of the wavefield were not properly imaged by Fresnel Volume migration.
Reflection Image Spectroscopy is therefor a powerful tool to investigate the frequency dependence of the imaged structures. Hence, Fresnel Volume migration was performed after applying particular bandpass filter to the data. Several structures have been significantly enhanced and even additional structures were imaged.
It was further shown that the imaging results can be complemented when particular geophone groups from each side of the source are considered separately.
Furthermore, the impact of the required a priori velocity model on the imaging results was shown by including two different velocity models in the migration process. The image quality and the reflectors sharpness were higher when a more detailed velocity model obtained from earthquake tomography was used.

The imaging results from Kirchhoff Prestack Depth migration, Fresnel Volume migration and Reflection Image Spectroscopy have been considered to identify the most striking structures which were combined by manually creating reflector maps. The latter were compared and discussed under consideration of other geophysical studies using passive seismic data, magnetotelluric data and the seismic velocity information from nearly the same location.
Previous imaging results of the SJ-6 data set could be verified and many additional structures could be imaged for the first time. It was shown that the reflectivity structure of the individual neighbouring blocks across the San Andreas fault system considerably differ. Major active strike slip faults, e.g. the Nacimiento fault and the San Andreas fault, respectively, can not be identified by distinct reflectors but as near vertical zones that lack of distinct reflectors.
The imaged structures in the western Franciscan Block are in principle subhorizontal

while structures imaged in the southwestern part of the adjacent Salinian Block are predominantly northeast oriented. The lower crust of the Salinian Block is characterized by strong subhorizontal layered reflectors that indicate a laminated lower crust which is interpreted to be the result of ductile deformation. The Moho can be inferred by the abrupt transition from the high reflective lower crust to a nearly transparent upper mantle at approximately 26 km depth.
Within the upper and middle crust the San Andreas fault zone was characterized by a subvertical predominantly transparent zone approximately 4 km in width. The fault zone successively broadens beneath the brittle-ductile transition zone at 13 km depth and non-volcanic tremor locations can clearly be attributed to the deep San Andreas fault southwest to its surface trace.
The reflectivity structure of the lower crust beneath the San Joaquin Valley was imaged for the first time at this particular location. A strong reflective body beneath the sedimentary layer sequences was interpreted as Great Valley ophiolite. The brittle-ductile transition zone and Moho deepen beneath the Great Valley to depths of approximately 32 km at the Sierra Nevada foothills.

This thesis has shown that it is worth to reprocess old seismic data using modern imaging techniques. Existing interpretations can be complemented or modified when additional structural information on the subsurface reflectivity structure are included. Moreover, it offers the possibility to investigate the reflectivity structure of new targets. Beside the SJ-6 reflection data set, the USGS provides the SJ-6 refraction data set that, if preprocessed with Fresnel Volume migration and Reflection Image Spectroscopy, would most likely reveal interesting subsurface features as well. The resolution would be significantly lower because of the low shotpoint number and the large receiver distances.
The reprocessing is significantly cheaper compared to the acquisition of new seismic data and many existing seismic reflection and refraction studies could be complemented this way especially those that have been acquired in the 1980s and early 1990s since new processing techniques have been developed.
It was further shown that Fresnel Volume migration and Reflection Image Spectroscopy are such advanced imaging techniques that produce seismic depth images of high quality. In furture, new or further developed imaging techniques will perhaps be available that are able to reveal even more structural details from old seismic data sets.

References

Atwater, T., 1970, *Implications of Plate Tectonics for the Cenozoic Tectonic Evolution of Western North America*, Geological Society of America Bulletin, v. 81, p.3513–3536.

Bailey, E. H., M. C. J. Blake, D. L. Jones, 1970, *On-land Mesozoic oceanic crust in the California Coast Ranges*, in Geological Survey Research: U.S. Geological Survey Professional Paper 700-C, p. C70-C81.

Bauer, K., T. Ryberg, G.S. Fuis, S. Lüth, 2013, *Seismic Imaging of the Waltham Canyon Fault, California: Comparison of Ray-Theoretical and Fresnel Volume Prestack Depth Migration*, Bull. Seism. Soc. Am., Vol. 103, No. 1, pp. 340-352, doi: 10.1785/0120110338.

Becken, M., O. Ritter, P. A. Bredosian, U. Weckmann, 2011, *Correlation between deep fluids, tremor and creep along the central San Andreas fault*, Nature, Vol.480.

Becken, M. , O. Ritter, 2012, *Magnetotelluric Studies at the San Andreas Fault Zone: Implications for the Role of Fluids*, Surveys in Geophysics, 33, 1, p. 65-105.

Bednar, J. M., 2005, *A brief history of seismic migration*, Geophysics, 70, no. 3, 3MJ - 20MJ.

Bleibinhaus, F., Hole, J.A., Ryberg, T., Fuis, G.S., 2007, *Structure of the California Coast Ranges and San Andreas Fault at SAFOD from seismic waveform inversion and reflection imaging*, J. Geophys. Res.,112,B06315,doi:10.1029/2006JB004611.

Bleistein, N., 1999, *Hagedoorn told us how to do Kirchhoff Migration and inversion*, The Leading Edge 18, 918-927.

Bleistein, N., S. H. Gray, 2001, *From the Hagedoorn imaging technique to Kirchhoff migration and inversion*, Geophysical Prospecting, 49, 629-643.

Bloch, R. B., R. von Huene, P. E. Hart, C. M. Wentworth, 1993, *Style and magnitude of tectonic shortening normal to the San Andreas fault across Pyramid Hills and Kettleman Hills South Dome, California*, Geol. Soc. Am. Bull.,v.105, p. 464–478.

Brown, R. D., Jr., 1990, *Quaternary deformation: In The San Andreas Fault System, California*: Wallace, R.E., ed.,U.S. Geological Survey Professional Paper 1515, p. 83–113.

Bryant, W. A., and Lundberg, M. Matthew, compilers, 2002, *Fault number 1e, San Andreas fault zone, Creeping section, in Quaternary fault and fold database of the United States*: U.S. Geological Survey website, http://earthquakes.usgs.gov/hazards/qfaults, accessed 02/07/2014 04:09 AM.

Buske, S., 1999, *Three-dimensional pre-stack Kirchhoff migration of deep seismic reflection data*, Geophys. J. Int., 137, 243-260.

Buske, S., S. Gutjahr, S. Rentsch, S. Shapiro, 2007, *Active and Passive Seismic Imaging of the San-Andreas-Fault-System*, EAGE 69^{th} annual meeting and technical exhibition, London, Expanded Abstracts.

Buske, S., S. Gutjahr, C. Sick, 2009, *Fresnel Volume Migration of single-component seismic data*, Geophysics, Vol.74, No.6, WCA47–WCA55.

Catchings, R. D., M. Goldman, G. S. Fuis, M. J. Rymer, 2009, *Pre-Stack Depth-Migrated Reflection Images of the Central California Coast ranges: Industry Seismic Reflection Profile SJ-6*, American Geophysical Union, Fall Meeting 2009, abstract #S43D-07.

Chalbaud, D. A., 2010, *Imaging the Chilean continental margin using wide-angle data*, Ph.D. thesis, Freie Universität Berlin

Claerbout, J., 1976, *Fundamentals of geophysical data processing*: Blackwell Scientific Publications.

Červerný, V. & J. E. P. Soarez, 1992, *Fresnel Volume ray tracing*, Geophysics, 57, 902-915.

Červerný, V., 2001, *Seismic ray theory*, Cambridge University Press.

Choi, S. H., J. W. Shervais, S. B. Mukasa, 2008, *Supra-subduction and abyssal mantle peridotites of the Coast Range ophiolite, California*, Contrib Mineral Petrol, 156, 551-576.

Dickinson, W. R., 1983, *Cretaceous Sinistral Strike Slip Along Nacimiento Fault in Coastal California*, The American Association of Petroleum Geologists Bulletin, V.67, No.4 (April 1983), p.624-645.

Eaton, J. P., M. J. Rymer, 1990, *Regional Seismotectonic Model for the Southern, Coast Ranges*, in The Coalinga , California, Earthquake of May 2, 1983, USGS Professional Paper 1487, p. 97–111.

Fliedner, M. M., S. L. Klemperer, N. I. Christensen, 2000, *Three-dimensional seismic model of the Sierra Nevada arc, California, and its implications for crustal and upper mantle composition*, Journal of Geophys. Res., Vol. 105, No. B5, pages 10,899-10,921.

Fuis, G. S., and W. D. Mooney, 1990, *Lithospheric structure and tectonics from seismic-refraction and other data*, in Wallace, R.E., edit., the San Andreas fault system: USGS Prof. Paper 1515, 207–236.

Gazdag, J.,1978, *Wave equation migration with the phase-shift method*, Geophysics, Vol. 43, SPECIAL SECTION – GEOTHERMAL, 1342-1351.

Godfrey, N. J., Y. Dilek, 2000, *Mesozoic assimilation of oceanic crust and island arc into the North American continental margin in California and Nevada: Insights from geophysical data*, in Dilek, Y., Moores, E. M., Elthon, D., and Nicolas, A., eds., Ophiolites and Oceanic Crust: New Insights from Field Studies and the Ocean Drilling Program: Boulder, Colorado, Geological Society of America Special Paper 349, p.365–382.

Godfrey, N. J., S. L. Klemperer, 1998, *Ophiolitic basement to a forearc basin and implications for continental growth: The Coast Range / Great Valley ophiolite, California*, Tectonics, Vol. 17, No. 4, Pages 558–570.

Görtz, A., C. Müller, S. Buske, S. Lüth, 2003, *Fresnel-volume multicomponent migration*, 655th Annual International Meeting, EAGE, Extended Abstracts, P144.

Gutjahr, S., 2009, *Seismic Imaging of the San-Andreas-fault system using multicomponent data*, Thesis, Freie Universität Berlin.

Hill, D. P., J. P. Eaton, L. M. Jones, 1987, *Seismicity, 1980-86*, in Wallace, R.E., edit., The San Andreas Fault System, Open-File Report 87–73.

Irwin, W. P., 1987, *Geology and Plate-Tectonic Developement*, in Wallace, R.E., edit., The San Andreas Fault System, Open-File Report 87–73.

Jennings, C. W., G. J. Saucedo, T. R. Toppozada, 2002, *Simplified fault activity map of California*, California. Dept. of Conservation, web page, <http:www.consrv.ca.gov/cgs/publications/Pages/SearchCGSPubs.aspx>; (downloaded from web site on August 12, 2014)

Keary, P., M. Brooks, (1990), *An Introduction to Geophysical Prospecting*, Blackwell Scientific Publications, Oxford.

Kious, W.J., R. I. Tilling, 1996, *This Dynamic Earth: the story of Plate Tectonics*, U.S. Department of the Interior / U.S. Geological Survey

Lin, G., C. H. Thurber, H. Zhang, E. Hauksson, P. M. Shearer, F. Waldhauser, T. M. Brocher, J. Hardebeck, 2010, *California statewide three-dimensional seismic velocity model from both absolute and differential times*, Bull. Seism. Soc. Am., 100, pp.225–240.

Lüth, S., S. Buske, R. Giese, A. Goertz, 2005, *Fresnel Volume migration of multicomponent data*, Geophysics, 70, no. 6, S121-129.

Mc Bride, J. H., L. D. Brown, 1986, *Reanalysis of the COCORP deep Seismic Reflection Profile Across the San Andreas fault, Parkfield, California*, Bull. Seism. Soc. Am., Vol.76, No.6, pp. 1668–1686.

Meissner, R., W. Rabbel, H. Kern, 2006, *Seismic lamination and anisotropy of the Lower Continental Crust*, Tectonophysics, 416, 81-99.

Mooney, W. D., A. W. Walter, 1987, *Interpretation of coincident seismic reflection and refraction data in laterally inhomogeneous structure: A discussion of the results*, Interpretations of the SJ-6 seismic Reflection/Refraction Profile, South Central California, Open-File Report 87–73.

Mooney, W. D., and T. M. Brocher, 1987, *Coincident seismic reflection/refraction studies of the continental lithosphere: a global view*, Review of Geophysics, 25, 723–742.

Nadeau, R. M. , and D. Dolenc, 2005, *Nonvolcanic Tremors Deep Beneath the San Andreas Faul*, Science, Vol. 307, p. 389.

Nadeau, R. M., and A. Guilhem, 2009, *Nonvolcanic tremor evolution and the San Simeon and Parkfield, California earthquakes*, Science, 325, 191–193, doi:10.1126/science.1174155.

Obara, K., 2002, *Nonvolcanic deep tremor associated with subduction in Southwest Japan*, Science, 296, 1679-1681.

Ozacar, A. A. and G. Zandt, 2009, *Crustal structure and seismic anisotropy near the San Andreas fault at Parkfield, California*, Geophys. J. Int., 178, 1098-1104.

Page, B. M., 1970, *Sur-Nacimiento Fault Zone of California: Continental Margin Tectonics*, Geological Society of America Bulletin, March 1970, v. 81, no. 3, p. 667-690.

Page, B. M., G. A. Thompson, R. G. Coleman, 1998, *OVERVIEW: Late Cenozoic Tectonics of the Central and Southern Coast Ranges of California*, GSA Bull., v. 110, no. 7, p. 846–876.

Podvin P. and I. Lecomte, 1991, *Finite difference computation of traveltimes in very contrasted velocity models: a massively parallel approach and its associated tools*, Geophys. J. Int., 105, 271-284.

Popov, A. A., S. V. Sobolev, M. D. Zoback, 2012, *Modeling evolution of the San Andreas Fault system in northern and central California*, Geochem. Geophys. Geosyst., 13, Q08016, doi:10.1029/2012GC004086.

Rubinstein J. L., D. R. Shelly, W. L. Ellsworth, 2010, *Non-volcanic Tremor: A Window into the Roots of Fault Zones*, in New Frontiers in Integrated Solid Earth Sciences, edited by S. Cloetingh and J. Negendank, pp. 287–314, Springer Science+Business Media B.V., doi:10.1007/978-90-481-2737-5_8.

Ryberg, T., Ch. Haberland, G.S. Fuis, W. L. Ellsworth, D. R. Shelly, 2010, *Locating non-volcanic tremor along the San Andreas Fault using a multiple array source imaging technique*, Geopys. J. Int., 183, 185–1500.

Schneider, W. A., 1978, *Integral formulation for migration in two and three dimensions*, Geophysics, 43, 49-76.

Shelly, D. R., W. L. Ellsworth, T. Ryberg, C. Haberland, G. S. Fuis, J. Murphy, R. M. Nadeau, and R. Bürghmann, 2009, *Precise location of San Andreas Fault tremors near Cholame, California using seismometer clusters: Slip on the deep extension of the fault?*, Geophys. Res. Lett., 36, L01303, doi:10.1029/2008GL036367.

Sherrif, R. E., 1991, *Encyclopedic Dictionary of Applied Geophysics*, 4th ed., Geophysical References Series #113, Soc. Expl. Geoph., Tulsa, OK

Shervais, J. W., D. L. Kimbrought, 1985, *Geochemical evidence for the tectonic setting of the Coast Range ophiolite: a composite island arc-oceanic crust terrane in western California*, Geology (Boulder), 13, 35-38.

Sick, C., 2006, *Structural investigations off Chile: Kirchhoff prestack depth migration versus Fresnel-Volume migration*, Ph.D. thesis, Freie Universität Berlin

Spetzler, J., R. Snieder, 2004, *Tutorial: The Fresnel volume and transmitted waves*, Geophysics, Vol. 69, No.3, (May-June 2004), p.653-663.

Suess, M. P. and J. H. Shaw, 2003, *P-wave seismic velocity structure from sonic logs and industry reflection data in the Los Angeles basin, California*, Journal of Geophysical Research, 108/B3.

Thatcher, W., 1990, *Present-day crustal movements and the mechanics of cyclic deformation*, in Wallace, R.E., edit., the San Andreas fault system: USGS Prof. Paper 1515, 207–236.

Thurber, C., H. Zhang, F. Waldhauser, J. Hardebeck, A. Michael, D. Eberhart-Phillips, 2006, *Three-dimensional compressional wavespeed model, earthquake relocations, and focal mechanisms for the Parkfield, California region*, Bull. Seism. Soc. Am., 96, S38–S49.

Tietze, K., O. Ritter, 2013, *3D magnetotelluric inversion in practice - the electrical conductivity structure of the San Andreas Fault in Central California.*, GJI, 195, 1, 130-147.

Trehu, A., and W. H. Wheeler, 1987, *Possible evidence in the seismic data of profile SJ-6 for subducted sediments beneath the Coast Ranges of California, USA*, Interpretations of the SJ-6 seismic Reflection/Refraction Profile, South Central California, Open-File Report 87–73.

Trehu, A. M., W. H. Wheeler, 1987, *Possible evidence for subducted sedimentary materials beneath central California*, Geology, v. 15, p. 259–261.

Waldhauser, F., and D.P. Schaff, 2008, *Large-scale relocation of two decades of Northern California seismicity using cross-correlation and double-difference methods*, J. Geophys. Res., 113, B08311, doi: 10.1029/2007JB005479.

Walter, A. W., W. D. Mooney, C. M. Wentworth, 1987, *An interpretation of seismic reflection and refraction data recorded between Cholame Valley and the Sierra Nevada, California, USA*, Interpretations of the SJ-6 seismic Reflection/Refraction Profile, South Central California, Open-File Report 87–73.

Wentworth, C. M., M. D. Zoback, J. A. Bartow, 1984, *Tectonic Setting of the 1983 Coalinga Earthquakes from Seismic Reflection Profiles: A Progress Report*, Open-File Report 85-44, MECHANICS OF THE MAY 2, 1983 COALINGA EARTHQUAKE.

Wentworth, C. M., Zoback, M. D., Griscom, A., Jachens, R. C. and Mooney, W. D., 1987, *A transec across the Mesozoic accretionary margin of central California*, Royal Astronomical Society Geophysical Journal, v. 89, no. 1, p. 105-110.

Yilmaz, Ö., 1987, *Seismic Data Processing*, Society of Exploration Geophysicists.

Yoon, M., 2005, *Deep Seismic Imaging in the Presence of Heterogeneous Overburden: Numerical Modelling and Case Studies from the Central Andes and Southern Andes*, PhD thesis, Freie Universität Berlin

Yoon, M., S. Buske, S.A. Shapiro, P. Wigger, 2009, *Reflection Image Spectroscopy across the Andean subduction zone*, Tectonophysics Volume 472, Issues 1–4, 1 July 2009, Pages 51–61.

Zhang, H. and C. H. Thurber, 2003, *Double-difference tomography: the method and its application to the Hayward fault, California*, Bull. Seism. Soc. Am., Vol.93, pp. 1875-1889.

Danksagung

Ohne die Hilfe vieler netter Menschen wäre diese Arbeit nie entstanden.

An erster Stelle möchte ich mich ganz herzlich bei Herrn Prof. Serge Shapiro für die Betreuung dieser Arbeit und seine Unterstützung über den gesamten Entstehungszeitraum hinweg bedanken.

Herr Prof. Stefan Buske hat die Vorraussetzungen dafür geschaffen, dass ich mich mit diesem spannenden Thema auseinandersetzen durfte und diese Arbeit beginnen konnte. Seine Betreuung und seine zahlreichen Anregungen halfen mir viele Probleme, die sich bei der Bearbeitung der Daten ergaben, zu lösen. Herzlichen Dank dafür!

Bei beiden bedanke ich mich auch für die Begutachtung dieser Arbeit.

Ein besonderer Dank gilt meinem Kollegen Herrn Oliver Krüger, der stets ein offenes Ohr für Probleme jeglicher Art hat. Bei fachlichen Problemen stand er mir immer mit Rat und besonders mit Tat zur Seite.

Frau Antonia Oelke danke ich sehr für das Korrekturlesen einiger Passagen der Arbeit und das offene Ohr für die kleinen und größeren Probleme.

Eine wesentliche Vorraussetzung für die Entstehung dieser Arbeit lieferte die finanzielle Unterstützung der Projekte *Active and Passive Seismic Imaging of the San-Andreas-Fault-System* und *Multiscale Seismic Imaging of the San Andreas Fault System* durch die Deutsche Forschungsgemeinschaft. Ein wichtiger Teil der finanziellen Unterstützung kam vom PHASE Research Projekt unter der Leitung von Prof. Serge Shapiro. Ihm und den Sponsoren des Projekts gilt mein besonderer Dank.

Clifford Thurber danke ich sehr für die Bereitstellung des Geschwindigkeitsmodells. Robert

Nadeau und David Shelly stellten mir ihre Tremorlokationen zur Verfügung. Allen dreien danke ich für ihr Interesse an dieser Arbeit.
Gary Fuis und Marc Goldmann vom United States Geological Survey bereiteten die Daten im Vorfeld auf und machten sie uns freundlicherweise zugänglich.

Meinen Kolleginnen und Kollegen Karsten, Jonas, Wasja, Jörn, Carsten, Cornelius, Nicolas, Sibylle, Ramona, Aurelian, Slava, Henri, Anton, Lucie und Florian danke ich sehr für die nette Arbeitsatmosphäre.
Ich bedanke mich auch herzlich bei Frau Malgorzata Grunenberg für ihre Bereitschaft, mir stets bei allen Verwaltungsangelegenheiten zu helfen.

Ohne meine Familie wäre ich nie in der Lage gewesen diesen Weg einzuschlagen. Meinen Eltern Bärbel und Horst Gutjahr bin ich zu besonderem Dank verpflichtet, da sie viel Geduld mit mir hatten und mir die nötigen Freiheiten und das damit verbundene Vertrauen gaben.
Eine große Stütze sind mir mein Mann Skiba und mein Sohn Hagen, die mir stets zeigen, wie wichtig es ist, die Arbeit Arbeit sein zu lasssen, die mir aber auch ein wichtiger Antrieb sind, weiterzumachen und nicht aufzugeben.

Meinen lieben und langjährigen Freundinnen und Freunden Ulli, Jule, Johanna, Steffen, Janine, Frank, Anja, Steven und Ulrike danke ich für die vielen schönen und lustigen Stunden. Besonders aber für die Treue, die diese besonderen Freundschaften schon so lange am Leben halten und hoffentlich noch für lange Zeit halten werden.
Anja und Steven danke ich für das Korrekturlesen einiger Passagen und den vielen Verbesserungsvorschlägen. Ihr habt euch tapfer durchgekämpft!